UNIVERSIDAD NACIONAL AUTÓNOMA DE MÉXICO

PROGRAMA DE MAESTRÍA Y DOCTORADO EN CIENCIAS MATEMÁTICAS Y DE LA ESPECIALIZACIÓN EN ESTADÍSTICA APLICADA

MICRO-TABLA: NUMERICAL MODELLING OF NON-HOMOGENEOUS PLATE VIBRATIONS

TESIS
QUE PARA OPTAR POR EL GRADO DE:

MAESTRO EN CIENCIAS

PRESENTA:

MATEO TONATIUH RODRÍGUEZ CERVANTES

DIRECTOR

DR. PABLO PADILLA LONGORIA
INSTITUTO DE INVESTIGACIONES EN MATEMÁTICAS APLICADAS Y EN SISTEMAS, UNAM

CIUDAD DE MÉXICO, NOVIEMBRE, 2023

Agradecimientos

Me gustaría expresar mi sincera gratitud a las siguientes personas y organizaciones que me han apoyado a lo largo de mi trayectoria académica:

En primer lugar, quiero agradecer a CONAHCYT por su apoyo durante mis estudios de maestría en el Programa de Maestría en Ciencias Matemáticas de la Universidad Nacional Autónoma de México. Además, quiero expresar mi sincero agradecimiento a todos los profesores que han sido fundamentales en mi aprendizaje y crecimiento durante mis estudios de maestría. Su dedicación, experiencia y orientación han dado forma a mi trayectoria académica y han contribuido en gran medida a mi conocimiento y comprensión.

También estoy agradecido al Programa de Posgrado de la Maestría en Ciencias Matemáticas de la Universidad Nacional Autónoma de México por su apoyo, que me permitió realizar una estancia de investigación en la Universidad de Cambridge a través del programa PAPIPE.

Me gustaría extender mi agradecimiento al Dr. Deepak Venkateshvaran por brindarme la oportunidad de colaborar con él durante mi estancia académica en la Universidad de Cambridge. También agradezco el apoyo recibido a través del financiamiento de la Royal Society (Royal Society Reference No. URF\R1\201590).

Además, quiero reconocer al Sr. Francis Knights por brindarme la oportunidad de colaborar en el proyecto de Métodos Formales en Musicología y por invitarme a realizar una estancia académica en Fitzwilliam College, Universidad de Cambridge, durante el otoño de 2022.

Quiero expresar mi más sincero agradecimiento al Dr. Pablo Padilla Longoria por

su apoyo constante y orientación. Ha desempeñado un papel crucial en hacer posible todas las oportunidades mencionadas anteriormente y muchas más para mí.

Finalmente, quiero expresar mi gratitud a mi familia por su constante y amable apoyo a lo largo de mi trayectoria académica.

Estoy realmente agradecido con todos aquellos que han contribuido a mi crecimiento personal y académico. Gracias por su apoyo inquebrantable y su creencia en mis habilidades.

Acknowledgments

I would like to express my sincere gratitude to the following individuals and organizations who have supported me throughout my academic journey:

Firstly, I would like to thank CONAHCYT for their support during my master's studies at the Master in Mathematical Sciences program at the Universidad Nacional Autónoma de México. In addition, I would like to express my sincere thanks to all the teachers who have been instrumental in my learning and growth during my master's studies. Their dedication, expertise, and guidance have shaped my academic journey and contributed greatly to my knowledge and understanding.

I am also grateful to the Postgraduate Program of the Master in Mathematical Sciences at the Universidad Nacional Autónoma de México for their support, which allowed me to pursue a research stay at the University of Cambridge through the PAPIPE program.

I would like to extend my appreciation to Dr. Deepak Venkateshvaran for providing me with the opportunity to collaborate with him during my academic stay at the University of Cambridge. I am also thankful for the support received through the funding from the Royal Society (Royal Society Reference No. URF\R1\201590).

Furthermore, I would like to acknowledge Mr. Francis Knights for granting me the opportunity to collaborate in the Formal Methods in Musicology project and for inviting me to undertake an academic stay at Fitzwilliam College, University of Cambridge during the Autumn of 2022.

I would like to extend my deepest thanks to Dr. Pablo Padilla Longoria for his

unwavering support and guidance. He has played a crucial role in making all the previously mentioned opportunities and more possible for me.

Finally, I want to express my gratitude to my family for their constant and kind support throughout my academic journey.

I am truly grateful to all those who have contributed to my personal and academic growth. Thank you for your unwavering support and belief in my abilities.

Resumen

En este trbajo desarrollamos un modelo numérico de Diferencias Finitas para simular y analizar las vibraciones de placas circulares amortiguadas y no homogéneas con dimensiones microscópicas. Este análisis muestra un aumento en el factor de calidad de las vibraciones de las placas en ciertos regímenes de carga. Estos resultados pueden ser utilizados como pautas de fabricación para nanodispositivos.

Abstract

We develop a Finite Difference numerical model to simulate and analyse the vibrations of non-homogeneous damped circular plates with microscopic dimensions. This analysis shows an improvement of the quality factor of the plates vibrations in certain loading regimes. These results can be used as manufacturing guidelines for nanodevices.

Contents

Prefacio

La investigación presentada en esta tesis es el resultado de la estancia académica del autor en la Universidad de Cambridge desde septiembre hasta diciembre de 2022. Durante este período, el autor colaboró con el Dr. Deepak Venkateshvaran[1] en un proyecto enfocado en la investigación de vibraciones en placas no homogéneas. La investigación se inspiró en las vibraciones observadas en la *tabla*, un tambor indio, donde una membrana circular es sometida a cargas para modificar los modos de vibración y, en consecuencia, alterar el sonido producido. El Dr. Venkateshvaran es un profesional en el campo de la electromecánica polimérica a escala nanométrica, con un profundo conocimiento de los avances más recientes en el campo. Fue a través de esta colaboración y experiencia que surgió la idea de crear un dispositivo Micro-Tabla, lo que llevó al desarrollo del concepto de dicho dispositivo. El Dr. Venkateshvaran planteó dos preguntas principales:

1. ¿Se puede mejorar la *armonicidad*[2] de los modos de vibración en una placa circular elástica hecha de polímero al cargarla con círculos concéntricos de material metálico?

2. ¿Se puede mejorar el *factor de calidad*[3] de las vibraciones de la placa a través del mismo procedimiento de carga?

Estas preguntas se abordaron mediante la aplicación de un Método de Diferencias Finitas (FDTD, por sus siglas en inglés) para resolver el problema de valor inicial y de frontera de la deflexión de una placa circular no homogénea con borde fijo, en el régimen elástico. Se desarrollaron dos esquemas de FDTD para este propósito: uno en coordenadas cartesianas y otro en coordenadas polares. El esquema de coordenadas polares mostró una mayor estabilidad numérica que el esquema cartesiano, pero ambos proporcionaron respuestas confiables a las preguntas planteadas, en ciertos regímenes de carga y con consideraciones específicas. Además, el esquema cartesiano tiene el potencial de modelar las vibraciones con borde fijo de placas y membranas con formas arbitrarias.

El autor de este texto desarrolló una tesis de licenciatura sobre simulaciones

[1] El Dr. Deepak Venkateshvaran es Miembro y Director de Estudios en Física en Selwyn College, Universidad de Cambridge. Posee una Beca de Investigación Universitaria de la Royal Society en el Laboratorio Cavendish de Cambridge, donde estudia las propiedades mecánicas de los materiales poliméricos a escala nanométrica.

[2] Definida en la sección 5.1.

[3] Definido en la sección 5.2.

numéricas de las vibraciones de barras no homogéneas [Rodríguez-Cervantes, 2019]. Las placas son el equivalente bidimensional de una barra (similar a cómo una membrana es el equivalente bidimensional de una cuerda), de esta manera, el trabajo previo sobre barra proporcionó el trasfondo adecuado para el presente trabajo.

En la siguiente sección, realizaremos una breve revisión histórica de la investigación en la acústica de la tabla, incluida una introducción a la organología de este instrumento. Posteriormente, en la sección siguiente, introduciremos brevemente los Sistemas Microelectromecánicos (MEMS), incluida una explicación de las posibles aplicaciones de este trabajo en este campo específico. Gran parte de este material introductorio fue proporcionado por el Dr. Venkateshvaran a través de un breve artículo que se publicará en el Calendario del Selwyn College [Venkateshvaran and Smith, 2023].

Introducción

Raman y el tambor indio *Tabla*

En 1920, el físico indio Sir C. V. Raman, quien más tarde recibiría el Premio Nobel, escribió una carta al editor de la revista Nature [Raman and Kumar, 1920]. En esta carta, presentó la primera elucidación científica de las tonalidades melódicas producidas por un antiguo instrumento de percusión indio llamado tabla. Raman resaltó que este instrumento, que depende de una membrana para su generar sonido, produce frecuencias que se alinean como armónicos. Este atributo único permite que el tambor tabla se ajuste finamente a una nota armónica solitaria, diferenciándolo de la mayoría de otros tambores y estableciendo una semejanza con las cuerdas de instrumentos musicales como violines y guitarras.

Figure 1: Material fotográfico proporcionado por el Dr. Deepak Venkateshvaran. Una membrana cargada de un tambor tabla. Un material negro está depositado de manera concéntrica en una piel de tambor de cuero. Esta construcción genera un sonido armónico.

Los instrumentos que pueden ser descritos por modelos que involucran la ecuación de onda unidimensional, ya sea que dependan de cuerdas o columnas de aire, exhiben un comportamiento armónico de sus modos de vibración de manera natual. Sin embargo, la propiedad de la armonicidad no es inherente a membranas bidimensionales, como las que se encuentran en los tambores. Los tambores que consisten en una sola membrana, como el tambor de caja o el conga, típicamente carecen de una resonancia armónica debido a las relaciones no enteras entre sus frecuencias modales[4]. En su correspondencia, Raman destacó que la armonicidad del tabla derivaba de su estructura

[4]Las frecuencias de las soluciones dadas en modos normales de la ecuación de onda bidimensional

de membrana distintiva, caracterizada por una piel de cuero que incorpora un material disímil colocado centralmente (representado en la Figura 1.1). Él enfatizó que esta capa de carga adaptable y firmemente fijada consistía principalmente en hierro metálico finamente dividido, una sustancia con una densidad mayor que la membrana de cuero acompañante.

El perfeccionamiento de un tabla armónicamente afinada evolucionó a partir de repetidos ensayos y errores. Incluso en tiempos contemporáneos, estos instrumentos son creados por artesanos que poseen un conocimiento mínimo o nulo de las matemáticas intrincadas que respaldan sus creaciones. Guiados únicamente por la intuición y la evaluación auditiva, los fabricantes de tablas ajustan incrementalmente la capa de carga, alternativamente aplicándola y retirándola, mientras golpean periódicamente la membrana para evaluar las características sonoras y converger en la armonicidad. Esta artesanía es una tradición transmitida a través de generaciones, como un secreto celosamente guardado dentro de las genealogías de las familias indias productoras de tablas.

La concisa comunicación de Raman a la revista Nature en 1920 fue seguida por una publicación más extensa en 1935, en la que ofreció una exploración integral de los diversos modos vibratorios inherentes a la membrana del tambor tabla, elucidando su papel en la producción de la armonicidad [Raman, 1934]. Durante el período intermedio entre estos dos artículos, Raman se sumergió en el estudio de las características vibratorias moleculares y su interacción con la luz, un esfuerzo que culminó en la obtención del Premio Nobel de Física en 1930. Se ha conjeturado que los fundamentos conceptuales para sus ideas sobre la interacción entre la luz y las moléculas, particularmente cómo la luz es dispersada por las moléculas a través de sus modos vibratorios, podrían haber tenido sus raíces en su fascinación por los modos vibratorios de los instrumentos musicales indios [Ramakrishnan, 1988]. Como lo expresó un historiador, "Raman's early fascination with acoustics became the basis of his later insights into the nature of the light quantum" [Banerjee, 2014].

El análisis matemático de los patrones vibratorios exhibidos por el tambor tabla indio ha cautivado a numerosos académicos en años posteriores[5]. Basándose en las primeras ideas de Raman, la comprensión actual revela que los modos vibratorios del tabla se ajustan a armónicos solo a partir del segundo modo en adelante. El modo fundamental, que implica la vibración colectiva de toda la membrana del tambor, no se alinea con la relación correcta para la armonicidad y debe ser suprimido. Curiosamente, los propios músicos de tabla a menudo desconocen que es este modo primario de vibración el que se suprime mediante la colocación deliberada del dedo anular en la membrana durante la interpretación (consultar la figura 1.2), lo que resulta en la producción de un dulce timbre armónico. Esto es un ejemplo de cómo tanto los fabricantes como los músicos de tabla se aferran a lo que se debe hacer para generar un tono armónico en el instrumento, sin necesitar las matemáticas que describen la vibración del instrumento.

---

en un dominio circular se expresan como raíces de la función de Bessel, las cuales no están dispuestas armónicamente [Leissa and Qatu, 2011]

[5]Por ejemplo, consultar: [Gaudet et al., 2006, Rossing, 1992, Tiwari and Gupta, 2017, Sathej and Adhikari, 2009, Dubey and Krishna, 2021].

Figure 2: Material fotográfico proporcionado por el Dr. Deepak Venkateshvaran. La posición del dedo anular en el tambor tabla asegura la supresión del modo fundamental, necesario para obtener el sonido más armónico.

La armonicidad, sin embargo, constituye solo una faceta de los atributos distintivos del tabla. Concluyendo su sucinta misiva al editor de Nature, Raman agregó la siguiente observación: "La carga central también mejora el efecto musical al aumentar la energía de vibración y, por lo tanto, prolongar la duración de los tonos". Básicamente, quiso decir que una vez que se golpea la membrana del tambor tabla, el sonido generado tarda mucho tiempo en decaer. Usando un término técnico, esta tasa de decaimiento más lenta implica un factor de calidad Q más alto. Este comportamiento del tabla, en comparación con un tambor ordinario, es un poco como adjuntar una pesada bola de acero en el centro de un trampolín: una vez empujado, continuaría oscilando durante más tiempo que un trampolín ordinario, debido a la masa adicional. Como se menciona en [Venkateshvaran and Smith, 2023]: “This increased Q-factor of a tabla’s vibrating membrane remains relatively unknown but could have implications for Microelectromechanical systems (MEMS) devices in engineering physics”.

Sistemas Microelectromecánicos (MEMS)

Los Sistemas Microelectromecánicos (MEMS) son la tecnología de dispositivos microscópicos que incorporan tanto componentes electrónicos como móviles. El término "MEMS" fue introducido en 1986 por S.C. Jacobsen (PI) y J.E. Wood (Co-PI) a través de una propuesta a DARPA (15 de julio de 1986), titulada "Micro Electro-Mechanical Systems (MEMS)", otorgada a la Universidad de Utah.

Como se afirma en [Venkateshvaran and Smith, 2023]: “Microelectromechanical systems have played a salient role in research, development, and commercial deployment for decades. Indeed, the accelerometer embedded in every smartphone to aid with GPS tracking is one such example of a MEMS device in ubiquitous use. We considered whether it would be possible to make a miniature equivalent to the tabla, with similar harmonic properties, which might potentially improve its performance in sensor applications. However, the equivalent MEMS device wouldn’t be under tension, unlike a drumhead(...)”.

Dado este contexto, la ausencia de tensión en el plano del dispositivo dirige el enfoque de estudio de las vibraciones de estos dispositivos hacia una interacción elástica interna exclusivamente. En consecuencia, la representación más adecuada para estos dispositivos es una placa elástica, en lugar de una membrana.

La relevancia de este estudio se puede ejemplificar con las palabras en [Heinrich and Dufour, 2015]:

"Resonators based on MEMS (micro-electromechanical systems) and NEMS (nano-electromechanical systems) span a broad spectrum of important current applications, including detection of chemical and biological substances, measurement of rheological properties of fluids, and energy harvesting, to name only a few. While the devices that perform these diverse functions span an equally broad range in geometric layout, material properties, circuitry, fabrication techniques, packaging, and so on, they all have one aspect in common: the phenomenon of 'resonance' forms the basis of their operating principle." Algunos ejemplos de trabajos recientes sobre resonadores utilizados en NEMS/MEMS y estudios de sus propiedades elásticas son [Šiškins et al., 2022], [Zheng et al., 2017] y [Schlicke et al., 2016].

Otra innovación notable propuesta por el Dr. Venkateshvaran involucra el uso de polímeros en la fabricación de resonadores en MEMS. Una ventaja distintiva presentada por estos materiales es su capacidad dual para poseer propiedades elásticas adecuadas y exhibir conductividad o semiconductividad eléctrica. Sin embargo, una desventaja notable es su tendencia a generar un bajo factor de calidad Q, que, como se explica en [Venkateshvaran and Smith, 2023]: "The MEMS devices in commercial deployment today are made of inorganic materials, mostly silicon-based. Using polymers for such devices is not popular yet, arguably because a vibrating polymer element has Q-factors that are in the single digits, too low for applications."

En este contexto, el modelo matemático y computacional delineado en este estudio tiene como objetivo examinar las vibraciones de dispositivos circulares microscópicos compuestos de polímeros. Inspirados en el diseño del tabla, estos dispositivos están sujetos a carga metálica concéntrica, con el objetivo principal de investigar el aumento potencial del factor de calidad inherente a tales dispositivos.

Preface

The research presented in this thesis is the outcome of the author's academic stay at the University of Cambridge from September to December 2022. During this period, the author collaborated with Dr. Deepak Venkateshvaran[6] on a project focused on the investigation of vibrations in non-homogeneous plates. The research inquiry was inspired by the vibrations observed in the *tabla*, an Indian drum, where a circular membrane is subjected to loading to modify the vibration modes and, consequently, alter the produced sound. Dr. Venkateshvaran's expertise is in the field of nanoscale polymer electromechanics. It was through this collaboration that the idea of creating a Micro-Tabla device emerged. Two main questions were posed:

1. Can the *harmonicity*[7] of vibration modes in an elastic circular plate made of polymer be improved by loading it with concentric circles of a metallic material?

2. Can the *quality factor*[8] of plate vibrations be improved through the same loading procedure?

These questions were addressed by applying a Finite Difference Method (FDTD) to solve the initial-boundary value problem of the deflection of a non-homogeneous circular plate with clamped edge, in the elastic regime. Two FDTD schemes were developed for this purpose: one in Cartesian coordinates and another in polar coordinates. The polar coordinate scheme exhibited greater numerical stability than the Cartesian scheme, but both provided reliable answers to the posed questions, in certain loading regimes and with specific considerations. Additionally, the Cartesian scheme has the potential to model the vibrations in clamped plates and membranes with arbitrary shapes.

The author completed a Bachelor's thesis on numerical simulations of the vibrations of non-homogeneous beams [Rodríguez-Cervantes, 2019]. Plates are the two-dimensional equivalent of a beam (similar to a membrane being the two dimensional equivalent of a string), in this way, the previous work on beams provided proper background to the present work.

In the next section, we will make a brief historical review of the research in the acoustics of the tabla, including an introduction to the organology of this instrument. In the subsequent section, we will be briefly introduce the Microelectrome-

[6]Dr. Deepak Venkateshvaran is a Fellow and Director of Studies in Physics at Selwyn College, University of Cambridge. He holds a Royal Society University Research Fellowship at the Cavendish Laboratory in Cambridge where he studies the mechanical properties of polymer materials on the nanoscale.

[7]Defined in section 5.1.

[8]Defined in section 5.2.

chanical Systems (MEMS) including an explanation of the possible applications of this work in this specific field. Most of this introductory material was provided by Dr. Venkateshvaran, via a short acticle to be published in the Selwyn College Calendar [Venkateshvaran and Smith, 2023].

Chapter 1

Introduction

1.1 Raman and the Indian drum *Tabla*

In 1920, the Indian physicist Sir C. V. Raman, who would later win the Nobel Prize, sent a letter to the editor of the Nature Magazine [Raman and Kumar, 1920]. Within this letter, he presented the inaugural scientific elucidation of the melodic tones produced by an ancient Indian percussion instrument called the tabla. Raman highlighted that this instrument, which relies on a membrane for its sound production, generates frequencies that align as harmonics. This unique attribute allows the tabla drum to be finely tuned to a solitary harmonic note, setting it apart from most other drums and drawing a likeness to the strings of musical instruments like violins and guitars.

Figure 1.1: Photographic material provided by Dr. Deepak Venkateshvaran. A loaded membrane of a tabla drum. A black material is deposited concentrically on a leather drumhead. This construction generates a harmonic sound.

Instruments that can be approximated by the one-dimensional wave equation, whether they rely on strings or columns of air, exhibit a harmonic arrange in their modes of vibration. This means that the frequencies of their modes of vibration are numerically close to integer multiples of the lowest frequency of vibration or *fundamental frequency*. However, the property of harmonicity isn't inherent in two-dimensional circular membranes, such as those found in drums. Drums consisting of

a single membrane, like the snare drum or conga, typically lack a harmonic resonance due to the non-whole number ratios between their mode frequencies. The frequencies of the solutions to the two-dimensional wave equation over a circular domain are expressed as roots of the Bessel function, which are not harmonically arranged ([Leissa and Qatu, 2011]). In his correspondence, Raman underscored that the tabla's harmonicity stemmed from its distinctive membrane structure, characterised by a leather skin incorporating a centrally placed, dissimilar material (depicted in figure 1.1). He emphasised that this adaptable and firmly affixed load-bearing layer primarily consisted of finely divided metallic iron—a substance possessing greater density than the accompanying leather membrane.

The refinement of a precisely tuned harmonically tabla evolved from repeated trial and error. Even in contemporary times, these instruments are crafted by artisans possessing minimal to no grasp of the intricate mathematics underpinning their creations. Guided solely by intuition and auditory assessment, tabla makers incrementally adjust the loading layer, alternately applying and removing it, while periodically tapping the membrane to gauge the sonic characteristics and converge on harmonicity. This craftsmanship is a tradition handed down through generations, safeguarded as a closely guarded secret within the lineages of Indian tabla-producing families. Furthermore, the loaded membrane system is also used in a wide variety of Indian drums, including the "Mridangam", the "Khol" and the "Pakhawaj".

Raman's concise communication to Nature Magazine in 1920 was followed by a more extensive publication in 1935, wherein he offered a comprehensive exploration of the diverse vibrational modes inherent in the tabla drumhead, elucidating their role in producing harmonicity [Raman, 1934]. During the interim period between these two papers, Raman immersed himself in the study of molecular vibrational characteristics and their interaction with light, an endeavor that culminated in his being awarded the Nobel Prize in Physics in 1930. It has been conjectured that the conceptual foundations for his insights into the interaction between light and molecules, particularly how light is scattered by molecules through their vibrational modes, could have been rooted in his fascination with the vibrational modes of Indian musical instruments [Ramakrishnan, 1988]. As one historian phrased it,"Raman's early fascination with acoustics became the basis of his later insights into the nature of the light quantum" [Banerjee, 2014].

The mathematical analysis of the vibrational patterns exhibited by the Indian tabla has captivated numerous scholars in subsequent years[1]. Building upon Raman's early insights, current understanding reveals that the tabla's vibrational modes conform to harmonics only starting from the second mode onward. The foundational mode, which involves the collective vibration of the entire drumhead, fails to align with the right ratio for harmonicity and needs to be suppressed. Curiously, tabla players themselves are often unaware that it's this primary mode of vibration that is suppressed by the deliberate placement of the ring finger on the drumhead during performance (refer to figure 1.2), resulting in the production of a sweet harmonic

[1]For instance, refer to: [Gaudet et al., 2006, Rossing, 1992, Tiwari and Gupta, 2017, Sathej and Adhikari, 2009, Dubey and Krishna, 2021].

Figure 1.2: Photographic material provided by Dr. Deepak Venkateshvaran. The position of the ring finger on the tabla drum ensures suppression of the fundamental mode, necessary for the most harmonic sound.

timbre. Such is an example of how both tabla makers and tabla players latch on to what needs to be done to generate a harmonic tone on the instrument, without needing any of the mathematics that describe the instrument's vibration.

Harmonicity, however, constitutes merely one facet of the tabla's distinctive attributes. Concluding his succinct missive to Nature's editor, Raman appended the following observation: "The central load also improves the musical effect by increasing the energy of vibration, and thus prolonging the duration of the tones." Essentially, he meant that, once the tabla drumhead is struck, the sound generated takes a long time to decay. To use a technical term, this slower decay rate implies a higher quality factor or Q-factor. This behaviour of the tabla, compared to an ordinary drum, is a little like attaching a heavy steel ball to the centre of a trampoline: once pushed, it would continue to oscillate for longer than an ordinary trampoline would, due to the extra mass. As mentioned in [Venkateshvaran and Smith, 2023]: "This increased Q-factor of a tabla's vibrating membrane remains relatively unknown but could have implications for Microelectromechanical systems (MEMS) devices in engineering physics".

1.2 Microelectromechanical systems (MEMS)

MEMS (Microelectromechanical systems) is the technology of microscopic devices incorporating both electronic and moving parts. The term "MEMS" was introduced in 1986 by S.C. Jacobsen (PI) and J.E. Wood (Co-PI) by way of a proposal to DARPA (15 July 1986), titled "Micro Electro-Mechanical Systems (MEMS)", granted to the University of Utah.

As stated in [Venkateshvaran and Smith, 2023]: "Microelectromechanical systems have played a salient role in research, development, and commercial deployment for decades. Indeed, the accelerometer embedded in every smartphone to aid with GPS tracking is one such example of a MEMS device in ubiquitous use. We considered whether it would be possible to make a miniature equivalent to the tabla, with similar harmonic properties, which might potentially improve its performance in sensor ap-

plications. However, the equivalent MEMS device wouldn't be under tension, unlike a drumhead(...)".

Given this context, the absence of in-plane tension directs the focus of studying the vibrations of these devices toward an exclusive inner elastic interaction. Consequently, the most suitable representation for these devices is an elastic plate, rather than a membrane.

The relevance of this study can be exemplified by the words in
[Heinrich and Dufour, 2015]:

"Resonators based on MEMS (micro-electromechanical systems) and NEMS (nano-electromechanical systems) span a broad spectrum of important current applications, including detection of chemical and biological substances, measurement of rheological properties of fluids, and energy harvesting, to name only a few. While the devices that perform these diverse functions span an equally broad range in geometric layout, material properties, circuitry, fabrication techniques, packaging, and so on, they all have one aspect in common: the phenomenon of 'resonance' forms the basis of their operating principle." Some examples of recent works on NEMS/MEMS resonators and studies of their elastic properties are [Šiškins et al., 2022], [Zheng et al., 2017] and [Schlicke et al., 2016].

Another noteworthy innovation proposed by Dr. Venkateshvaran involves the use of organic polymers in the manufacturing of resonant MEMS. One distinct advantage presented by these materials is their dual capability to possess suitable elastic properties and exhibit electrical conductivity or semi-conductivity. However, a notable drawback is their tendency to yield a low Q-factor, which, as explained in [Venkateshvaran and Smith, 2023]: "The MEMS devices in commercial deployment today are made of inorganic materials, mostly silicon-based. Using polymers for such devices is not popular yet, arguably because a vibrating polymer element has Q-factors that are in the single digits, too low for applications."

In this context, the mathematical and computational model outlined in this study aims to examine the vibrations of microscopic circular plate devices composed of polymers. Inspired by the tabla design, these devices are subjected to concentric metallic loading, with the primary objective of investigating the potential enhancement of the quality factor inherent to such devices.

Chapter 2

Linear elasticity of isotropic materials in continuum mechanics

This chapter provides a concise introduction to the fundamental concepts of elasticity theory in continuum mechanics. The objective is to establish a foundation for understanding subsequent discussions on plate vibrations. The focus is on defining continuum mechanics and its relevance to the study of deformable materials. The concepts of strain and stress tensors are explored, emphasising their essential properties. Furthermore, the elastic constitutive relations for an elastic solid are derived based on the generalised Hooke's Law. It is worth noting that the concepts and derivations presented in this chapter draw heavily from the works [Pujol, 2003] and [Slawinski, 2010].

2.1 The concept of continuum

In continuum mechanics, the atomic structure of matter and the explicit interactions between particles are disregarded. Instead, the concept of a continuum is employed, justified by the assumption that a material is composed of closely spaced particles, enough for its descriptive functions to be treated as continuous. In essence, the infinitesimal elements of the material are assumed to possess the same physical properties as those observed in macroscopic studies. While this idealization does not align with the microscopic structure of real materials, it serves as a valuable framework for mathematical analysis, enabling us to model physical reality using abstract concepts.

The concept of a continuum provides a framework where materials can be treated so that their descriptive functions exhibit continuity and differentiability. This enables us to define stress at a specific point, allowing the application of calculus to the analysis of forces within the continuum. Augustin-Louis Cauchy pioneered this definition and the subsequent utilisation of calculus in the first half of the nineteenth century. Rather than focusing on atomic forces between individual particles, Cauchy introduced the concepts of stress and strain in a continuum, developing the equations associated with the theory of elasticity.

2.2 Conditions of linearized theory

In the continuum approximation to solid dynamics, the Eulerian (or spatial) displacement vector

$$\mathbf{u}(\boldsymbol{x}, t) = [u(\boldsymbol{x}, t), v(\boldsymbol{x}, t), w(\boldsymbol{x}, t)] \tag{2.1}$$

is used to describe changes in the configuration of solids over time, t, and space, $\boldsymbol{x} = (x_1, x_2, x_3)$, from the perspective of an external observer. Another displacement vector can be obtained by adopting the material (or Lagrangian) point of view. In this approach, we focus our attention on a mass of the continuum system as it moves, meaning that we always track the same particles. In short, this consists in adopting another spatial coordinate system $\boldsymbol{X} = (X_1, X_2, X_3)$, and another displacement field $\mathbf{U}(\boldsymbol{X}, t)$. However, it can be shown that for the case of linear dynamics, the Eulerian and Lagrangian descriptions are indistinguishable for infinitesimal displacements, this is

$$\begin{aligned} \boldsymbol{x} &\approx \boldsymbol{X} \\ \mathbf{u}(\boldsymbol{x}, t) &\approx \mathbf{u}(\boldsymbol{X}, t) \approx \mathbf{U}(\boldsymbol{x}, t). \end{aligned} \tag{2.2}$$

Another important consequence of the linear aproach is that the distinctions between time derivatives and material-time derivatives are not taken into account, this is

$$\begin{aligned} \frac{d\mathbf{u}}{dt} &\approx \frac{\partial \mathbf{U}}{\partial t} \\ \frac{d^2\mathbf{u}}{d^2t} &\approx \frac{\partial^2 \mathbf{U}}{\partial t^2}. \end{aligned} \tag{2.3}$$

In this way, we can always work in only one coordinate system to obtain the fundamental continuum dynamics equations, in the linear regime for infinitesimal displacements. For further details see, for example, [Slawinski, 2010], section 1.3.3. In this study we will make use of the linearized theory and work on the Eulerian description.

2.3 Strain tensor

Continuum deformation refers to the alteration of point positions within it each other. When such alteration happens, the continuum experiences strain. This strain induces stress, wherein the resulting stress opposes the deformation, endeavouring to revert the continuum to its original, un-strained state. The continuum's resistance to deformation and its inherent inclination to return to its initial state lead to the propagation of waves.

The strain tensor is a second-order tensor field used to describe the change in shape during the deformation of a solid. In the linear elastic regime, the components of the strain are given by

$$\varepsilon_{ij} = \frac{1}{2}\left(\frac{\partial u_i}{\partial x_j} + \frac{\partial u_j}{\partial x_i}\right), \tag{2.4}$$

which in matrix notation can be represented as

$$\boldsymbol{\varepsilon} = \begin{bmatrix} \varepsilon_{11} & \varepsilon_{12} & \varepsilon_{13} \\ \varepsilon_{21} & \varepsilon_{22} & \varepsilon_{23} \\ \varepsilon_{31} & \varepsilon_{32} & \varepsilon_{33} \end{bmatrix}. \tag{2.5}$$

The *engineering* strain tensor is defined as

$$\gamma_{ij} = 2\varepsilon_{ij}. \tag{2.6}$$

The strain tensor describes two types of deformation, relative linear displacement and relative angular displacement. Further details can be consulted in [Slawinski, 2010], section 1.4.3.

The strain tensor is symmetric, i.e., $\varepsilon_{ij} = \varepsilon_{ji}$, and ε_{ij} with $i = j$ are known as the *normal strains*, while ε_{ij} with $i \neq j$ are known as the *shearing strains*. The eigenvectors of ε_{ij} are referred to as the *principal directions of strain*, and the eigenvalues correspond to the *principal strains*.

The system of equations for the displacement field u given by (2.4) leads to a system of three unknown (the three components of u) and six differential equations, which is an over-determined system. Therefore, for u to be single value and continuous a compatibility equation is needed, and is given by

$$\varepsilon_{ij,km} + \varepsilon_{km,ij} - \varepsilon_{ik,jm} - \varepsilon_{jm,ik} = 0, \tag{2.7}$$

where the sub-index after a coma represents the partial derivative with respect to the coordinates after the coma.

2.4 Stress tensor

The concept of stress is introduced to examine the internal forces exerted between adjacent material elements within the continuum. Stress is a fundamental quantity used to describe the internal distribution of forces within a material. It quantifies the intensity of internal forces per unit area acting on a small surface within the material. By analysing the stress distribution, insights into the material's response to external loads and deformations can be inferred. The study of stress forms the basis for understanding various mechanical phenomena and plays a crucial role analysing and designing structures and materials.

In continuum mechanics, two types of forces are recognised, body forces and surface (or contact) forces. By considering a force $\Delta\mathbf{F}$ acting on an infinitesimally small area ΔS, that has a normal vector $\mathbf{n}$, the surface force called stress vector (or traction), is defined as

$$\mathbf{T}(\mathbf{n}) = \lim_{\Delta S \to 0} \frac{\Delta \mathbf{F}}{\Delta S} = \frac{d\mathbf{F}}{dS}. \tag{2.8}$$

The stress vector satisfies

$$\mathbf{T}(\mathbf{n}) = -\mathbf{T}(-\mathbf{n}), \tag{2.9}$$

by the Cauchy's fundamental lemma, which is similar to Newton's Third Law. By Cauchy's Stress Theorem, there exists a second-order tensor field, $\boldsymbol{\sigma}(\boldsymbol{x}, t)$, called the Cauchy's stress tensor, independent from the unit normal vector $\mathbf{n}$, such that the traction $\mathbf{T}$ is a linear function of $\mathbf{n}$, this is,

$$\mathbf{T}(\mathbf{n}) = \mathbf{n} \cdot \boldsymbol{\sigma}, \quad \text{or} \quad T_i = \sigma_{ij} n_j, \tag{2.10}$$

where

$$\sigma_{ij} = T_j^{(\mathbf{e}_i)}, \tag{2.11}$$

this is, σ_{ij} represents the j-th component of the surface force acting on the surface whose normal is parallel to the x_i-axis (see figure 2.1). The diagonal elements of σ_{ij} are known as *normal stresses*, while the off-diagonal elements are known as *shearing stresses*.

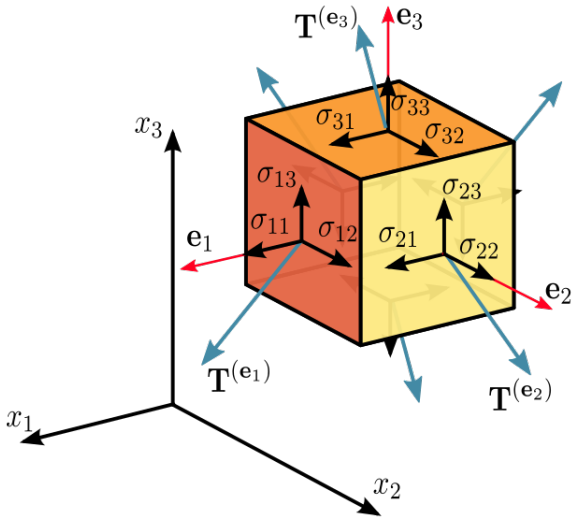

Figure 2.1: Components of the traction vector and stress tensor in Cartesian coordinates[1].

The stress tensor can be represented in matrix notation as

$$\boldsymbol{\sigma} = \begin{bmatrix} \sigma_{11} & \sigma_{12} & \sigma_{13} \\ \sigma_{21} & \sigma_{22} & \sigma_{23} \\ \sigma_{31} & \sigma_{32} & \sigma_{33} \end{bmatrix}. \tag{2.12}$$

[1]Image credits: By Sanpaz - Own work, CC BY-SA 3.0, `https://commons.wikimedia.org/w/index.php?curid=5668647`

2.5 Conservation principles

In this section, some conservation principles that are followed by any continuum system are briefly explained. Some of these principles directly influence on the shape and behaviour of the stress tensor.

Conservation of mass

The principle of conservation of mass stands that the rate of change of the amount of material inside a closed surface equals the net rate with which this material flows through this surface. This principle can be expressed as the equation of continuity, given by

$$\frac{\partial \rho}{\partial t} + \nabla \cdot \left(\rho \frac{\partial \mathbf{u}}{\partial t} \right) = 0, \tag{2.13}$$

where ρ is the volumetric density of the material. This equation relates mass density and displacement.

Balance of linear momentum

By considering the balance of traction forces and body forces by volume unit (denoted by $\mathbf{f}=(f_1, f_2, f_3)$), and a moving volume that consistently contains the same portion of the continuum, and invoking Newton's second law of motion, the balance of linear momentum can be written as

$$\iiint_{V(t)} \rho \frac{\partial^2 \mathbf{u}}{\partial t^2} dV = \iint_{S(t)} \mathbf{T} dS + \iiint_{V(t)} \mathbf{f} dV \tag{2.14}$$

In essence, this principle describes how the application of forces, both on the surface and within the body, influences the motion and behaviour of the material.

It is possible to arrive at **Cauchy's equations of motion**[2], given by

$$\frac{\partial \sigma_{ji}}{\partial x_j} + f_i = \rho \frac{\partial^2 u_i}{\partial t^2}, \qquad i \in \{1, 2, 3\}, \tag{2.15}$$

by considering the balance of linear momentum, substituting $\mathbf{T}$ with (2.10) and applying the divergence theorem.

Cauchy's equations of motion establish a connection between two vector quantities: The surface force, represented by the divergence of the stress tensor σ_{ij}, and the body force, acting on a material element. These equations express that the acceleration of a continuum element is a consequence of both surface and body forces.

If the acceleration term vanishes in equations of motion (2.15), we obtain the

[2]Where we are using the repeated index summation convention (also known as Einstein notation): $\frac{\partial \sigma_{ji}}{\partial x_j} = \sum_{j=1}^{3} \frac{\partial \sigma_{ji}}{\partial x_j}$.

equations of static equilibrium,

$$\frac{\partial \sigma_{ji}}{\partial x_j} + f_i = 0, \qquad i \in \{1, 2, 3\}. \tag{2.16}$$

These equations describe the equilibrium state of an element of the continuum arising from the application of forces whose resultant is zero.

Balance of angular momentum

The balance of angular momentum, emerges from the fact that the time rate of change of angular momentum for a given system is equal to the vector sum of the torques due to the external forces acting on that system. Considering only the central forces acting within the continuum, the balance of angular momentum can be state as

$$\frac{d}{dt}\iiint_{V(t)} \Big(\boldsymbol{x} \times \rho \frac{\partial \mathbf{u}}{\partial t}\Big) dV = \iint_{S(t)} \Big(\boldsymbol{x} \times \mathbf{T}\Big) dS + \iiint_{V(t)} \Big(\boldsymbol{x} \times \mathbf{f}\Big) dV, \tag{2.17}$$

where $V(t)$ is a volume that moves while always containing the same portion of the continuum and $S(t)$ is the surface enclosing this volume. Balance of angular momentum can be expressed in terms of the stress tensor by substituting $\mathbf{T}$ with (2.10) and applying the divergence theorem to obtain

$$\rho\Big(\boldsymbol{x} \times \frac{\partial^2 \mathbf{u}}{\partial t^2}\Big) = \nabla \cdot \Big(\boldsymbol{x} \times \boldsymbol{\sigma}^T\Big) + \boldsymbol{x} \times \mathbf{f}. \tag{2.18}$$

By applying the balance of linear and angular momentum, it can be proved that the stress tensor satisfies

$$\epsilon_{ijk}\sigma_{kj} = 0 \tag{2.19}$$

where ϵ_{ijk} is the Levy-Civita symbol and the convention of sum for repeated indices is being applied. As the Levy-Civita symbol is not symmetric, equation (2.19) implies that the stress tensor is symmetric, i.e.,

$$\boldsymbol{\sigma} = \boldsymbol{\sigma}^T \qquad \text{or} \qquad \sigma_{ij} = \sigma_{ji}. \tag{2.20}$$

Balance of Energy

We can write the Kinetic energy of a continuum body occupying a volume V in terms of the derivative of the displacement vector (which represents a velocity) as

$$K = \frac{1}{2}\int_V \rho \dot{\mathbf{u}} \cdot \dot{\mathbf{u}} dV \tag{2.21}$$

The total internal energy can be found as

$$U = \int_V \rho E dV, \tag{2.22}$$

where E represents the specific internal energy. Also, the rate work made by a deformation in terms of the stress tensor can be found as

$$\frac{dw}{dt} = \int_S \boldsymbol{\sigma} \cdot \dot{\mathbf{u}} dS + \int_V \rho \mathbf{f} \cdot \dot{\mathbf{u}} dV. \tag{2.23}$$

Hence, the **Balance Law of Energy** is given by

$$\frac{dK}{dt} + \frac{dU}{dt} = \frac{dw}{dt} + \frac{dQ}{dt}, \tag{2.24}$$

where Q represents the total heat input. For more details consult [Pujol, 2003].

2.6 Constitutive relations of Isotropic materials

2.6.1 Generalised Hooke's Law

An elastic deformation is characterised by the stress being solely dependent on the current value of the strain, without any dependence on the rate of strain. This implies that the relationship between stress and strain follows an extension of Hooke's Law, which states a proportional relationship between applied forces and resulting deformations. Cauchy generalised Hooke's Law to elastic solids by proposing that stress and strain are linearly related. In tensor form the law takes the form

$$\sigma_{ij} = c_{ijkl}\varepsilon_{kl} \equiv \sum_{k=1}^{3}\sum_{l=1}^{3} c_{ijkl}\varepsilon_{kl}, \tag{2.25}$$

where c_{klpq} is a fourth-order tensor called *stiffness coefficient*, with $3^4 = 81$ components. The reverse relation is possible and it gives $s = c^{-1}$, which is know as the *material compliance coefficients*. It can be proved that, due to the symmetry of the strain and stress tensors, the amount of different components of the stiffness coefficient can be reduced to 36, which lead to the constitutive equations for a *anisotropic material*.

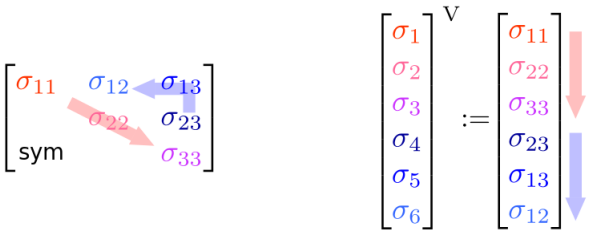

Figure 2.2: Graphic representation of Voigt notation.

It is common to represent the stress-strain relations given by the generalized Hooke's Law by employing the *Voigt* notation. In multilinear algebra, the Voight notation is a way to represent a symmetric tensor by reducing its order, by following a simple mnemonic rule, which is graphically represented in figure 2.2. Thus, the stress tensor is represented in Voigt notation as

$$\underline{\boldsymbol{\sigma}} := \begin{bmatrix} \sigma_{11} \\ \sigma_{22} \\ \sigma_{33} \\ \sigma_{23} \\ \sigma_{13} \\ \sigma_{12} \end{bmatrix} = \begin{bmatrix} \sigma_1 \\ \sigma_2 \\ \sigma_3 \\ \sigma_4 \\ \sigma_5 \\ \sigma_6 \end{bmatrix}, \tag{2.26}$$

the strain tensor can be notated in a similar way, as

$$\underline{\boldsymbol{\varepsilon}} := \begin{bmatrix} \varepsilon_1 \\ \varepsilon_2 \\ \varepsilon_3 \\ 2\varepsilon_4 \\ 2\varepsilon_5 \\ 2\varepsilon_6 \end{bmatrix} = \begin{bmatrix} \varepsilon_{11} \\ \varepsilon_{22} \\ \varepsilon_{33} \\ 2\varepsilon_{23} \\ 2\varepsilon_{13} \\ 2\varepsilon_{12} \end{bmatrix}, \tag{2.27}$$

where factors of 2 result from the symmetry of the strain tensor, i.e., for each $k \neq l$, the corresponding strain-tensor component appears twice in the summation on the right-hand side of equations (2.25), as ε_{kl} and as ε_{lk}. The 36 different coefficients of the stiffness coefficient tensor can be represented in this notation as

$$[c] = \begin{bmatrix} c_{1111} & c_{1122} & c_{1133} & c_{1123} & c_{1131} & c_{1112} \\ c_{2211} & c_{2222} & c_{2233} & c_{2223} & c_{2231} & c_{2212} \\ c_{3311} & c_{3322} & c_{3333} & c_{3323} & c_{3331} & c_{3312} \\ c_{2311} & c_{2322} & c_{2333} & c_{2323} & c_{2331} & c_{2312} \\ c_{3111} & c_{3122} & c_{3133} & c_{3123} & c_{3131} & c_{3112} \\ c_{1211} & c_{1222} & c_{1233} & c_{1223} & c_{1231} & c_{1212} \end{bmatrix} \equiv \begin{bmatrix} C_{11} & C_{12} & C_{13} & C_{14} & C_{15} & C_{16} \\ C_{21} & C_{22} & C_{23} & C_{24} & C_{25} & C_{26} \\ C_{31} & C_{32} & C_{33} & C_{34} & C_{35} & C_{36} \\ C_{41} & C_{42} & C_{43} & C_{44} & C_{45} & C_{46} \\ C_{51} & C_{52} & C_{53} & C_{54} & C_{55} & C_{56} \\ C_{61} & C_{62} & C_{63} & C_{64} & C_{65} & C_{66} \end{bmatrix} =: \boldsymbol{C}, \tag{2.28}$$

where the matrix $\boldsymbol{C}$ is called the *elasticity matrix*. Then, in Voigt notation, the generalized Hooke's Law for a anisotropic material is given by

$$\begin{bmatrix} \sigma_1 \\ \sigma_2 \\ \sigma_3 \\ \sigma_4 \\ \sigma_5 \\ \sigma_6 \end{bmatrix} = \begin{bmatrix} C_{11} & C_{12} & C_{13} & C_{14} & C_{15} & C_{16} \\ C_{21} & C_{22} & C_{23} & C_{24} & C_{25} & C_{26} \\ C_{31} & C_{32} & C_{33} & C_{34} & C_{35} & C_{36} \\ C_{41} & C_{42} & C_{43} & C_{44} & C_{45} & C_{46} \\ C_{51} & C_{52} & C_{53} & C_{54} & C_{55} & C_{56} \\ C_{61} & C_{62} & C_{63} & C_{64} & C_{65} & C_{66} \end{bmatrix} \begin{bmatrix} \varepsilon_1 \\ \varepsilon_2 \\ \varepsilon_3 \\ 2\varepsilon_4 \\ 2\varepsilon_5 \\ 2\varepsilon_6 \end{bmatrix}, \tag{2.29}$$

which, in sort, can be written as

$$\underline{\boldsymbol{\sigma}} = \boldsymbol{C}\underline{\boldsymbol{\varepsilon}}. \tag{2.30}$$

2.6.2 Strain-energy density function

A further reduction in the stiffness coefficient tensor is possible, but to achieve this it is necessary to stipulate the existence of the Strain-energy density function. For elastic continua, all the expended energy is assumed to be stored in the strained continuum as potential energy. In other words, a conservative system is considered. The aim is to formulate the corresponding potential-energy function. To motivate such a formulation, consider a force, u, acting on a conservative system to increase the potential energy, $U(x)$, of this system. We can write the components of such a force as $\partial U/\partial x_i = F_i$, where $i \in \{1, 2, 3\}$. By analogy, it is postulated a Strain-energy density function $W(\boldsymbol{\varepsilon})$, such that

$$\sigma_{ij} = \frac{\partial W(\varepsilon_{ij})}{\varepsilon_{ij}}. \tag{2.31}$$

It is possible to start by giving $W(\varepsilon_{ij})$ a general form, and then, arrive to the following formulae

$$W(\varepsilon_{ij}) = \frac{1}{2}\sigma_{ij}\varepsilon_{ij} = \frac{1}{2}c_{ijkl}\varepsilon_{kl}\varepsilon_{ij}, \tag{2.32}$$

to review this derivation consult [Pujol, 2003]. Once the previous expression for $W(\boldsymbol{\varepsilon})$ is obtained, substituting in the generalised Hooke's Law (2.25), yields

$$c_{ijkl} = \frac{\partial \sigma_{ij}}{\partial \varepsilon_{kl}} = \frac{\partial^2 W(\varepsilon)}{\partial \varepsilon_{ij}\partial \varepsilon_{kl}} = \frac{\partial^2 W(\varepsilon)}{\partial \varepsilon_{kl}\partial \varepsilon_{ij}} = c_{klij}, \tag{2.33}$$

which leads to the symmetry $c_{ijkl} = c_{klij}$, in Voigt notation, is represented as

$$C_{ij} = C_{ji}. \tag{2.34}$$

Therefore, the symmetric elasticity matrix is given by

$$\boldsymbol{C} = \begin{bmatrix} C_{11} & C_{12} & C_{13} & C_{14} & C_{15} & C_{16} \\ C_{12} & C_{22} & C_{23} & C_{24} & C_{25} & C_{26} \\ C_{13} & C_{23} & C_{33} & C_{34} & C_{35} & C_{36} \\ C_{14} & C_{24} & C_{34} & C_{44} & C_{45} & C_{46} \\ C_{15} & C_{25} & C_{35} & C_{45} & C_{55} & C_{56} \\ C_{16} & C_{26} & C_{36} & C_{46} & C_{56} & C_{66} \end{bmatrix}. \tag{2.35}$$

This symmetry reduces the independent coefficients to 21.

The elasticity matrix (2.35) defines the stress-strain equations followed by a general elastic continuum that obeys Hooke's law. Materials following these general stress-strain relations are known as *Triclinic Materials*.

It can also be proved that the *potential strain energy*, U, is related with the strain energy density function as

$$U = \int_V W dV, \tag{2.36}$$

for further details consult [Pujol, 2003].

2.6.3 Material Symmetry

Materials can possess certain symmetries. This means that a material's property can be measure in several different orientations of the coordinate system and obtain the same result each time. In other words, it is not possible to detect the transformations of the reference coordinate system by mechanical experiments. This invariance to the orientation of the coordinate system is called material symmetry. In an adequately chosen coordinate system, the elasticity matrix's form can make recognisable this continuum's symmetry. This symmetry is indicative of the properties exhibited by the material represented by this continuum.

The symmetry transformations can be represented by an orthogonal second order tensor

$$\boldsymbol{Q} = Q_{ij}\boldsymbol{e}_i \otimes \boldsymbol{e}_j, \tag{2.37}$$

such that $\boldsymbol{Q} = \boldsymbol{Q}^T$, and characterised by its determinant as

$$det(Q_{ij}) = \begin{cases} +1, & \text{rotation,} \\ -1, & \text{reflection.} \end{cases} \tag{2.38}$$

The invariance of the stiffness tensor under these transformations is expressed as follows

$$c_{ijkl} = Q_{ip}Q_{jq}Q_{kr}Q_{ls}c_{pqrs}. \tag{2.39}$$

The more the internal symmetries, the simpler the structure of the stiffness tensor. The set of all orthogonal transformations given by matrices $\boldsymbol{Q}$ to which the elastic properties of a given continuum are invariant is called the symmetry group of that continuum.

2.6.4 Isotropic linear elastic materials

A continuum whose symmetry group contains all orthogonal transformations is said to be isotropic. For an isotropic continuum, all coordinate systems are natural coordinate systems; hence, no particular orientation is required.

It can be proved (see, for example [Slawinski, 2010]), that the most general fourth-order isotropic symmetric tensor is given by

$$c_{ijkl} = \lambda\delta_{ij}\delta_{kl} + \mu(\delta_{ik}\delta_{jl} + \delta_{il}\delta_{jk}), \tag{2.40}$$

where λ and μ are real numbers, and δ_{ij} is the Kronecker delta.

Therefore, using the strain tensor symmetry, the constitutive relations for *isotropic materials* in tensor formulation are given by

$$\sigma_{ij} = \lambda\delta_{ij}\varepsilon_{kk} + 2\mu\varepsilon_{ij} = \lambda\delta_{ij}uk, k + 2\mu(u_{i,j} + u_{j,i}), \tag{2.41}$$

and, in Voigt notation, as

$$\begin{bmatrix}\sigma_1\\ \sigma_2\\ \sigma_3\\ \sigma_4\\ \sigma_5\\ \sigma_6\end{bmatrix} = \begin{bmatrix}2\mu+\lambda & \lambda & \lambda & 0 & 0 & 0\\ \lambda & 2\mu+\lambda & \lambda & 0 & 0 & 0\\ \lambda & \lambda & 2\mu+\lambda & 0 & 0 & 0\\ 0 & 0 & 0 & \mu & 0 & 0\\ 0 & 0 & 0 & 0 & \mu & 0\\ 0 & 0 & 0 & 0 & 0 & \mu\end{bmatrix}\begin{bmatrix}\varepsilon_1\\ \varepsilon_2\\ \varepsilon_3\\ 2\varepsilon_4\\ 2\varepsilon_5\\ 2\varepsilon_6\end{bmatrix}, \tag{2.42}$$

where λ is known as the first Lame parameter and μ as the second Lame parameter or the *shear modulus*. The Lamé parameters, are constants used to describe the elastic properties of a material. They are related to the Young's modulus, E, and Poisson's ratio, ν, as follows:

$$\lambda = \frac{E\cdot\nu}{(1+\nu)(1-2\nu)}, \qquad \mu = \frac{E}{2(1+\nu)} \quad \text{in three dimensions,} \tag{2.43}$$

and as

$$\lambda = \frac{E\cdot\nu}{(1+\nu)(1-\nu)}, \qquad \mu = \frac{E}{2(1+\nu)} \quad \text{in two dimensions.} \tag{2.44}$$

The Young's modulus represents the material's stiffness or ability to resist deformation under an applied load. It quantifies the ratio of stress to strain in the linear elastic range. Poisson's ratio, on the other hand, characterizes the lateral contraction or expansion that occurs when a material is stretched or compressed in one direction. It is defined as the negative ratio of the transverse strain to the longitudinal strain. Young's modulus and Poisson's ratio are commonly obtained experimentally. Thus, the generalised Hooke's Law in terms of the Young's modulus and the Poisson's ratio is given by

$$\begin{bmatrix}\sigma_1\\ \sigma_2\\ \sigma_3\\ \sigma_4\\ \sigma_5\\ \sigma_6\end{bmatrix} = \frac{E}{(1+\nu)(1-2\nu)}\begin{bmatrix}1-\nu & \nu & \nu & 0 & 0 & 0\\ \nu & 1-\nu & \nu & 0 & 0 & 0\\ \nu & \nu & 1-\nu & 0 & 0 & 0\\ 0 & 0 & 0 & \frac{1-2\nu}{2} & 0 & 0\\ 0 & 0 & 0 & 0 & \frac{1-2\nu}{2} & 0\\ 0 & 0 & 0 & 0 & 0 & \frac{1-2\nu}{2}\end{bmatrix}\begin{bmatrix}\varepsilon_1\\ \varepsilon_2\\ \varepsilon_3\\ 2\varepsilon_4\\ 2\varepsilon_5\\ 2\varepsilon_6\end{bmatrix}. \tag{2.45}$$

Plane stress

In continuum mechanics, a material is said to be under plane stress if the stress tensor is zero across a particular plane. In other words, a plane stress state is defined to be one in which all transverse stresses are negligible (see figure 2.3). This case is particularly important for the present study as it is often the case for thin plates.

If the first two coordinate axes are chosen to be perpendicular to the direction of

[3]Image credits: By Sanpaz - Own work, CC BY-SA 3.0, `https://commons.wikimedia.org/w/index.php?curid=5717540`

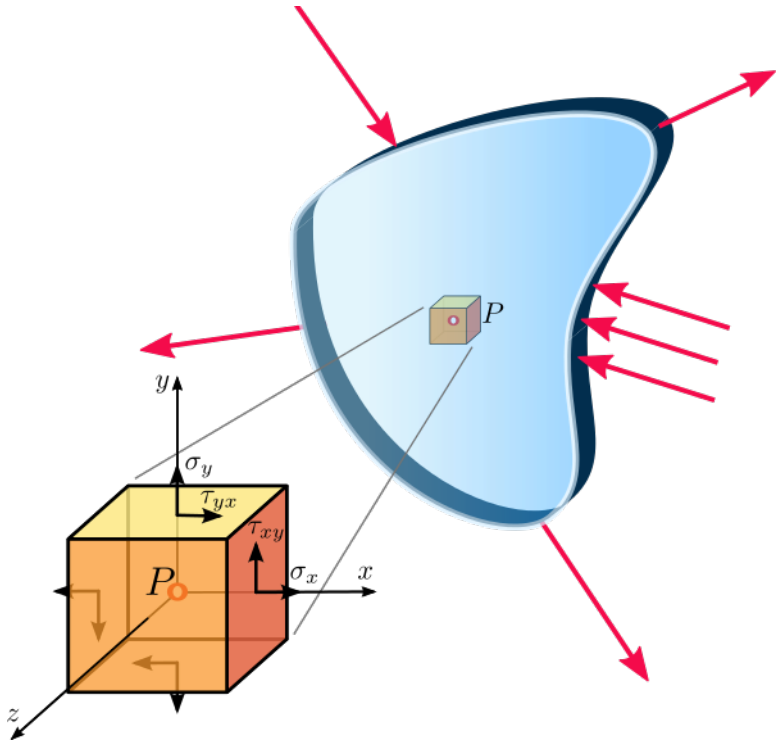

Figure 2.3: Graphical representation of plane stress state[3].

zero stress, then, the plane stress conditions are

$$\sigma_{31} = \sigma_{13} = \sigma_{32} = \sigma_{23} = \sigma_{33} = 0,$$

and the stress tensor will have the form

$$\boldsymbol{\sigma} = \begin{bmatrix} \sigma_{11} & \sigma_{12} & 0 \\ \sigma_{21} & \sigma_{22} & 0 \\ 0 & 0 & 0 \end{bmatrix} \equiv \begin{bmatrix} \sigma_x & \tau_{xy} & 0 \\ \tau_{yx} & \sigma_y & 0 \\ 0 & 0 & 0 \end{bmatrix}. \tag{2.46}$$

Thus, the stress state can be represented by a tensor of dimension 2, or as a 2×2 matrix rather than 3×3, this is

$$\sigma_{ij} = \begin{bmatrix} \sigma_{11} & \sigma_{12} \\ \sigma_{21} & \sigma_{22} \end{bmatrix} \equiv \begin{bmatrix} \sigma_x & \tau_{xy} \\ \tau_{yx} & \sigma_y \end{bmatrix}. \tag{2.47}$$

In this case, Hooke's Law takes the form

$$\begin{bmatrix} \sigma_{11} \\ \sigma_{22} \\ \sigma_{12} \end{bmatrix} = \frac{E}{1-\nu^2} \begin{bmatrix} 1 & \nu & 0 \\ \nu & 1 & 0 \\ 0 & 0 & \frac{1-\nu}{2} \end{bmatrix} \begin{bmatrix} \varepsilon_{11} \\ \varepsilon_{22} \\ 2\varepsilon_{12} \end{bmatrix}. \tag{2.48}$$

Further details about plane stress state can be consulted in [Meyers and Chawla, 2008] or in [Salençon, 2012].

2.7 Energy Principles and Variational Methods

The governing equations of a continuum can be derived by applying the laws of physics. In the context of solid mechanics problems, these laws can be expressed in different forms. One approach is the principle of conservation of linear momentum, which leads to the equations of motion. The equations of motion can be obtained using either Newton's Second Law of motion or the principle of virtual displacements. The former approach is known as the vector approach, while the latter is referred to as the energy approach.

Newton's laws are employed in the vector approach to determine the governing equations by isolating a representative volume element of the structure along with all the applied and reactive forces. The vector sum of all static and dynamic forces and moments acting on the element is set to zero, resulting in the equations of motion. This method is straightforward for simple mechanical systems, where the free-body diagram can be readily established. However, for complex systems, this approach can become cumbersome and challenging. Additionally, determining the appropriate boundary conditions to use with the derived equations may not always be clear.

On the other hand, the energy approach sets the total work done or energy stored in the body due to actual forces to zero, considering virtual displacements that satisfy the geometric constraints of the body. This approach not only yields the equations of motion but also provides the force boundary conditions and guides the specification of geometric boundary conditions. Additionally, the energy expressions derived from this approach are useful for obtaining approximate solutions through direct variational methods like the Ritz and finite element methods.

Overall, the energy approach offers advantages in terms of providing a comprehensive understanding of the governing equations, force boundary conditions, and geometric constraints, while also enabling the application of variational methods for approximate solutions.

This section will briefly introduce the main ideas involving energy and variational methods. The main concepts of Variational Calculus and the definitions and properties involving the *variational operator*, δ, are summarised in appendix A. Most of the ideas presented in this section can be consulted in [Reddy, 2006]. The summation convention of repeated index is always applied in this section.

2.7.1 Virtual Displacements and Forces

Considering purely geometrical aspects, a given mechanical system can exhibit numerous possible configurations that adhere to the geometric constraints placed upon it. However, out of all these possible configurations, only one corresponds to the equilibrium configuration of the system under the specified forces. This particular configuration satisfies Newton's second law, which encompasses the equations of equilibrium or motion for the system.

The set of configurations that meet the geometric constraints but may not satisfy Newton's second law is referred to as the set of admissible configurations. These configurations are constrained to a small region surrounding the true configuration

and are obtained through *infinitesimal* variations of the true configuration. During these variations, the geometric constraints of the system are maintained, and all forces remain fixed at their actual values. It is important to note that these variations, known as virtual displacements, need not be related to the actual displacements that might occur due to changes in applied loads. The term "virtual" indicates that these displacements are imagined to occur while the actual loads remain constant. *At the boundary points where geometric boundary conditions are specified, the virtual displacements are assumed to be zero.*

Similarly to the concept of virtual displacements, one can consider the notion of virtual forces acting on a system. These virtual forces constitute a collection of forces that maintain equilibrium within themselves. These forces can encompass both internal and external forces and are not necessarily related to the actual forces present in the system.

2.7.2 External and Internal Virtual Work

When a force acts on a material point and moves through a displacement, the work done by the force is defined by the projection of the force in the direction of the displacement times the magnitude of the displacement. The work done by the actual forces through virtual displacements or the work done by virtual forces through actual displacements is called virtual work. The virtual work done by actual forces $\boldsymbol{F}$ in a body Ω in moving through the virtual displacements $\delta\mathbf{u}$ is given by

$$\delta W = \int_{\Omega} \boldsymbol{F} \cdot \delta\mathbf{u}\, dv, \tag{2.49}$$

where dv represents an infinitesimal volume element within the body.

The virtual work concept allows for the evaluation of the total work done by actual forces through infinitesimal virtual displacements.

Similar to the virtual displacements, it can be imagined to apply forces on a body without disturbing its equilibrium. Then the virtual work done by virtual forces $\delta\boldsymbol{F}$ in moving through the actual displacement $\mathbf{u}$ is given by:

$$\delta W^* = \int_{\Omega} \delta\boldsymbol{F} \cdot \mathbf{u}\, dv. \tag{2.50}$$

This concept of virtual work allows us to evaluate the total work done by virtual forces through actual displacements.

When a deformable body in equilibrium undergoes virtual displacements, work is performed by both externally applied forces and internally developed forces. The work done by externally applied forces as they move through their respective virtual displacements is referred to as external virtual work, denoted by δW_E. The work done by internal forces as they move through the virtual displacements is called internal virtual work, denoted by δW_I. The internal energy W_I of the body encompasses various types of energy, such as mechanical, thermal, chemical, etc. However, this particular study, focuses solely on the internal energy resulting from mechanical forces causing deformation, known as strain energy, denoted by U. For rigid bodies that undergo

no geometric changes and therefore do not develop internal forces, the internal work done, W_I, is equal to zero. In the following, expressions for the external and internal virtual works of a deformable body will be derive.

External Virtual Work

The external virtual work done due to virtual displacements δu in a solid body Ω subjected to body forces $\mathbf{f}$ per unit volume and surface tractions $\mathbf{T}$ per unit area of the boundary Γ_σ is given by

$$\delta W_E = -\left(\int_\Omega \mathbf{f}\cdot\delta\mathbf{u}\,dv + \int_{\Gamma_\sigma} \mathbf{T}\cdot\delta\mathbf{u}\,ds\right), \tag{2.51}$$

where ds denotes the infinitesimal surface area element Γ_σ denotes the portion of the boundary on which stresses are specified. The negative sign indicates that the work is performed on the body. It is understood that the displacements are specified on the remaining portion $\Gamma_u = \Gamma - \Gamma_\sigma$ of the boundary Γ. Therefore, the virtual displacements are zero on Γ_u, irrespective of whether u is specified to be zero or not.

Analogously, the external virtual work done due to virtual body forces $\delta\mathbf{f}$ and surface tractions $\delta\mathbf{t}$ on Γ_u of a solid body Ω in moving through the respective actual displacements $\mathbf{u}$ is called the complementary virtual work δW_E^*, and it is given by

$$\delta W_E^* = -\left(\int_\Omega \delta\mathbf{f}\cdot\mathbf{u}\,dv + \int_{\Gamma_u} \delta\mathbf{t}\cdot\mathbf{u}\,ds\right). \tag{2.52}$$

Internal Virtual Work

The deformations of a body are induced by the applied forces, resulting in internal stresses within it. These deformations can be quantified by measuring the strain, which describe the relative movement of material particles. The internal stress field associated with these forces causes displacements of the material particles, corresponding to the strain field present within the body. Consequently, work is performed. It is important to note that the work done on the body by external forces is responsible for the internal work within the body.

The internal virtual work, resulting from a virtual displacement $\delta\mathbf{u}$, can be computed as follows. Consider an infinitesimal material element with a volume of $dv = dx_1dx_2dx_3$ within the body. This material element experiences small virtual strains $\delta\varepsilon_{ij}$ due to the virtual displacements δu_i, given by

$$\delta\varepsilon_{ij} = \frac{1}{2}\left(\frac{\partial\delta u_i}{\partial x_j} + \frac{\partial\delta u_j}{\partial x_i}\right). \tag{2.53}$$

The total virtual work done, or virtual strain energy δU stored, by forces due to all the stresses in a volume element in moving through their respective displacements

is given by

$$(\sigma_{11}\delta\varepsilon_{11} + \sigma_{22}\delta\varepsilon_{22} + \sigma_{33}\delta\varepsilon_{33} + 2\sigma_{12}\delta\varepsilon_{12} + 2\sigma_{13}\delta\varepsilon_{13} + 2\sigma_{23}\delta\varepsilon_{23})\, dx_1dx_2dx_3 = \sigma_{ij}\delta\varepsilon_{ij}\, dv. \tag{2.54}$$

The virtual strain energy per unit volume is called the virtual strain energy density, $\delta U_0 = \sigma_{ij}\delta\varepsilon_{ij}$. The total internal virtual work done, δW_I, is obtained by integrating the above expression over the entire volume of the body,

$$\delta W_I = \delta U = \int_\Omega \sigma_{ij}\delta\varepsilon_{ij} dv = \int_\Omega \boldsymbol{\sigma} : \delta\boldsymbol{\varepsilon} dv, \tag{2.55}$$

where " : " denotes the tensor *double dot* product. The expression (2.55) is also called the *virtual strain energy*, and is valid for any material body irrespective of its constitutive behaviour. Although (2.55) was derived for infinitesimal strain case, it also holds for the finite strain case.

The internal virtual work done by virtual stresses $\delta\sigma_{ij}$ in moving through the actual strains ε_{ij}, called the *complementary internal virtual* work δW_I^*, is given by

$$\delta W_I^* = \delta U^* = \int_\Omega \varepsilon_{ij}\delta\sigma_{ij} dv = \int_\Omega \boldsymbol{\varepsilon} : \delta\boldsymbol{\sigma} dv, \tag{2.56}$$

and is also know as *virtual complementary strain energy*. The virtual forces $(\delta\mathbf{f}, \delta\mathbf{T})$ and virtual stresses $(\delta\boldsymbol{\sigma})$ should be such that the stress equilibrium equations,

$$\frac{\partial\delta\sigma_{ij}}{\partial x_j} + \rho\delta f_i = 0 \qquad \text{or} \qquad \nabla\cdot\delta\boldsymbol{\sigma} + \rho\delta\mathbf{f} = \mathbf{0}, \tag{2.57}$$

as well as the stress boundary conditions,

$$\delta\sigma_{ij}n_j = \delta T \qquad \text{or} \qquad \delta\sigma\cdot\mathbf{n} = \mathbf{T} = \mathbf{0}, \tag{2.58}$$

are satisfied.

2.7.3 Energy principles

The Principle of Virtual Displacements

Consider a continuous body **B** in equilibrium, subjected to body forces **f** and surface tractions **T**, with reference configuration C^0, considered as the initial configuration, and let the volume of the body be denoted as Ω. Within the total boundary Γ of the region Ω, there are two disjoint portions: Γ_u, where the displacements are specified to be $\hat{\mathbf{u}}$, and Γ_σ, where the tractions are specified as $\hat{\mathbf{T}}$. Let the displacement vector **u** be the equilibrium configuration of the body. Then, the admissible configurations are defined by sufficiently differentiable functions that satisfy the geometric boundary conditions $\mathbf{u} = \hat{\mathbf{u}}$ on Γ_u.

In the case of a body in equilibrium, the actual configuration, out of all admissible configurations, is characterised by the property that the total virtual work performed

is equal to zero. Thus, the **principle of virtual displacements** can be stated as follows: *If a continuous body is in equilibrium, the virtual work of all actual forces in moving through a virtual displacement is zero:*

$$\delta W_I + \delta W_E \equiv \delta W = 0. \tag{2.59}$$

By writing down the previous definitions of internal and external virtual work, yields

$$\int_\Omega \boldsymbol{\sigma} : \delta\boldsymbol{\varepsilon} dv - \int_\Omega \mathbf{f} \cdot \delta\mathbf{u}\, dv - \int_{\Gamma_\sigma} \mathbf{T} \cdot \delta\mathbf{u}\, ds = 0, \tag{2.60}$$

which, in terms of rectangular components (with sum on repeated subscripts implied), takes the form

$$\int_\Omega (\sigma_{ij}\delta\varepsilon_{ij} - \rho f_i \delta u_i) dv - \int_{\Gamma_\sigma} T_i \delta u_i ds = 0. \tag{2.61}$$

The virtual strain, $\delta\varepsilon_{ij}$,in terms of the virtual displacements δu_i is given by

$$\delta\varepsilon_{ij} = \frac{1}{2}(\delta u_{i,j} + \delta u_{j,i}), \qquad \text{with} \qquad u_{i,j} := \frac{\partial u_i}{\partial x_j}. \tag{2.62}$$

Then,

$$\sigma_{ij}\delta\varepsilon_{ij} = \frac{1}{2}\sigma_{ij}(\delta u_{i,j} + \delta u_{j,i}) = \frac{1}{2}(\sigma_{ij}\delta u_{i,j} + \sigma_{ij}\delta u_{j,i}), \tag{2.63}$$

as the stress tensor in symmetric,

$$\sigma_{ij}\delta u_{j,i} = \sigma_{ji}\delta u_{i,j} = \sigma_{ij}\delta u_{i,j}, \tag{2.64}$$

thus

$$\sigma_{ij}\delta\varepsilon_{ij} = \frac{1}{2}\sigma_{ij}(\delta u_{i,j} + \delta u_{j,i}) = \frac{1}{2}(\sigma_{ij}\delta u_{i,j} + \sigma_{ij}\delta u_{i,j}) = \sigma_{ij}\delta u_{i,j} = \sigma_{ji}\delta u_{i,j}. \tag{2.65}$$

Therefore, the volume integral in (2.61) can be written as

$$\int_\Omega (\sigma_{ij}\delta\varepsilon_{ij} - \rho f_i \delta u_i) dv = \int_\Omega (\sigma_{ji}\delta u_{i,j} - \rho f_i \delta u_i) dv. \tag{2.66}$$

The term involving the stress tensor can be modified by applying the divergence theorem as

$$\int_\Omega \sigma_{ji}\delta u_{i,j} dv = -\int_\Omega \sigma_{ji,j}\delta u_i dv + \int_\Gamma \sigma_{ji} n_j \delta u_i. \tag{2.67}$$

Therefore, since $\delta u_i = 0$ on Γ_u and $\Gamma_\sigma = \Gamma - \Gamma_u$, the principle of virtual displacements takes the form

$$-\int_\Omega (\sigma_{ji,j} + \rho f_i)\delta u_i dv + \int_{\Gamma_\sigma} (\sigma_{ji} n_j - T_i)\delta u_i ds = 0 \tag{2.68}$$

Because the virtual displacements are arbitrary in Ω_0 (the interior of Ω), and on Γ_σ,

equation (2.68) yields to the following Euler-Lagrange (see appendix A):

$$\sigma_{ji,j} + \rho f_i = 0, \qquad \text{in} \qquad \Omega, \tag{2.69}$$

$$\sigma_{ji} n_j - T_i = 0, \qquad \text{in} \qquad \Gamma_\sigma. \tag{2.70}$$

Equations (2.69) are nothing but the equilibrium equations of the 3-D elasticity previously mention in equation (2.16). The boundary conditions in (2.70) are the natural boundary conditions for a body in equilibrium.

Hamilton's Principle

The principle of virtual displacements is applicable to static equilibrium conditions of solid bodies. To extend this principle to dynamics, Hamilton's principle is introduced. Hamilton's principle, a dynamic version of the principle of virtual displacements, considers a dynamical system characterised by two energy functions: kinetic energy K and potential energy W. As previously mentioned, the kinetic energy of a continuous body is given by

$$K = \frac{1}{2} \int_\Omega \rho \frac{\partial \mathbf{u}}{\partial t} \cdot \frac{\partial \mathbf{u}}{\partial t} dv, \tag{2.71}$$

where $\frac{\partial \mathbf{u}}{\partial t}$ denotes the velocity of the material particle. The complete determination of motion in a body requires the incorporation of the kinematic conditions and constitutive equations, previously derived. The actual path followed by a material particle in position $\boldsymbol{x}$ within the body is varied, while satisfying the kinematic (essential) boundary conditions, to a new path $\mathbf{u} + \delta\mathbf{u}$. The admissible variation $\delta\mathbf{u}$ of the path is assumed to differ from the actual path except at the initial time t_1 and final time t_2. Therefore, an admissible variation $\delta\mathbf{u}$ must satisfy the following conditions:

$$\begin{aligned} \delta\mathbf{u}(\boldsymbol{x}, t) &= 0 \quad \text{on}\, \Gamma_u \,\text{for all}\, t, \\ \delta\mathbf{u}(\boldsymbol{x}, t_1) &= \delta\mathbf{u}(\boldsymbol{x}, t_2) = 0, \quad \text{for all}\, \boldsymbol{x}. \end{aligned} \tag{2.72}$$

Hamilton's principle states that *of all possible paths that a material particle could travel from its position at time t_1 to its position at time t_2, its actual path will be one for which the integral*

$$\int_{t_1}^{t_2} (K - W) dt \tag{2.73}$$

is an extremum.

The difference between the kinetic and potential energies is called the Lagrangian function

$$L = K - W = K - W_I - W_E. \tag{2.74}$$

Thus, Hamilton's principle can be expressed as

$$\int_{t_1}^{t_2} (\delta L) dt = \int_{t_1}^{t_2} (\delta K - \delta W_I - \delta W_E) dt = 0. \tag{2.75}$$

The requirement that $\delta\mathbf{u}$ be zero at the final time when $\mathbf{u}(\boldsymbol{x}, t_2)$ is not known or

specified is often a point of discussion and, for this reason, Hamilton's principle is sometimes referred to as a pseudo variational principle. The principle gives the equations of motion, but not the initial conditions. The procedure to obtain the equations of motion, consits in finding δL and solve (2.75) by applying the Euler-Lagrange equations.

Chapter 3

Plate Vibrations

3.1 Introduction

We are interested in modelling the vibrations of micro-scale circular polymer *membrane-like* device, with a concentric heterogeneous coat of some metallic material. As mentioned in the introductory chapter, the micro-scale polymer *membrane* lacks of in-plane tension, therefore, the natural model for these devices is a *plate* rather than a membrane.

The primary goal of this chapter is to establish the governing equations for the classical theory of plates. Subsequently, an analytical solution will be provided specifically for homogeneous circular plates. Finally, the modified equations of motion will be derived for non-homogeneous plates incorporating damping, along with an exploration of its implications. The modified model will be further addressed and solved using the Finite Difference Method in subsequent chapters.

3.2 Classical theory of plates

A plate is a structural element characterised by its plan-form dimensions being significantly larger than its thickness. When it is subjected to loads, it can induce both bending deformation and stretching. Due to the relatively small thickness, it is often unnecessary to employ 3D elasticity equations for modelling plates. Instead, simplified 2D plate theories can be developed to analyse the deformation and stresses in plate structures.

3.2.1 Semi-inverse method and Kirchhoff hypothesis

Plates theories are commonly obtain by proposing an *Ansatz* or a reasonable guess to the form of the displacement field or stress field, leaving enough freedom in the assumed field to satisfy the equations of elasticity. Such a formulation is also known as a semi-inverse method, and is explicitly mentioned in texts like [Reddy, 2006] and [Chaigne and Kergomard, 2016], and implicitly texts like [Leissa and Qatu, 2011] and [Graff, 1975].

In the case of beams, plates, and shells, the displacement field is proposed to be given in terms of unknown functions ϕ_i^j of the surface coordinates (x, y) and time t, as

$$u_i(x, y, z, t) = \sum_{j=0}^{N} (z)^j \phi_i^j(x, y, t) \tag{3.1}$$

The specific form of equation (3.1) depends on the kinematics of deformation to be included.

The classical plate theory is one in which the displacement field is based on the *Kirchhoff hypothesis*, which consists of the following three parts [Reddy, 2006]:

1. Straight lines perpendicular to the mid-surface (i.e., transverse normals) before deformation remain straight after deformation.

2. The transverse normals do not experience elongation (i.e., they are in- extensible).

3. The transverse normals rotate such that they remain perpendicular to the middle surface after deformation.

The consequences of the Kirchhoff hypothesis can be examined in the context of a plate with uniform thickness, h. The rectangular Cartesian coordinates (x, y, z) are utilised, where the xy-plane aligns with the geometric middle plane of the plate, and the positive z-coordinate represents the upward direction. The displacements of a point along the (x, y, z) coordinates are given by (u, v, w). Considering the movement of a material point within the plate, from its original position in the undeformed state to the position $(x + u, y + v, z + w)$ in the deformed state, some conclusions can be drawn based on assumptions 1 and 2. These assumptions imply the inextensibility of a transverse normal. As a result, the thickness normal strain, represented by ε_{zz}, is determined to be zero:

$$\varepsilon_{zz} = \frac{\partial w}{\partial z} = 0. \tag{3.2}$$

Consequently, the displacement component w is independent of the z coordinate, indicating that it does not vary along the thickness of the plate, then

$$w(x, y, z, t) \equiv w_0(x, y, t), \tag{3.3}$$

where w_0 denote the displacement of a material point at $(x, y, 0)$ in the z-direction. From here on, w and w_0 will be used indistinctly, as they both represent the same quantity, the *bending deflection* of the plate (also known as the plate's *deflection*, given that it does no vary along the plate's thickness). The third assumption results in zero transverse shear strains, this is,

$$\varepsilon_{xz} = \frac{\partial u}{\partial z} + \frac{\partial w}{\partial x} = 0, \qquad \varepsilon_{yz} = \frac{\partial v}{\partial z} + \frac{\partial w}{\partial y} = 0. \tag{3.4}$$

Therefore, a reasonable Ansatz for the displacement field that satisfies the Kirchhoff

hypothesis, can be given by

$$u(x,y,z) = -z\frac{\partial w}{\partial x} + u_0(x,y), \qquad v(x,y,z) = -z\frac{\partial w}{\partial y} + v_0(x,y), \tag{3.5}$$

where u_0 and v_0 represent the value of u and v, respectively, at the point $(x, y, 0)$.

If the mid-plane surface is represented by $\Omega \subset \mathbb{R}^2$, by additionally imposing that the displacement along Ω only depends on the variation of the traversal direction, this is,

$$u_0(x,y) = v_0(x,y) = 0, \qquad \forall (x,y) \in \Omega, \tag{3.6}$$

the displacement field Ansatz is modified to only be given in terms of the z-direction displacement,w, as

$$u(x,y,z,t) = -z\frac{\partial w}{\partial x}, \quad v(x,y,z,t) = -z\frac{\partial w}{\partial y}, \quad w(x,y,z,t) = w_0(x,y,t) \equiv w(x,y,t). \tag{3.7}$$

Thus, the strain tensor components have the form

$$\varepsilon_{xx} = -z\frac{\partial^2 w}{\partial x^2}, \quad \varepsilon_{yy} = -z\frac{\partial^2 w}{\partial y^2}, \quad \varepsilon_{xy} = -z\frac{\partial^2 w}{\partial x \partial y}, \tag{3.8}$$

and

$$\varepsilon_{xz} = \varepsilon_{yz} = \varepsilon_{zz} = 0. \tag{3.9}$$

The displacement field given by (3.7) is the proposed by the semi-inverse method. Thus, the solution to the plate dynamics can be given only in terms of the z-displacement, $w(x, y, t)$. By nullifying the in-plane displacement, as expressed in equation (3.6), the in-plane tension forces, also known as *membrane forces*, are neglected. Therefore, this model suits the necessities for the micro-tabla device, as mentioned in the introduction of this text (see section 1.2).

3.2.2 Equation of Motion for Transverse Vibrations

The equation of motion for a plate following the previously mentioned displacements restrictions will be derive, adding a traverse external body force, $q(x, y)$, acting on the plate. The undeformed middle plane of the plate is denoted by Ω. The total domain of the plate is the Cartesian product $V = \Omega \times [h/2, h/2]$. The boundary of the total domain consists of the top surface ($z = -h/2$), bottom surface ($z = -h/2$), and the edge $\Gamma := \hat{\Gamma} \times [-h/2, h/2]$, where $\hat{\Gamma} = \partial\Omega$. In general, Γ is a curved surface, with outward normal $\hat{\mathbf{n}} = n_x\hat{\boldsymbol{e}}_x + n_y\hat{\boldsymbol{e}}_y$, where n_x and n_y are the direction cosines of the unit normal.

In what follows, the equation of motion for the classical plate model will be derive taking two approaches. The first one will be based on the variational methods, explained in the previous chapter. The second one will be to derive the equations of motion by a direct inspection of the moments and forces acting on a infinitesimal portion of the plate. Then, the equation of motion in therms of the z-direction

displacement, w, is obtained.

Derivation by variational principles

The Hamilton's principle will be applied to find the equation of motion in the interior if the plate. Following (3.8) and (3.9), the virtual strain components are given by

$$\delta\varepsilon_{xx} = -z\frac{\partial^2 \delta w}{\partial x^2}, \quad \delta\varepsilon_{yy} = -z\frac{\partial^2 \delta w}{\partial y^2}, \quad \delta\varepsilon_{xy} = -z\frac{\partial^2 \delta w}{\partial x \partial y}, \tag{3.10}$$

and

$$\delta\varepsilon_{xz} = \delta\varepsilon_{yz} = \delta\varepsilon_{zz} = 0. \tag{3.11}$$

Thus, the internal virtual work done (or virtual strain energy) is given by

$$\delta W_I = \delta U = \int_\Omega \int_{-h/2}^{h/2} \sigma_{ij}\delta\varepsilon_{ij} dv = \int_\Omega \int_{-h/2}^{h/2} (\sigma_{xx}\delta\varepsilon_{xx} + \sigma_{yy}\delta\varepsilon_{yy} + 2\sigma_{xy}\delta\varepsilon_{xy}) dz dx dy. \tag{3.12}$$

By introducing the *bending moments*, also known as *stress resultants*, given by

$$M_{xx} = \int_{-h/2}^{h/2} \sigma_{xx} z dz,\ M_{yy} = \int_{-h/2}^{h/2} \sigma_{yy} z dz,\ M_{xy} = \int_{-h/2}^{h/2} \sigma_{xy} z dz, \tag{3.13}$$

the internal virtual work, in terms of the z-direction virtual displacement, takes the form

$$\delta W_I = \int_\Omega \left(-M_{xx}\frac{\partial^2 \delta w}{\partial x^2} - M_{yy}\frac{\partial^2 \delta w}{\partial y^2} - 2M_{xy}\frac{\partial^2 \delta w}{\partial x \partial y} \right) dx dy. \tag{3.14}$$

The traverse external body force, $q(x, y)$, will be consider to be composed of two distributed traverse loads, one, $q_t(x, y)$, applied at the top surface, $(z = h/2)$, and the second one, $q_b(x, y)$ applied at the bottom surface, $(z = -h/2)$, as

$$q(x, y) = q_t(x, y) + q_b(x, y). \tag{3.15}$$

By considering that the forces and moments acting on the portion Γ_σ of the edge with normal $\hat{\mathbf{n}}$, are due to in-plane normal stress $\hat{\sigma}_{nn}$, in-plane tangential stress $\hat{\sigma}_{ns}$, and the transverse shear stress $\hat{\sigma}_{nz}$, and that the virtual displacement on the edge is given by

$$\delta\mathbf{u}|_{\Gamma_\sigma} = (-z\frac{\partial \delta w}{\partial n}, -z\frac{\partial \delta w}{\partial s}, \delta w), \tag{3.16}$$

where n and s denote the normal and tangential direction (on the edge) respectively, the virtual work done by external forces takes the form

$$
\begin{aligned}
\delta W_E &= -\Bigg(\int_\Omega (q_t(x,y)\delta w(x,y,h/2) + q_b(x,y)\delta w(x,y,-h/2))\, dxdy \\
&\quad + \int_{\Gamma_\sigma} \int_{-h/2}^{h/2} (\hat{\sigma}_{nn}, \hat{\sigma}_{ns}, \hat{\sigma}_{nz}) \cdot \delta \mathbf{u}|_{\Gamma_\sigma}\, dzds \Bigg) \\
&= -\Bigg(\int_\Omega (q_t(x,y) + q_b(x,y))\delta w\, dxdy \\
&\quad + \int_{\Gamma_\sigma} \int_{-h/2}^{h/2} (\hat{\sigma}_{nn}(-z\frac{\partial \delta w}{\partial n}) + \hat{\sigma}_{ns}(-z\frac{\partial \delta w}{\partial s}) + \hat{\sigma}_{nz}\delta w)\, dzds \Bigg) \\
&= -\Bigg(\int_\Omega q(x,y)\delta w\, dxdy \\
&\quad + \int_{\Gamma_\sigma} (-\hat{M}_{nn}\frac{\partial \delta w}{\partial n} - \hat{M}_{ns}\frac{\partial \delta w}{\partial s} + \hat{Q}_n \delta w)\, ds \Bigg),
\end{aligned}
\tag{3.17}
$$

where

$$
\hat{M}_{nn} = \int_{-h/2}^{h/2} \sigma_{nn} z dz, \quad \hat{M}_{ns} = \int_{-h/2}^{h/2} \sigma_{ns} z dz, \quad \hat{Q}_n = \int_{-h/2}^{h/2} \sigma_{nz} dz. \tag{3.18}
$$

Finally, the virtual kinetic energy is given by

$$
\begin{aligned}
\delta K &= \frac{1}{2}\delta \int_V \rho(\dot{\mathbf{u}} \cdot \dot{\mathbf{u}}) dzdxdy = \int_\Omega \int_{-h/2}^{h/2} \rho(\dot{\mathbf{u}} \cdot \delta\dot{\mathbf{u}}) dzdxdy \\
&= \int_\Omega \int_{-h/2}^{h/2} \rho \left[(-z\frac{\partial \dot{w}}{\partial x})(-z\frac{\partial \delta\dot{w}}{\partial x}) + (-z\frac{\partial \dot{w}}{\partial y})(-z\frac{\partial \delta\dot{w}}{\partial y}) + \dot{w}\delta\dot{w} \right] dzdxdy \\
&= \int_\Omega \left[I_0(\dot{w}\delta\dot{w}) + I_2 \left(\frac{\partial \dot{w}}{\partial x}\frac{\partial \delta\dot{w}}{\partial x} + \frac{\partial \dot{w}}{\partial y}\frac{\partial \delta\dot{w}}{\partial y} \right) \right] dxdy,
\end{aligned}
\tag{3.19}
$$

where

$$
I_0 = \int_{-h/2}^{h/2} \rho dz = \rho h, \quad I_2 = \int_{-h/2}^{h/2} z^2 \rho dz = \rho \frac{h^3}{12}, \tag{3.20}
$$

are known as the *mass moments of inertia.* For time-dependent problems, the admissible virtual displacements must vanish at time $t_1 = 0$ and $t_2 = T$. Substituting

δW_I, δW_E and δK in the Hamilton's principle (2.75), yields

$$\begin{aligned} 0 = \int_0^T \Bigg\{ \int_\Omega \Bigg[& I_0(\dot{w}\delta\dot{w}) + I_2 \left(\frac{\partial \dot{w}}{\partial x}\frac{\partial \delta\dot{w}}{\partial x} + \frac{\partial \dot{w}}{\partial y}\frac{\partial \delta\dot{w}}{\partial y} \right) \\ & - \left(-M_{xx}\frac{\partial^2 \delta w}{\partial x^2} - M_{yy}\frac{\partial^2 \delta w}{\partial y^2} - 2M_{xy}\frac{\partial^2 \delta w}{\partial x \partial y} \right) + q\delta w \Bigg] \Bigg\} dt \\ & + \int_0^T \left\{ \int_{\Gamma_\sigma} \left(-\hat{M}_{nn}\frac{\partial \delta w}{\partial n} - \hat{M}_{ns}\frac{\partial \delta w}{\partial s} + \hat{Q}_n \delta w \right) ds \right\} dt. \end{aligned} \tag{3.21}$$

In order to apply the fundamental lemma of variational calculus (defined in appendix A) the virtual displacements have to be relieved of any differentiation in the first integral of (3.21). This can be done by integrating by parts in time and space. Like this, the partial derivatives of the virtual displacements pass to their respective coefficients, the sign of the integral in the interior is inverted (for every differentiation), and the corresponding boundary conditions are added. The boundary conditions in time at $t = 0$ and $t = T$ are set to zero because the virtual displacements are zero at $t = 0$ and $t = T$. The boundary conditions in space are given in terms of the normal-direction partial derivatives and the components of the outward normal vector, $\hat{\mathbf{n}} = n_x\hat{\boldsymbol{e}}_x + n_y\hat{\boldsymbol{e}}_y$. Therefore, the Hamilton's principle takes the form

$$\begin{aligned} 0 = \int_0^T \Bigg\{ \int_\Omega \Bigg[& -I_0(\ddot{w}\delta w) + I_2 \left(\frac{\partial^2 \ddot{w}}{\partial x^2} + \frac{\partial^2 \ddot{w}}{\partial y^2} \right) \delta w \\ & + \left(M_{xx,xx} + M_{yy,yy} + 2M_{xy,xy} \right) \delta w + q\delta w \Bigg] dxdy \\ & + \int_\Gamma \Bigg[- M_{xx}n_x\frac{\partial \delta w}{\partial x} + M_{xx,x}n_x\delta w - M_{yy}n_y\frac{\partial \delta w}{\partial y} + M_{yy,y}n_y\delta w \\ & - M_{xy}n_x\frac{\partial \delta w}{\partial y} + M_{xy,x}n_y\delta w - M_{xy}n_y\frac{\partial \delta w}{\partial x} + M_{xy,y}n_x\delta w \\ & + I_2 \left(\frac{\partial \ddot{w}}{\partial x}n_x + \frac{\partial \ddot{w}}{\partial y}n_y \right) \delta w \Bigg] ds \Bigg\} dt \\ & + \int_0^T \left\{ \int_{\Gamma_\sigma} \left(-\hat{M}_{nn}\frac{\partial \delta w}{\partial n} - \hat{M}_{ns}\frac{\partial \delta w}{\partial s} + \hat{Q}_n \delta w \right) ds \right\} dt, \end{aligned} \tag{3.22}$$

where the indexes after a coma represent a partial derivative with respect to the index variable, e.g. $M_{xy,xy} = \partial^2 M_{xy}/\partial x \partial y$. In order to obtain the equations of motion in the interior of the plate, the integral over Ω can be treated separately to satisfy the Hamilton's principle. The integral on the edges Γ and Γ_σ has to be analyse following the Euler-Lagrange equations (as explained in appendix A) in order to obtain the boundary conditions, but this will be done for an specific case in the next section. Thus, by considering only the integral over Ω, and grouping the terms that has δw

as a factor the Hamilton's principle takes the form

$$\begin{aligned} 0 = -\int_0^T \Bigg\{ \int_\Omega \Bigg[\Bigg(-I_0 \ddot{w} + I_2 \left(\frac{\partial^2 \ddot{w}}{\partial x^2} + \frac{\partial^2 \ddot{w}}{\partial y^2} \right) \\ + (M_{xx,xx} + M_{yy,yy} + 2M_{xy,xy}) + q \Bigg) \delta w \Bigg] dxdy \Bigg\} dt \end{aligned} \tag{3.23}$$

As the integral has to be zero for any δw, the term multiplying δw in the integral has to be identically zero, leading to the following equation of motion

$$M_{xx,xx} + M_{yy,yy} + 2M_{xy,xy} + q = I_0 \ddot{w} - I_2 \left(\frac{\partial^2 \ddot{w}}{\partial x^2} + \frac{\partial^2 \ddot{w}}{\partial y^2} \right) \tag{3.24}$$

The terms involving I_2 are called rotary (or rotatory) inertia terms, and are often neglected in most books. The term can contribute to higher frequencies of vibration. For the case we are interested in, the fundamental frequencies are of the order of the hundred of thousand of Hertz to the mega Hertz, thus, the higher order frequencies are not of interest. Therefore, the equation of motion for the classical plate theory that will be consider for our model is given by

$$\frac{\partial^2 M_{xx}}{\partial x^2} + \frac{\partial^2 M_{yy}}{\partial y^2} + 2\frac{\partial^2 M_{xy}}{\partial x \partial y} + q = \rho h \frac{\partial^2 w}{\partial t^2}. \tag{3.25}$$

Derivation by balance of forces and moments

As a consequence of nullifying the in-plane displacement, as explained in the equation (3.6), the in-plane tension forces, or *membrane forces*, are neglected. Thus, the only remaining internal forces acting on the plate are the bending and twisting moments, and the shear forces. In figure 3.1 a infinitesimal element of a plate with in-plane dimensions $dx \times dy$ and thickness h with the mid-plane placed in the (x, y) plane is drawn. Shown on the element, by vectors with single arrows, are transverse shearing forces (per unit length along an edge) Q_x and Q_y, and their incremental changes, acting along its edges, and a distributed loading (per unit surface area) q which is applied on the plate's surface. Also, the bending moment resultants (M_{xx} and M_{yy}) are shown by vectors with double arrows, as well as the twisting moment resultants (M_{xy} and M_{yx}), and their incremental changes. All of which have dimensions of moment per unit length along an edge.

The bending moments are defined in (3.13), and the shear forces per unit length along an edge are defined as

$$Q_x = \int_{-h/2}^{h/2} \sigma_{xz} dz, \quad Q_y = \int_{-h/2}^{h/2} \sigma_{yz} dz. \tag{3.26}$$

The equation of motion can be found by obtaining the relation between the bending moments and the shear forces. This can be done by considering the Cauchy's equation

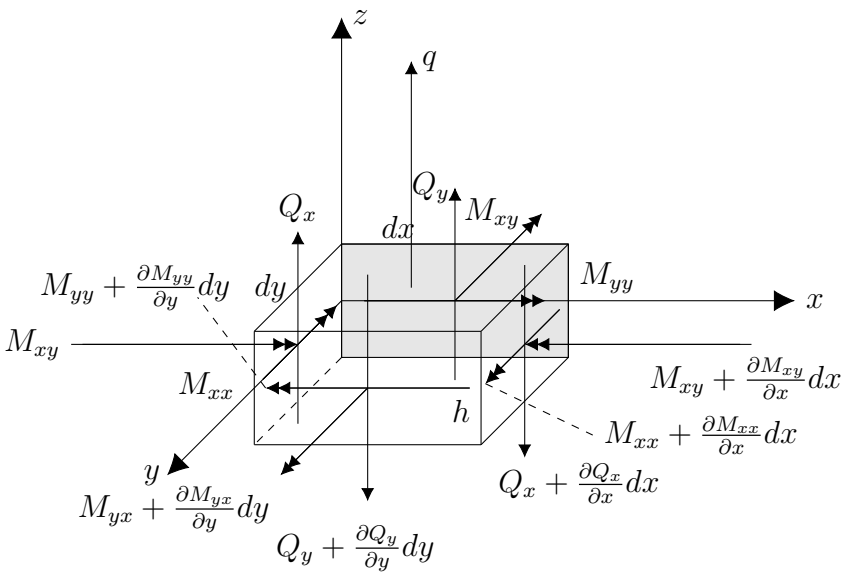

Figure 3.1: Shear forces, bending and twisting moments acting on a $dx \times dy \times h$ infinitesimal plate section.

of motion (2.15), given by components as

$$\begin{aligned} \frac{\partial \sigma_{xx}}{\partial x} + \frac{\partial \sigma_{xy}}{\partial y} + \frac{\partial \sigma_{xz}}{\partial z} &= \rho \frac{\partial^2 u}{\partial t^2}, \\ \frac{\partial \sigma_{xy}}{\partial x} + \frac{\partial \sigma_{yy}}{\partial y} + \frac{\partial \sigma_{yz}}{\partial z} &= \rho \frac{\partial^2 v}{\partial t^2}, \\ \frac{\partial \sigma_{xz}}{\partial x} + \frac{\partial \sigma_{yz}}{\partial y} + \frac{\partial \sigma_{zz}}{\partial z} &= \rho \frac{\partial^2 w}{\partial t^2}. \end{aligned} \tag{3.27}$$

Additionally, the external force, $q(x, y) = q_b(x, y) + q_t(x, y)$, can be introduced by considering the stress boundary conditions on the top and bottom surfaces of the infinitesimal plate element to be given by

$$\begin{aligned} \sigma_{xz}(x, y, -\frac{h}{2}) = 0,\ \sigma_{xz}(x, y, \frac{h}{2}) = 0,\ \sigma_{yz}(x, y, -\frac{h}{2}) = 0, \\ \sigma_{yz}(x, y, \frac{h}{2}) = 0,\ \sigma_{zz}(x, y, -\frac{h}{2}) = -q_b,\ \sigma_{zz}(x, y, \frac{h}{2}) = q_t. \end{aligned} \tag{3.28}$$

By taking the z-direction component in (3.27), and integrating with respect to z

over the interval $(-h/2, h/2)$, yields

$$\begin{aligned}
&\frac{\partial}{\partial x}\int_{-h/2}^{h/2}\sigma_{xz}dz + \frac{\partial}{\partial y}\int_{-h/2}^{h/2}\sigma_{yz}dz + \int_{-h/2}^{h/2}\frac{\partial\sigma_{zz}}{\partial z}dz = \rho\frac{\partial^2 w}{\partial t^2}\int_{-h/2}^{h/2}dz,\\
&\quad\Rightarrow \frac{\partial Q_x}{\partial x} + \frac{\partial Q_y}{\partial y} + (\sigma_{zz}(x,y,\frac{h}{2}) - \sigma_{zz}(x,y,-\frac{h}{2})) = \rho h\frac{\partial^2 w}{\partial t^2},\\
&\quad\Rightarrow \frac{\partial Q_x}{\partial x} + \frac{\partial Q_y}{\partial y} + (q_t + q_b) = \rho h\frac{\partial^2 w}{\partial t^2},\\
&\quad\Rightarrow \frac{\partial Q_x}{\partial x} + \frac{\partial Q_y}{\partial y} + q = \rho h\frac{\partial^2 w}{\partial t^2},
\end{aligned} \tag{3.29}$$

which is equivalent to consider the balance of forces acting on the z-direction, from the diagram in figure (3.1). By taking the equations involving u and v in (3.27), and replacing them in terms of $w(x,y)$ using (3.7), multiplying with z and integrating again with respect to z over the interval $(-h/2, h/2)$, leads to

$$\begin{aligned}
&\frac{\partial}{\partial x}\int_{-h/2}^{h/2}z\sigma_{xx}dz + \frac{\partial}{\partial y}\int_{-h/2}^{h/2}z\sigma_{xy}dz + \int_{-h/2}^{h/2}z\frac{\partial\sigma_{xz}}{\partial z}dz = \rho\int_{-h/2}^{h/2}-z^2\frac{\partial\ddot{w}}{\partial x}dz,\\
&\quad\Rightarrow \frac{\partial M_{xx}}{\partial x} + \frac{\partial M_{xy}}{\partial y} - Q_x = -I_2\frac{\partial\ddot{w}}{\partial x},\\
&\quad\Rightarrow Q_x = I_2\frac{\partial\ddot{w}}{\partial x} + \left(\frac{\partial M_{xx}}{\partial x} + \frac{\partial M_{xy}}{\partial y}\right),
\end{aligned} \tag{3.30}$$

and

$$\begin{aligned}
&\frac{\partial}{\partial x}\int_{-h/2}^{h/2}z\sigma_{yx}dz + \frac{\partial}{\partial y}\int_{-h/2}^{h/2}z\sigma_{yy}dz + \int_{-h/2}^{h/2}z\frac{\partial\sigma_{yz}}{\partial z}dz = \rho\int_{-h/2}^{h/2}-z^2\frac{\partial\ddot{w}}{\partial y}dz,\\
&\quad\Rightarrow \frac{\partial M_{xy}}{\partial x} + \frac{\partial M_{yy}}{\partial y} - Q_y = -I_2\frac{\partial\ddot{w}}{\partial y},\\
&\quad\Rightarrow Q_y = I_2\frac{\partial\ddot{w}}{\partial y} + \left(\frac{\partial M_{xy}}{\partial x} + \frac{\partial M_{yy}}{\partial y}\right),
\end{aligned} \tag{3.31}$$

where the integration by parts was used and the zero stress boundary conditions in (3.28) were applied, to compute

$$\int_{-h/2}^{h/2}z\frac{\partial\sigma_{xz}}{\partial z}dz = z\sigma_{xz}\big|_{-h/2}^{h/2} - \int_{-h/2}^{h/2}\sigma_{xz}dz = -\int_{-h/2}^{h/2}\sigma_{xz}dz = -Q_x, \tag{3.32}$$

and

$$\int_{-h/2}^{h/2}z\frac{\partial\sigma_{yz}}{\partial z}dz = z\sigma_{yz}\big|_{-h/2}^{h/2} - \int_{-h/2}^{h/2}\sigma_{yz}dz = -\int_{-h/2}^{h/2}\sigma_{yz}dz = -Q_y, \tag{3.33}$$

Finally, by replacing Q_x and Q_y from (3.30) and (3.31) in (3.29), yields

$$\frac{\partial}{\partial x}\left[I_2\frac{\partial \ddot{w}}{\partial x}+\left(\frac{\partial M_{xx}}{\partial x}+\frac{\partial M_{xy}}{\partial y}\right)\right]+\frac{\partial}{\partial y}\left[I_2\frac{\partial \ddot{w}}{\partial y}+\left(\frac{\partial M_{xy}}{\partial x}+\frac{\partial M_{yy}}{\partial y}\right)\right]+q=\rho h\frac{\partial^2 w}{\partial t^2}$$

$$\Rightarrow \frac{\partial^2 M_{xx}}{\partial x^2}+\frac{\partial^2 M_{yy}}{\partial y^2}+2\frac{\partial^2 M_{xy}}{\partial x\partial y}+q=\rho h\frac{\partial^2 w}{\partial t^2}-I_2\left(\frac{\partial^2 \ddot{w}}{\partial x^2}+\frac{\partial^2 \ddot{w}}{\partial y^2}\right). \tag{3.34}$$

By again neglecting the rotatory inertia terms, leads to

$$\frac{\partial^2 M_{xx}}{\partial x^2}+\frac{\partial^2 M_{yy}}{\partial y^2}+2\frac{\partial^2 M_{xy}}{\partial x\partial y}+q=\rho h\frac{\partial^2 w}{\partial t^2}, \tag{3.35}$$

which is the same equation of motion found in (3.25).

Equation of motion in terms of the displacement

The previous derivations from the Kirschhoff hypothesis imply that the traverse strains $(\varepsilon_{xz}, \varepsilon_{yz}, \varepsilon_{zz})$ are identically zero. For the classical plate theory, a isotropic material constitutive relation, given by

$$\sigma_{ij}=\lambda\delta_{ij}\varepsilon_{kk}+2\mu\varepsilon_{ij}, \tag{3.36}$$

is considered. Consequently,

$$\sigma_{xz}=2\mu\varepsilon_{xz}=0,$$

and

$$\sigma_{yz}=2\mu\varepsilon_{yz}=0.$$

Even when the traverse stress, σ_{zz}, is not exactly zero, it does not enter into the formulation of the equation of motion as it does not account for the internal virtual strain energy of the plate (see equation (2.55)). Then, for the case of the classical plate theory, is assumed a plane stress state to model the constitutive equations in the interior of Ω. Regardless of whether a theory accounts for transverse stresses or not, in reality, these stresses exist to maintain equilibrium in a plate. While the virtual strain energy expression does not include the transverse stresses, they must still be considered in the boundary conditions and the equilibrium of forces. Therefore, in order to obtain the equation of motion in the interior of the plate, in terms of the z-displacement component, $w(x, y)$, the constitutive relations of a plane stress state, given by

$$\begin{bmatrix}\sigma_{xx}\\ \sigma_{yy}\\ \sigma_{xy}\end{bmatrix}=\frac{E}{1-\nu^2}\begin{bmatrix}1 & \nu & 0\\ \nu & 1 & 0\\ 0 & 0 & \frac{1-\nu}{2}\end{bmatrix}\begin{bmatrix}\varepsilon_{xx}\\ \varepsilon_{yy}\\ \gamma_{xy}\end{bmatrix}, \tag{3.37}$$

will be consider. By substituting the strain tensor components, given by (3.8), the

stress tensor components are given by

$$\begin{aligned}
\sigma_{xx} &= \frac{E}{1-\nu^2}(\varepsilon_{xx}+\nu\varepsilon_{yy}) = -z\frac{E}{1-\nu^2}\left(\frac{\partial^2 w}{\partial x^2}+\nu\frac{\partial^2 w}{\partial y^2}\right),\\
\sigma_{yy} &= \frac{E}{1-\nu^2}(\nu\varepsilon_{xx}+\varepsilon_{yy}) = -z\frac{E}{1-\nu^2}\left(\nu\frac{\partial^2 w}{\partial x^2}+\frac{\partial^2 w}{\partial y^2}\right),\\
\sigma_{xy} &= \frac{E}{2(1-\nu^2)}(1-\nu)\gamma xy = -z\frac{E}{1-\nu^2}(1-\nu)\frac{\partial^2 w}{\partial x\partial y}.
\end{aligned} \tag{3.38}$$

Thus, the bending moments, in terms of $w(x,y)$, are given by

$$\begin{aligned}
M_{xx} &= \int_{h/2}^{h/2} z\sigma_{xx}dz = -\int_{h/2}^{h/2} z^2\frac{E}{1-\nu^2}(\frac{\partial^2 w}{\partial x^2}+\nu\frac{\partial^2 w}{\partial y^2})dz = -D\left(\frac{\partial^2 w}{\partial x^2}+\nu\frac{\partial^2 w}{\partial y^2}\right),\\
M_{yy} &= \int_{h/2}^{h/2} z\sigma_{yy}dz = -\int_{h/2}^{h/2} z^2\frac{E}{1-\nu^2}(\nu\frac{\partial^2 w}{\partial x^2}+\frac{\partial^2 w}{\partial y^2})dz = -D\left(\nu\frac{\partial^2 w}{\partial x^2}+\frac{\partial^2 w}{\partial y^2}\right),\\
M_{xy} &= \int_{h/2}^{h/2} z\sigma_{xy}dz = -\int_{h/2}^{h/2} z^2\frac{E}{1-\nu^2}(1-\nu)\frac{\partial^2 w}{\partial x\partial y}dz = -D(1-\nu)\frac{\partial^2 w}{\partial x\partial y},
\end{aligned} \tag{3.39}$$

where

$$D = \frac{Eh^3}{12(1-\nu^2)} \tag{3.40}$$

is the so-called *flexural rigidity* of the plate, with E being the Young's modulus and ν the Poisson's ratio.

Finally, by substituting the bending moments (3.39) in the equation of motion (3.25), the equation of motion for a Kirchhoff-Kelvin thin plate of thickness h and volumetric density ρ, in terms of the deflection of the mid-plane, $w(x,y)$, takes the form

$$-D\nabla^4 w = -D\left(\frac{\partial^4 w}{\partial y^4}+2\frac{\partial^4 w}{\partial y^2\partial x^2}+\frac{\partial^4 w}{\partial x^4}\right)+q = \rho h\frac{\partial^2 w}{\partial t^2}, \tag{3.41}$$

where

$$\nabla^4 := \left(\frac{\partial^4}{\partial y^4}+2\frac{\partial^4}{\partial y^2\partial x^2}+\frac{\partial^4}{\partial x^4}\right), \tag{3.42}$$

is known as the *biharmonic* operator.

3.2.3 Clamped boundary conditions

The real polymer microscopic plate for which the mathematical model is been developed, is build in such a way that the edge is completely fixed. Thus, the plate model that will be used has clamped (or fixed) boundary conditions. The clamped boundary conditions are one where the movement of the plate is geometrically fully

restrained, hence

$$w = \frac{\partial w}{\partial \mathbf{n}} = 0, \tag{3.43}$$

where $\mathbf{n}$ is the outer normal vector on the plate edge surface Γ.

Given that the actual displacements and their normal derivatives are defined, the corresponding virtual displacements are zero. Consequently, the integrals over Γ_σ and Γ in equation (3.22) becomes zero as well. Therefore, the Hamilton's principle is trivially satisfied. It is important to note that in order to obtain other boundary conditions, the Euler-Lagrange equations need to be specified for this boundary term. For additional information on different types of boundary conditions, refer to [Reddy, 2006].

3.2.4 Circular clamped plates

In order to solve the equation of motion of a circular plate clamped at the border and free in the centre, we begin by assuming a solution that has a sinusoidal response in time, given by

$$w(x, y, t) = W(x, y) \sin(\omega t + \phi). \tag{3.44}$$

By substituting this solution in (3.41), the spatial term of the equation becomes

$$(\nabla^4 - k^4)W = 0 \tag{3.45}$$

where

$$k^4 = \rho h \omega^2 / D. \tag{3.46}$$

The differential operator $(\nabla^4 - k^4)$ may be factorised as the composition

$$(\nabla^2 + k^2) \circ (\nabla^2 - k^2),$$

thus, the solution to (3.45) is the sum of the solutions arising from its two parts,

$$(\nabla^2 + k^2)W = 0 \tag{3.47}$$

$$(\nabla^2 - k^2)W = 0 \tag{3.48}$$

In polar coordinates the spatial part of the solution is $W \equiv W(r, \theta)$, and the laplacian operator is given by

$$\nabla^2 = \frac{\partial^2}{\partial r^2} + \frac{1}{r}\frac{\partial}{\partial r} + \frac{1}{r^2}\frac{\partial^2}{\partial \theta^2} \tag{3.49}$$

Expecting a solution given by normal modes, we can assume that

$$W = W_n(r) \cos(n\theta), \tag{3.50}$$

not only because it satisfies (3.47) and (3.48), but the integer values of n give the

desired *periodicity* needed for the solution, that is

$$W(r,\theta) = W(r,\theta+2\pi),$$

notice that $\sin(n\theta)$ also satisfies the periodicity, but it misses the first axisymmetric mode with $n=0$.

Substituting in (3.47) and (3.48) yields

$$\frac{d^2W_n}{dr^2} + \frac{1}{r}\frac{dW_n}{dr} - \Big(\frac{n^2}{r^2} - k^2\Big)W_n = 0, \tag{3.51}$$

$$\frac{d^2W_n}{dr^2} + \frac{1}{r}\frac{dW_n}{dr} - \Big(\frac{n^2}{r^2} + k^2\Big)W_n = 0. \tag{3.52}$$

The solution for (3.51) are the ordinary Bessel functions of first and second kind with real argument kr. The solution of (3.52) can be expressed as the *modified* Bessel functions with the same argument. Thus, the complete solution is obtained as the sum, this is

$$W = [A_nJ_n(kr) + B_nY_n(kr) + C_nI_n(kr) + D_nK_n(kr)]\cos(n\theta)$$

As $Y_n(0) = -\infty$ and $K_n(0) = \infty$, for a circular plate centred in the origin $B_n = D_n = 0$, therefore

$$W = [A_nJ_n(kr) + C_nI_n(kr)]\cos(n\theta). \tag{3.53}$$

Supposing a clamped boundary at $r=a$ the boundary conditions are

$$w(a,\theta,t) = 0, \quad \frac{\partial w}{\partial r}(a,\theta,t) = 0,$$

whence

$$W_n(a) = 0 \quad \text{and} \quad W_n'(a) = 0. \tag{3.54}$$

Substituting (3.53) into (3.54) gives

$$\begin{pmatrix} J_n(\lambda) & I_n(\lambda) \\ J_n'(\lambda) & I_n'(\lambda) \end{pmatrix}\begin{pmatrix} A_n \\ C_n \end{pmatrix} = \begin{pmatrix} 0 \\ 0 \end{pmatrix} \tag{3.55}$$

where $\lambda^2 = (ka)^2 = \omega a^2\sqrt{\rho h/D}$ form the definition of k in (3.46). Using the relationships

$$\lambda J_n'(\lambda) = nJ_n(\lambda) - \lambda J_{n+1}(\lambda)$$
$$\lambda I_n'(\lambda) = nI_n(\lambda) - \lambda I_{n+1}(\lambda)$$

and setting the determinant of the matrix (3.55) to be zero (in order to have a nontrivial solutions), we obtain that the values of λ have to satisfy

$$J_n(\lambda)I_{n+1}(\lambda) + I_n(\lambda)J_{n+1}(\lambda) = 0. \tag{3.56}$$

	s			
n	0	1	2	3
0	10.22	39.77	89.10	158.18
1	21.26	60.82	120.1	199.1
2	34.88	84.58	153.8	242.7
3	51.04	111.0	190.3	289.2
4	69.67	140.1	229.5	338.4
5	90.74	171.8	271.4	390.4

Table 3.1: Non dimensional frequencies $\omega a^2\sqrt{\rho h/D}$ for a clamped circular plate. Values taken from [Leissa and Qatu, 2011], table 6.2.

The ratio C_n/A_n can be found with the first equation in (3.55), as

$$\begin{aligned} A_n J_n(\lambda) + C_n I_n(\lambda) &= 0 \\ \Rightarrow A_n J_n(\lambda) &= -C_n I_n(\lambda) \\ \Rightarrow \frac{C_n}{A_n} &= -\frac{J_n(\lambda)}{I_n(\lambda)}. \end{aligned} \tag{3.57}$$

Dividing (3.53) by A_n and substituting (3.57), we found the eigen functions describing the modes shapes as

$$W_{mn}(r,\theta) = \left[J_n\Big(\lambda_{mn}\frac{r}{a}\Big) - \frac{J_n(\lambda_{mn})}{I_n(\lambda_{mn})} I_n\Big(\lambda_{mn}\frac{r}{a}\Big)\right]\cos n\theta, \tag{3.58}$$

where λ_{mn} represents the mth eigenvalue from (3.56) for a given n. The roots λ of (3.56) have to be obtained numerically or consulted in tables. Values of the non dimensional frequency,

$$\lambda^2 = \omega a^2\sqrt{\rho h/D}, \tag{3.59}$$

for modes having n nodal diameters and s interior nodal circles are presented in figure 3.1.

3.3 Equation of motion for the loaded plate with damping

In this section, the system to be analysed will be introduced. The mathematical model to approximate said system consists of a loaded plate with damping. Such a model will be derived by parting from the classical plate theory, modifying it to approximate the desired system.

In the first section of this chapter, two different ways to arrive to the same equation of motion in the interior of a isotropic plate, following the Kirchhoff hypothesis with the addition of neglecting the horizontal displacements, have been given. The first used the internal and external energies present in the plate, to arrive to a equation

that govern the deflection of the interior of the mid-plane Ω, applying the Hamilton's principle. The second one, analyse the forces and moments acting *only* on a infinitesimal element of the plate. This later conceptual formulation will be important to develop the model of a non-homogeneous plate that was implemented in this work, as it express the equation of motion as a local behaviour, depending on the local material and geometric properties of the plate.

3.3.1 Loaded plate model

The system to be modelled, consists of a clamped circular polymer material plate, of radius R_{ext} and thickness h_1, with a concentric circular metallic load on the top surface, of radius R_{int} and thickness h_2, as show in figure 3.2. In what follows,two models that approximates the loaded plate system will be explained and derived. The first one presents both computational and conceptual complexities that makes it hard to be implemented for the desired system. The aim of explaining this model, is to illustrate the process to derive the second model, and to explain some cases where it could be used. The second model, consists in a further simplification of the first one, but is consistent both computationally and conceptually according to the theory of plates. The second model is the one that will be implemented computationally to obtain results.

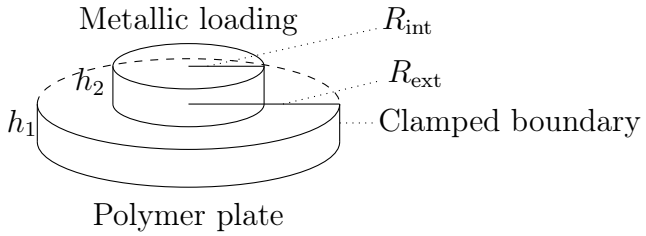

Figure 3.2: Clamped circular polymer material plate with a concentric circular metallic load on the top surface.

Distributed-parameters model

In both cases, a two dimensional approximation to the loaded plate system, will be given in terms of the material, elastic and geometric properties of the materials involved. This consists in taking a two dimensional circular plate, and making its Young's modulus E, Poisson's ratio ν, thickness h and density ρ to depend on the spatial coordinates, this is

$$E \equiv E(x,y) \quad \nu \equiv \nu(x,y) \quad \rho \equiv \rho(x,y) \quad h \equiv h(x,y).$$

These modifications lead to spatial-dependent flexural rigidity D give by

$$D(x,y) = \frac{E(x,y)h^3(x,y)}{12(1-\nu(x,y)^2)}. \tag{3.60}$$

For the portion of the plate where there is a material on top of another, for instance, the material 2 occupying a region of thickness h_2 on top of a circular plate of thickness h_1 compose of the material 1, an *effective Young's modulus*, E_T, will be consider, obtained from the following formulae

$$\frac{h_T}{E_T} = \frac{h_2}{E_2} + \frac{h_1}{E_1} \Rightarrow E_T = \frac{h_T}{\frac{h_2}{E_2} + \frac{h_1}{E_1}},$$

where $h_T = h_2 + h_1$ is the total thickness of the loaded region. Similarly, we can find the effective density, ρ_T, of this region, as

$$\rho_T = \frac{h_T}{\frac{h_2}{\rho_2} + \frac{h_1}{\rho_1}},$$

as well as an effective Poisson's ratio

$$\nu_T = \frac{h_T}{\frac{h_2}{\nu_2} + \frac{h_1}{\nu_1}}.$$

Variable coefficients model

In the classical plate model, the equation of motion is given in terms of the deflection of the mid-plane $w(x, y)$. Thus, in order to make use of this theory, the system to be analyse have to be symmetric in the traverse direction, so that the mid-plane can be properly defined. Therefore, a further simplification will be made on the original system, which consists in making that the loaded part to share the same mid-plane symmetry as the unloaded part of the plate. This can be done by placing the load whit half of its thickness in the top and bottom surfaces of the plate, as shown in figure 3.3.

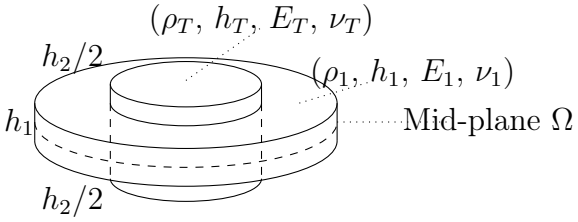

Figure 3.3: Symmetric loaded plate.

The first model, modifies the equation of motion by modifying the bending mo-

ments with the variable coefficients, which leads to

$$
\begin{aligned}
M_{xx} &= -\int_{-h(x,y)/2}^{h(x,y)/2} z^2 \frac{E(x,y)}{1-\nu(x,y)^2}\left(\frac{\partial^2 w}{\partial x^2}+\nu(x,y)\frac{\partial^2 w}{\partial y^2}\right)dz = -D(x,y)\left(\frac{\partial^2 w}{\partial x^2}+\nu(x,y)\frac{\partial^2 w}{\partial y^2}\right),\\
M_{yy} &= -\int_{-h(x,y)/2}^{h(x,y)/2} z^2 \frac{E(x,y)}{1-\nu(x,y)^2}\left(\nu(x,y)\frac{\partial^2 w}{\partial x^2}+\frac{\partial^2 w}{\partial y^2}\right)dz = -D(x,y)\left(\nu(x,y)\frac{\partial^2 w}{\partial x^2}+\frac{\partial^2 w}{\partial y^2}\right),\\
M_{xy} &= -\int_{-h(x,y)/2}^{h(x,y)/2} z^2 \frac{E(x,y)}{1-\nu(x,y)^2}(1-\nu(x,y))\frac{\partial^2 w}{\partial x\partial y}dz = -D(x,y)(1-\nu(x,y))\frac{\partial^2 w}{\partial x\partial y},
\end{aligned}
\tag{3.61}
$$

where the spatial dependency of the thickness h can be represented in polar coordinates, with the origin at the centre of the plate, as a step function of the radius, as

$$
h(r) = \begin{cases} h_T, & \text{if} \quad 0 \le r < R_{\text{int}}, \\ h_1, & \text{if} \quad R_{\text{int}} \le r \le R_{\text{ext}}. \end{cases}
\tag{3.62}
$$

Then the spatial-dependant bending moments are substituted in the equation of motion (3.25) in the absence of external forces ($q = 0$), obtaining

$$
\begin{aligned}
&-2\frac{\partial D}{\partial y}\left(-\frac{\partial \nu}{\partial x}\frac{\partial^2 w}{\partial x\partial y}+\frac{\partial \nu}{\partial y}\frac{\partial^2 w}{\partial x^2}+\frac{\partial^3 w}{\partial y^3}+\frac{\partial^3 w}{\partial x^2\partial y}\right)\\
&-2\frac{\partial D}{\partial x}\left(\frac{\partial \nu}{\partial x}\frac{\partial^2 w}{\partial y^2}-\frac{\partial \nu}{\partial y}\frac{\partial^2 w}{\partial x\partial y}+\frac{\partial^3 w}{\partial x\partial y^2}+\frac{\partial^3 w}{\partial x^3}\right)\\
&+2\frac{\partial^2 D}{\partial x\partial y}\nu\frac{\partial^2 w}{\partial x\partial y}-\frac{\partial^2 D}{\partial x^2}\nu\frac{\partial^2 w}{\partial y^2}-\frac{\partial^2 D}{\partial y^2}\left(\nu\frac{\partial^2 w}{\partial x^2}+\frac{\partial^2 w}{\partial y^2}\right)\\
&-2\frac{\partial^2 D}{\partial x\partial y}\frac{\partial^2 w}{\partial x\partial y}-\frac{\partial^2 D}{\partial x^2}\frac{\partial^2 w}{\partial x^2}+2D\frac{\partial^2 \nu}{\partial x\partial y}\frac{\partial^2 w}{\partial x\partial y}-D\frac{\partial^2 \nu}{\partial x^2}\frac{\partial^2 w}{\partial y^2}-D\frac{\partial^2 \nu}{\partial y^2}\frac{\partial^2 w}{\partial x^2}\\
&\quad -D\frac{\partial^4 w}{\partial y^4}-2D\frac{\partial^4 w}{\partial x^2\partial y^2}-D\frac{\partial^4 w}{\partial x^4}=\rho(x,y)h(x,y)\Big(\frac{\partial^2 w}{\partial t^2}\Big).
\end{aligned}
\tag{3.63}
$$

In the last row of (3.63) the familiar biharmonic term can be found. The rest of the terms are all in terms of the spatial partial derivatives of $D(x,y)$ or $\nu(x,y)$. The spatial dependency of these parameters can also be represented in polar coordinates as a step function of the radius as

$$
\nu(r) = \begin{cases} \nu_T, & \text{if} \quad 0 \le r < R_{\text{int}}, \\ \nu_1, & \text{if} \quad R_{\text{int}} \le r \le R_{\text{ext}}, \end{cases}
\tag{3.64}
$$

and

$$
D(r) = \begin{cases} D_T, & \text{if} \quad 0 \le r < R_{\text{int}}, \\ D_1, & \text{if} \quad R_{\text{int}} \le r \le R_{\text{ext}}, \end{cases}
\tag{3.65}
$$

where

$$
D_1 = \frac{E_1 h_1^3}{12(1-\nu_1)}, \qquad D_T = \frac{E_T h_T^3}{12(1-\nu_T)}.
\tag{3.66}
$$

The terms of (3.63) that involve partial derivatives of D and ν can be expressed in polar coordinates, as

$$
\begin{aligned}
&-2\frac{\partial D}{\partial y}\left(-\frac{\partial \nu}{\partial x}\frac{\partial^2 w}{\partial x \partial y}+\frac{\partial \nu}{\partial y}\frac{\partial^2 w}{\partial x^2}+\frac{\partial^3 w}{\partial y^3}+\frac{\partial^3 w}{\partial x^2 \partial y}\right)\\
&-2\frac{\partial D}{\partial x}\left(\frac{\partial \nu}{\partial x}\frac{\partial^2 w}{\partial y^2}-\frac{\partial \nu}{\partial y}\frac{\partial^2 w}{\partial x \partial y}+\frac{\partial^3 w}{\partial x \partial y^2}+\frac{\partial^3 w}{\partial x^3}\right)\\
&+2\frac{\partial^2 D}{\partial x \partial y}\nu\frac{\partial^2 w}{\partial x \partial y}-\frac{\partial^2 D}{\partial x^2}\nu\frac{\partial^2 w}{\partial y^2}-\frac{\partial^2 D}{\partial y^2}\left(\nu\frac{\partial^2 w}{\partial x^2}+\frac{\partial^2 w}{\partial y^2}\right)\\
&-2\frac{\partial^2 D}{\partial x \partial y}\frac{\partial^2 w}{\partial x \partial y}-\frac{\partial^2 D}{\partial x^2}\frac{\partial^2 w}{\partial x^2}+2D\frac{\partial^2 \nu}{\partial x \partial y}\frac{\partial^2 w}{\partial x \partial y}-D\frac{\partial^2 \nu}{\partial x^2}\frac{\partial^2 w}{\partial y^2}-D\frac{\partial^2 \nu}{\partial y^2}\frac{\partial^2 w}{\partial x^2}\\
&=\frac{1}{r^3}\Bigg[r\Bigg(-\left(\left(\frac{\partial^2 w}{\partial \theta^2}+r\frac{\partial w}{\partial r}\right)\left(\nu(r)D''(r)+D(r)\nu''(r)\right)\right)-r\frac{\partial^2 w}{\partial r^2}\left(rD''(r)+D(r)\nu'(r)\right)\Bigg)\\
&-D'(r)\Bigg\{(2r\nu'(r)-3)\frac{\partial^2 w}{\partial \theta^2}+r\Bigg((2r\nu'(r)-1)\frac{\partial w}{\partial r}+r\left((\nu(r)+2)\frac{\partial^2 w}{\partial r^2}+2r\frac{\partial^3 w}{\partial r^3}\right)\\
&\qquad+2\frac{\partial^3 w}{\partial r \partial \theta^2}\Bigg)\Bigg\}\Bigg].
\end{aligned}
\tag{3.67}
$$

The main mathematical problem with this approach is that the derivative of a step function is not well defined. It can be given in terms of distributions as the Dirac Delta function, which has zero-measure in terms of Lebesgue's spaces. This could be an argument to neglect the terms involving the derivatives of $D(r)$ and $\nu(r)$, but it is not formal. This is the reason why this approach is not convenient for the loaded plate system that is being solved. This approach may be convenient when the distribution of parameters is given by differentiable functions.

Variable density model

The second approach to approximate the loaded plate system, consists in thinking on a single circular plate that has a convenient density distribution, while keeping constant the rest of the material and geometric variables, as the properties base plate h_1, E_1 and ν_1 (see figure 3.4). Said density distribution is given by

$$
\rho(r)=\begin{cases}\rho_T\frac{D_1 h_T}{D_T h_1}, & \text{if} \quad 0\leq r<R_{\text{int}},\\ \rho_1, & \text{if} \quad R_{\text{int}}\leq r\leq R_{\text{ext}}.\end{cases}
\tag{3.68}
$$

In order to derive the equation of motion for a variable density plate, consider the balance of forces of the infinitesimal plate element given in a previous section. On the right side of the Cauchy's equations of motion (2.15) the moment per unit of volume

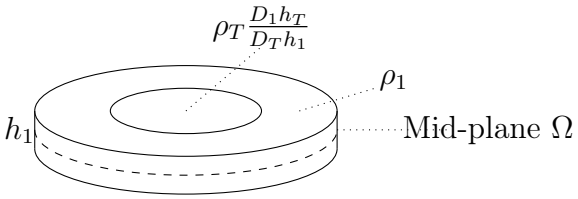

Figure 3.4: Variable density plate.

is given by

$$\rho \frac{\partial^2 \mathbf{u}}{\partial t^2}. \tag{3.69}$$

For a variable-density plate, the moment per unit of volume of a infinitesimal element of the plate will have the same space dependency as the density. In the case of a density distribution given by (3.68), the space-dependent moment per unit of volume is given by

$$\rho(r) \frac{\partial^2 \mathbf{u}}{\partial t^2}. \tag{3.70}$$

By substituting (3.70) in the Cauchy's equations of motion (3.27) the same computations can be made to derive the equation motion (3.35), only changing ρ with $\rho(r)$. Therefore, the equation of motion in terms of the z-displacement (3.41) (in the absence of external forces) is modified to be

$$-D_1 \nabla^4 w = \rho(r) h_1 \frac{\partial^2 w}{\partial t^2}. \tag{3.71}$$

To have a better understanding of the effect of the density distribution (3.68), the equation of motion (3.71) can be expressed in terms of the space-dependant *stiffness parameter*, $\kappa(r)$, given by

$$\kappa^2(r) = \frac{D_1}{\rho(r) h_1}, \tag{3.72}$$

as

$$-\kappa^2(r) \nabla^4 w = \frac{\partial^2 w}{\partial t^2}. \tag{3.73}$$

Therefore, the spatial distribution behaviour of the stiffness parameter is given by

$$\kappa^2(r) = \begin{cases} \frac{D_1}{\rho_T \frac{D_1 h_T}{D_T h_1} h_1} = \frac{D_T}{\rho_T h_T}, & \text{if} \quad 0 \leq r < R_{\text{int}}, \\ \frac{D_1}{\rho_1 h_1}, & \text{if} \quad R_{\text{int}} \leq r \leq R_{\text{ext}}. \end{cases} \tag{3.74}$$

In this way, the equation of motion (3.73) represents a two dimensional approximation to the desired loaded plate system, as it has the material properties of the unloaded and loaded sections of the plate in the adequate regions. Comment apart, this equation of motion can also be obtained by neglecting the terms that involve partial derivatives of $D(x, y)$ and $\nu(x, y)$ in (3.63). As previously mentioned, this is not well justified, nevertheless, the variable-density model can be conceived as a

zeroth-order approximation of the variable-coefficients model.

The model that we choose to simulate the loaded plate vibrations was the variable-density model, as it represents the desired loading shape in a better way. It also is less complicated to implement computationally.

3.3.2 Damping term

As the quality factor of the plate is a feature that needs to be measure, a damping term is introduced in the equation of motion as an external force that is proportional to the infinitesimal moment in the z-direction, given by

$$q(r) = -2\sigma_0 \rho(r) h_1 \frac{\partial w}{\partial t}, \tag{3.75}$$

where $\sigma_0 \geq 0$ is a constant damping parameter.

By substituting this external force $q(r)$ in (3.41), the resultant equation of motion that integrates these modifications is

$$-D_1 \nabla^4 w = \rho(r) h_1 \Big(\frac{\partial^2 w}{\partial t^2} + 2\sigma_0 \frac{\partial w}{\partial t} \Big), \tag{3.76}$$

which can be re-written in terms of the space-dependant stiffness parameter as

$$\frac{\partial^2 w}{\partial t^2} = -\kappa^2(r) \nabla^4 w - 2\sigma_0 \frac{\partial w}{\partial t}. \tag{3.77}$$

This is the equation that will be approximated with a two dimensional finite difference method.

Effect of damping in an oscillator

In order to show the effect of the damping term, consider the solution of (3.77) to be given in terms of separation of variables, as

$$w(\bar{x}, t) = W(\bar{x}) T(t), \tag{3.78}$$

for the spatial variable $\bar{x} \in \Omega$ and time $t > 0$. By inserting (3.78) in the equation of motion (3.77) yields

$$WT'' = -\kappa^2 T \nabla^4 W - 2\sigma_0 W T'. \tag{3.79}$$

Dividing by TW, leads to

$$\frac{T''}{T} = -\kappa^2 \frac{\nabla^4 W}{W} - 2\sigma_0 \frac{T'}{T}, \tag{3.80}$$

which can be split by space and time dependence, using a separation constant, $-\omega_0^2$, as

$$\frac{T'' + 2\sigma_0 T'}{T}(t) = -\omega_0^2 = -\kappa^2 \frac{\nabla^4 W}{W}(\bar{x}). \tag{3.81}$$

Thus, the time dependant part of the solution has to satisfy

$$T'' = -\omega_0^2 T - 2\sigma_0 T'. \tag{3.82}$$

Assuming that $\sigma_0 \leq \omega_0$, the general solution to (3.82) can be written as

$$T(t) = e^{-\sigma_0 t}(A\cos(\omega_1 t) + B\sin(\omega_1 t)), \tag{3.83}$$

where $\omega_1 = \sqrt{\omega_0^2 - \sigma_0^2}$. Assuming a bounded spatial solution, $|W(\bar{x})| \leq M < \infty$, for all $\bar{x} \in \mathbb{R}^2$, the complete solution, w, has a bound given by

$$|w(\bar{x}, t)| \leq |W(\bar{x})| \cdot |T(t)| \leq Ce^{-\sigma_0 t} < C, \tag{3.84}$$

for a constant $C > 0$, for all $t > 0$ and for all $\bar{x} \in \mathbb{R}^2$.

Therefore, the damping term inserted in the equation of motion induces an exponential decay on the solution, with decay constant σ_0.

Chapter 4

Two dimensional finite difference method

4.1 Introduction

The Finite Difference Method (FDTD) is a computational procedure to obtain approximate solutions to partial differential equations (PDE). For a given partial differential equation, the solution the solution consists of replacing replacing the continuous solution to the equation by discrete functions, defined on discrete spatial and temporal points in the domain of interest, as well as replacing the differential operators involved by *discretised differential operators*. The discrete domain is known as the spatial and temporal *grid*, and the discrete functions are known as *grid functions*.

In order to approximate the PDE solution, the differential problem is replaced by an algebraic problem in terms of the grid function, provided by the *discretised differential operators* also known as *difference operators*. The above mentioned algebraic problem is known as the *finite difference scheme*. To obtain a *numerical solution* from schemes of this type, the algebraic expression is used to implement an iterative process in which the solution values at a certain time level are expressed in terms of the corresponding values at previous time levels. In this way, the solution to the discrete algebraic problem approximates the solution of the PDE as the spatial and/or temporal grid size increases (spatial or temporal step size decrease).

To obtain an approximated solution for a given initial-boundary value problem, the finite difference scheme, as well as the spatial and temporal grids, have to satisfy specific convergence and stability criteria, as well as the necessary boundary conditions. The aim of this chapter is to explain the main FDTD concepts and to describe the schemes applied to the solution of the loaded plate with damping model, previously obtained. The spatial domain of interest for the loaded plate model consists of a circle in $\mathbb{R}^2$. Thus, the FDTD will be applied in both a Cartesian and polar

Coordinates discretisation of the considered domain.

4.2 Grid functions and difference operators in Cartesian coordinates

4.2.1 Grid functions and discretised domains

A grid function in two spatial dimensions and one temporal dimension, can be represented as $u^n_{l,m}$, where $(l,m) \in D \subset \mathbb{Z}^2$, $n \in T \subset \mathbb{Z}^+$. The size and shape of the integers domains D and T depends on the continuous domain that wants to be approximated. The grid function represents a approximation to the continuous function $u(x,y,t)$, at the coordinates $x = lh_x$, $y = mh_y$, $t = nk$, where h_x and h_y are the grid spacing in the x and y directions, and k is the time-step size. Such an approximation is given over the domain

$$\mathbb{D} = \{(x,y,t) \in \Omega \times \mathbb{T} | x = lh_x,\, y = mh_y,\, t = nk,\, (l,m) \in D \subset \mathbb{Z}^2,\, n \in T \subset \mathbb{Z}^+\}, \tag{4.1}$$

where $\Omega \subset \mathbb{R}^2$ represents the discrete spatial domain and $\mathbb{T} \subset \mathbb{R}^+$ the discrete time domain.

If the continuous time domain of interest is given by $[0, T_f] \subset \mathbb{R}^+$, where $T_f \in \mathbb{R}^+$ represents the final time, the integer time domain can be given by $T = (0, \cdots, N_f)$, where N_f is the number of sub-divisions of the time interval, and the time step is given by $k = T_f/N_f$. Then, the discrete time domain is given by

$$\mathbb{T} = [0, \frac{T_f}{N_f}, 2\frac{T_f}{N_f}, \cdots, (N_f - 1)\frac{T_f}{N_f}, T_f] \tag{4.2}$$

For the case of a rectangular spatial domain with a corner in the origin and growing to the positive x and y directions, of length $L_x \times L_y$ the continuous domain is given by $[0, L_x] \times [0, L_y]$, and the integer domain can be given by

$$D = (0, 1, \cdots, N_x) \times (0, 1, \cdots, N_y),$$

where N_x+1 and N_y+1, the number of sub-divisions of $[0, L_x]$ and $[0, L_y]$ respectively. The grid spacings are given by $h_x = L_x/N_x$ and $h_y = L_y/N_y$. Like this, the discrete spatial domain is given by

$$\Omega = [0, \frac{L_x}{N_x}, 2\frac{L_x}{N_x}, \cdots, (N_x - 1)\frac{L_x}{N_x}, L_x] \times [0, \frac{L_y}{N_y}, 2\frac{L_y}{N_y}, \cdots, (N_y - 1)\frac{L_y}{N_y}, L_y]. \tag{4.3}$$

4.2.2 Discrete differential operators

The partial differential equation is transformed into an algebraic problem by discretizing the partial derivative operators. To achieve this, consider the Taylor series expansion of a function $u : \mathbb{R}^2 \times \mathbb{R}^+ \to \mathbb{R}$ around a point $(x,y,t) \in \mathbb{R}^2 \times \mathbb{R}^+$ in the x

direction, given by

$$\begin{aligned} u(x+h_x,y,t) = u(x,y,t) + h_x\frac{\partial u(x,y,t)}{\partial x} + h_x^2\frac{1}{2}\frac{\partial^2 u(x,y,t)}{\partial x^2} \\ + h_x^3\frac{1}{3!}\frac{\partial^3 u(x,y,t)}{\partial x^3} + O(h_x^4) \end{aligned} \tag{4.4}$$

where $O(h_x^4)$ indicates that the residual is at most of order h_x^4. The expression (4.4) is valid for positive and negative values of h_x, thus, considering $-h_x$, the Taylor's expansion is given as follows

$$\begin{aligned} u(x-h_x,y,t) = u(x,y,t) - h_x\frac{\partial u(x,y,t)}{\partial x} + h_x^2\frac{1}{2}\frac{\partial^2 u(x,y,t)}{\partial x^2} \\ - h_x^3\frac{1}{3!}\frac{\partial^3 u(x,y,t)}{\partial x^3} + O(h_x^4) \end{aligned} \tag{4.5}$$

By isolating the partial derivative of u with respect to x from (4.4), when truncating the expansion after the second term, one obtains

$$\begin{aligned} \frac{\partial u(x,y,t)}{\partial x} &= \frac{u(x+h_x,y,t) - u(x) + O(h_x^2)}{h_x} \\ &= \frac{u(x+h_x,y,t) - u(x)}{h_x} + O(h_x). \end{aligned} \tag{4.6}$$

Similarly, from (4.5) the same partial derivative is approximated by

$$\begin{aligned} \frac{\partial u(x,y,t)}{\partial x} &= \frac{u(x-h_x,y,t) - u(x) + O(h_x^2)}{-h_x} \\ &= \frac{u(x) - u(x-h_x,y,t)}{h_x} + O(h_x). \end{aligned} \tag{4.7}$$

Thus, two different approximations of order one, for the partial derivative of u with respect to x are obtained. On the other hand, by subtracting (4.5) from (4.4), truncating the expansion after the second term and isolating the same partial derivative, yields

$$\frac{\partial u(x,y,t)}{\partial x} = \frac{u(x+h_x,y,t) - u(x-h_x,y,t)}{2h_x} + O(h_x) \tag{4.8}$$

In this way, three different approximations for the first partial derivative with respect to x are obtained, the first two of order one and the third one of order two. These approximations can be expressed by *discrete differential operators* also known as *difference operators*, denoted by the Greek letter 'δ' with a sub-index that indicates the direction and type of approximation, acting on the grid function $u_{l,m}^n$ (which

indicates the approximation to the value of $u(lh_x, mh_y, nk))$, as

$$\begin{aligned}
\delta_{x+}u^n_{l,m} &= \frac{u^n_{l+1,m} - u^n_{l,m}}{h_x}, \quad \text{the 'forward approximation',} \\
\delta_{x-}u^n_{l,m} &= \frac{u^n_{l,m} - u^n_{l-1,m}}{h_x}, \quad \text{the 'backward approximation', and} \\
\delta_{x\cdot}u^n_{l,m} &= \frac{u^n_{l+1,m} - u^n_{l-1,m}}{2h_x}, \quad \text{the 'central approximation'.}
\end{aligned} \tag{4.9}$$

In the central approximation, second-order terms have been disregarded, while in the first two cases, terms from the first order onwards were neglected. It is then stated that the forward and backward approximations are of order one, and the central one is of order two. By following this method, an approximation to the second derivative of u can be made; for this purpose, (4.4) is added to (4.5), obtaining

$$u(x + h_x, y, t) + u(x - h_x, y, t) = 2u(x, y, t) + h_x^2 \frac{\partial^2 u(x, y, t)}{\partial x^2} + O(h_x^4). \tag{4.10}$$

Which leads to an approximation of the second partial derivative given by

$$\frac{\partial^2 u(x, y, t)}{\partial x^2} \approx \frac{u(x + h_x, y, t) - 2u(x, y, t) + u(x - h_x, y, t)}{h_x^2}, \tag{4.11}$$

or, given as a difference operator, by

$$\delta_{xx}u^n_{l,m} = \frac{u^n_{l+1,m} - 2u^n_{l,m} + u^n_{l-1,m}}{h_x^2}. \tag{4.12}$$

To obtain the order of the approximation of (4.12) to the second partial derivative of a function evaluated on the grid point (lh_x, mh_y, nk), consider the Taylor expansion of $u((l + 1)h_x, mh_y, nk)$ around the point (lh_x, mh_y, nk) given by

$$\begin{aligned}
u((l+1)h_x, mh_y, nk) &= u(lh_x, mh_y, nk) + h_x \frac{\partial u(lh_x, mh_y, nk)}{\partial x} + h_x^2 \frac{1}{2} \frac{\partial^2 u(lh_x, mh_y, nk)}{\partial x^2} \\
&+ h_x^3 \frac{1}{3!} \frac{\partial^3 u(lh_x, mh_y, nk)}{\partial x^3} + h_x^4 \frac{1}{4!} \frac{\partial^4 u(lh_x, mh_y, nk)}{\partial x^4} + h_x^5 \frac{1}{5!} \frac{\partial^5 u(lh_x, mh_y, nk)}{\partial x^5} \\
&+ h_x^6 \frac{1}{6!} \frac{\partial^6 u(lh_x, mh_y, nk)}{\partial x^6} + O(h_x^7)
\end{aligned} \tag{4.13}$$

and the expansion of $u((l - 1)h_x, mh_y, nk)$, given by

$$u((l-1)h_x, mh_y, nk) = u(lh_x, mh_y, nk) - h_x\frac{\partial u(lh_x, mh_y, nk)}{\partial x} + h_x^2\frac{1}{2}\frac{\partial^2 u(lh_x, mh_y, nk)}{\partial x^2}$$
$$- h_x^3\frac{1}{3!}\frac{\partial^3 u(lh_x, mh_y, nk)}{\partial x^3} + h_x^4\frac{1}{4!}\frac{\partial^4 u(lh_x, mh_y, nk)}{\partial x^4} + h_x^5\frac{1}{5!}\frac{\partial^5 u(lh_x, mh_y, nk)}{\partial x^5}$$
$$+ h_x^6\frac{1}{6!}\frac{\partial^6 u(lh_x, mh_y, nk)}{\partial x^6} + O(h_x^7). \tag{4.14}$$

By substituting in the difference operator (4.12), leads to

$$\frac{1}{h_x^2}(u((l+1)h_x, mh_y, nk) - 2u(lh_x, mh_y, nk) + u((l-1)h_x, mh_y, nk)) =$$
$$\frac{1}{h_x^2}\Bigg[\cancel{u(lh_x, mh_y, nk)} + \cancel{h_x\frac{\partial u(lh_x, mh_y, nk)}{\partial x}} + h_x^2\frac{1}{2}\frac{\partial^2 u(lh_x, mh_y, nk)}{\partial x^2}$$
$$+ \cancel{h_x^3\frac{1}{3!}\frac{\partial^3 u(lh_x, mh_y, nk)}{\partial x^3}} + h_x^4\frac{1}{4!}\frac{\partial^4 u(lh_x, mh_y, nk)}{\partial x^4} + O(h_x^5)$$
$$- \cancel{2u(lh_x, mh_y, nk)}$$
$$+ \cancel{u(lh_x, mh_y, nk)} - \cancel{h_x\frac{\partial u(lh_x, mh_y, nk)}{\partial x}} + h_x^2\frac{1}{2}\frac{\partial^2 u(lh_x, mh_y, nk)}{\partial x^2}$$
$$- \cancel{h_x^3\frac{1}{3!}\frac{\partial^3 u(lh_x, mh_y, nk)}{\partial x^3}} + h_x^4\frac{1}{4!}\frac{\partial^4 u(lh_x, mh_y, nk)}{\partial x^4} + O(h_x^5)\Bigg]$$
$$= \frac{\partial^2 u(lh_x, mh_y, nk)}{\partial x^2} + h_x^2\frac{2}{4!}\frac{\partial^4 u(lh_x, mh_y, nk)}{\partial x^4} + O(h_x^5) = \frac{\partial^2 u(lh_x, mh_y, nk)}{\partial x^2} + O(h_x^2), \tag{4.15}$$

which means that (4.12) approximates the second order partial derivative in the x direction with an accuracy of order h_x^2. This property can be said as that the difference operator is an approximation of second-order accuracy to the corresponding differential operator.

A direct substitution can show that the second partial derivative difference operator can be computed as

$$\delta_{xx} = \delta_{x+}\delta_{x-}. \tag{4.16}$$

Similarly, an approximation to a fourth order partial derivative can be found as

$$\delta_{xxxx} = \delta_{xx}\delta_{xx}, \tag{4.17}$$

which, when applied to the grid function, takes the form

$$\delta_{xxxx}u_{l,m}^n = \frac{u_{l+2,m}^n - 4u_{l+1,m}^n + 6u_{l,m}^n - 4u_{l-1,m}^n + u_{l-2,m}^n}{h_x^4}. \tag{4.18}$$

To obtain the order of approximation of (4.18), the Taylor expansions of a function

evaluated on the grid point $(l \pm 2, m, n)$, $u((l \pm 2)h_x, mh_y, nk)$, have to be considered, which are easily found by replacing h_x by $2h_x$ in (4.13) and (4.14), as

$$u((l+2)h_x, mh_y, nk) = u + 2h_x u_x + (2h_x)^2 \frac{1}{2} u_{xx} + (2h_x)^3 \frac{1}{3!} u_{xxx} + (2h_x)^4 \frac{1}{4!} u_{xxxx} + (2h_x)^5 \frac{1}{5!} u_{xxxxx} + (2h_x)^6 \frac{1}{6!} u_{xxxxxx} + O(h_x^7) \tag{4.19}$$

and

$$u((l-2)h_x, mh_y, nk) = u - 2h_x u_x + (2h_x)^2 \frac{1}{2} u_{xx} - (2h_x)^3 \frac{1}{3!} u_{xxx} + (2h_x)^4 \frac{1}{4!} u_{xxxx} - (2h_x)^5 \frac{1}{5!} u_{xxxxx} + (2h_x)^6 \frac{1}{6!} u_{xxxxxx} + O(h_x^7), \tag{4.20}$$

where the sub-index indicates a partial derivative with respect to the index variable the amount of times it appear, and all the functions are evaluated on (lh_x, mh_y, nk).

Then, evaluating, yields

$$\begin{aligned}
&\frac{1}{h_x^4}(u((l+2)h_x, mh_y, nk) - 4u((l+1)h_x, mh_y, nk) + 6u(lh_x, mh_y, nk) \\
&- 4u((l-1)h_x, mh_y, nk) + u((l-2)h_x, mh_y, nk)) = \\
&\frac{1}{h_x^4}\Bigg[\cancel{u} + \cancel{2h_x u_x} + \cancel{(2h_x)^2 \frac{1}{2} u_{xx}} + \cancel{(2h_x)^3 \frac{1}{3!} u_{xxx}} + (2h_x)^4 \frac{1}{4!} u_{xxxx} + \cancel{(2h_x)^5 \frac{1}{5!} u_{xxxxx}} \\
&+ (2h_x)^6 \frac{1}{6!} u_{xxxxxx} + O(h_x^7) - 4\Bigg(\cancel{u} + \cancel{h_x u_x} + \cancel{h_x^2 \frac{1}{2} u_{xx}} + \cancel{h_x^3 \frac{1}{3!} u_{xxx}} + h_x^4 \frac{1}{4!} u_{xxxx} + \\
&\cancel{h_x^5 \frac{1}{5!} u_{xxxxx}} + h_x^6 \frac{1}{6!} u_{xxxxxx} + O(h_x^7)\Bigg) + 6\cancel{u} - 4\Bigg(\cancel{u} - \cancel{h_x u_x} + \cancel{h_x^2 \frac{1}{2} u_{xx}} - \cancel{h_x^3 \frac{1}{3!} u_{xxx}} \\
&+ h_x^4 \frac{1}{4!} u_{xxxx} - \cancel{h_x^5 \frac{1}{5!} u_{xxxxx}} + h_x^6 \frac{1}{6!} u_{xxxxxx} + O(h_x^7)\Bigg) + \cancel{u} - \cancel{2h_x u_+} + \cancel{(2h_x)^2 \frac{1}{2} u_{xx}} \\
&- \cancel{(2h_x)^3 \frac{1}{3!} u_{xxx}} + (2h_x)^4 \frac{1}{4!} u_{xxxx} - \cancel{(2h_x)^5 \frac{1}{5!} u_{xxxxx}} + (2h_x)^6 \frac{1}{6!} u_{xxxxxx} + O(h_x^7)\Bigg] \\
&= \frac{1}{h_x^4}\left[h_x^4 \cancel{24} \frac{1}{\cancel{4!}} u_{xxxx} + h_x^6 \frac{120}{6!} u_{xxxxxx} + O(h_x^7)\right] = \frac{\partial^4 u(lh_x, mh_y, nk)}{\partial x^4} + O(h_x^2),
\end{aligned} \tag{4.21}$$

which implies that (4.18) is a second-order accuracy approximation.

In a similar way, the difference operators that approximates the partial derivatives with respect to y and t can be found by adapting the action of the analogous operator in the x direction to the adequate coordinate. Thus, said difference operators are given

by

$$\begin{aligned}
\delta_{y+}u^n_{l,m} =& \frac{u^n_{l,m+1}-u^n_{l,m}}{h_y}, \quad \delta_{y-}u^n_{l,m} = \frac{u^n_{l,m}-u^n_{l,m-1}}{h_y},\\
\delta_{y\cdot}u^n_{l,m} =& \frac{u^n_{l,m+1}-u^n_{l,m-1}}{2h_y}, \quad \delta_{yy}u^n_{l,m} = \frac{u^n_{l,m+1}-2u^n_{l,m}+u^n_{l,m-1}}{h_y^2},\\
\delta_{yyyy}u^n_{l,m} =& \frac{u^n_{l,m+2}-4u^n_{l,m+1}+6u^n_{l,m}-4u^n_{l,m-1}+u^n_{l,m-2}}{h_y^4},
\end{aligned} \tag{4.22}$$

and

$$\begin{aligned}
\delta_{t+}u^n_{l,m} =& \frac{u^{n+1}_{l,m}-u^n_{l,m}}{k}, \quad \delta_{t-}u^n_{l,m} = \frac{u^n_{l,m}-u^{n-1}_{l,m}}{k},\\
\delta_{t\cdot}u^n_{l,m} =& \frac{u^{n+1}_{l,m}-u^{n-1}_{l,m}}{2k}, \quad \delta_{tt}u^n_{l,m} = \frac{u^{n+1}_{l,m}-2u^n_{l,m}+u^{n-1}_{l,m}}{k^2}.
\end{aligned} \tag{4.23}$$

A condition that will be employ in this work is known as *equal grid spacing*, and consists in taking the grid spacing in the x and y directions equal to the same constant, this is

$$h_x = h_y = h. \tag{4.24}$$

The discrete Laplacian operator can be given in terms of the previously obtained difference operators as

$$\delta_{\nabla^2} = \delta_{xx} + \delta_{yy} = \nabla^2 + O(h^2), \tag{4.25}$$

where the second-order of accuracy is inherit from the operators involved.

In a similar way as how the fourth order partial derivative difference operator was found in (4.17), the discrete biharmonic operator can be given in terms of the discrete Laplacian operator as

$$\begin{aligned}
\delta_{\nabla^4} &= \delta_{\nabla^2}\delta_{\nabla^2}\\
&= (\delta_{xx}+\delta_{yy})(\delta_{xx}+\delta_{yy}) = \delta_{xx}\delta_{xx}+\delta_{xx}\delta_{yy}+\delta_{yy}\delta_{xx}+\delta_{yy}\delta_{yy}\\
\delta_{xx}\delta_{xx} &+ 2\delta_{xx}\delta_{yy}+\delta_{yy}\delta_{yy} = \delta_{xxxx}+2\delta_{xx}\delta_{yy}+\delta_{yyyy}.
\end{aligned} \tag{4.26}$$

To obtain the order of accuracy of the biharmonic difference operator, we need to compute the order of accuracy of $\delta_{xx}\delta_{yy}$, which, when is applied to a grid function has the form

$$\begin{aligned}
\delta_{xx}\delta_{yy}u^n_{l,m} = \frac{1}{h^4}\Big[& u^n_{l+1,m+1}-2u^n_{l,m+1}+u^n_{l-1,m+1}-2(u^n_{l+1,m}-2u^n_{l,m}+u^n_{l-1,m})\\
&+u^n_{l+1,m-1}-2u^n_{l,m-1}+u^n_{l-1,m-1}\Big].
\end{aligned} \tag{4.27}$$

Thus, the order of accuracy can be obtain by considering the Taylor expansion in

two directions given by

$$u((l\pm1)h,(m+1)h,nk) = u + h(\pm u_x + u_y) + \frac{1}{2}h^2(u_{xx} \pm 2u_{xy} + u_{yy})$$
$$+ \frac{1}{3!}h^3(\pm u_{xxx} + 3u_{xxy} \pm 3u_{yyx} + u_{yyy}) + \frac{1}{4!}h^4(u_{xxxx} \pm 4u_{xxxy} + 6u_{xxyy} \pm 4u_{yyyx} + u_{yyyy})$$
$$+ \frac{1}{5!}h^5(\pm u_{xxxxx} + 5u_{xxxxy} \pm 10u_{xxxyy} + 10u_{xxyyy} \pm 5u_{yyyyx} + u_{yyyyy})$$
$$+ \frac{1}{6!}h^6(u_{xxxxxx} \pm 6u_{xxxxxy} + 15u_{xxxxyy} \pm 20u_{xxxyyy} + 15u_{yyyyxx} \pm 6u_{xyyyyy} + u_{yyyyyy}) + O(h^7), \tag{4.28}$$

$$u((l+1)h,(m\pm1)h,nk) = u + h(u_x \pm u_y) + \frac{1}{2}h^2(u_{xx} \pm 2u_{xy} + u_{yy})$$
$$+ \frac{1}{3!}h^3(u_{xxx} \pm 3u_{xxy} + 3u_{yyx} \pm u_{yyy}) + \frac{1}{4!}h^4(u_{xxxx} \pm 4u_{xxxy} + 6u_{xxyy} \pm 4u_{yyyx} + u_{yyyy})$$
$$+ \frac{1}{5!}h^5(u_{xxxxx} \pm 5u_{xxxxy} + 10u_{xxxyy} \pm 10u_{xxyyy} + 5u_{yyyyx} \pm u_{yyyyy})$$
$$+ \frac{1}{6!}h^6(u_{xxxxxx} \pm 6u_{xxxxxy} + 15u_{xxxxyy} \pm 20u_{xxxyyy} + 15u_{yyyyxx} \pm 6u_{xyyyyy} + u_{yyyyyy}) + O(h^7), \tag{4.29}$$

and

$$u((l-1)h,(m-1)h,nk) = u - h(u_x + u_y) + \frac{1}{2}h^2(u_{xx} + 2u_{xy} + u_{yy})$$
$$- \frac{1}{3!}h^3(u_{xxx} + 3u_{xxy} + 3u_{yyx} + u_{yyy}) + \frac{1}{4!}h^4(u_{xxxx} + 4u_{xxxy} + 6u_{xxyy} + 4u_{yyyx} + u_{yyyy})$$
$$- \frac{1}{5!}h^5(u_{xxxxx} + 5u_{xxxxy} + 10u_{xxxyy} + 10u_{xxyyy} + 5u_{yyyyx} + u_{yyyyy})$$
$$+ \frac{1}{6!}h^6(u_{xxxxxx} + 6u_{xxxxxy} + 15u_{xxxxyy} + 20u_{xxxyyy} + 15u_{yyyyxx} + 6u_{xyyyyy} + u_{yyyyyy}) + O(h^7) \tag{4.30}$$

Then, evaluating,

$$\delta_{xx}\delta_{yy}u(lh,mh,nk) = \frac{1}{h^4}\Big[u((l+1)h,(m+1)h,nk) - 2u(lh,(m+1)h,nk)$$
$$+ u((l-1)h,(m+1)h,nk) - 2(u((l+1)h,mh,nk) - 2u(lh,mh,nk) + u((l-1)h,mh,nk))$$
$$+ u((l+1)h,(m-1)h,nk) - 2u(lh,(m-1)h,nk) + u((l-1)h,(m-1)h,nk)\Big] =$$

$$\frac{1}{h^4}\Bigg[\cancel{u}^{(1)}+\cancel{h(u_x+u_y)}^{(3)}+\frac{1}{2}h^2\cancel{(u_{xx}+2u_{xy}+u_{yy})}^{(5)(6)(7)}+\frac{1}{\cancel{3!}}h^3\cancel{(u_{xxx}+3u_{xxy}+3u_{yyx}+u_{yyy})}^{(8)}$$

$$+\frac{1}{4!}h^4\cancel{(u_{xxxx}+4u_{xxxy}+6u_{xxyy}+4u_{yyyx}+u_{yyyy})}^{(10)(11)(12)(13)}+\frac{1}{\cancel{5!}}h^5\cancel{(u_{xxxxx}+5u_{xxxxy}+10u_{xxxyy}}^{(14)}$$

$$+10u_{xxyyy}+5u_{yyyyx}+u_{yyyyy})+\frac{1}{6!}h^6\cancel{(u_{xxxxxx}+6u_{xxxxxy}+15u_{xxxxyy}+20u_{xxxyyy}}^{(18)(19)(20)}$$

$$+15u_{yyyyxx}+\cancel{6u_{xyyyyy}+6u_{yyyyyy})}^{(21)(22)}+O(h^7)-2(\cancel{u}^{(1)}+\cancel{hu_y}^{(2)}+h^2\frac{1}{2}\cancel{u_{yy}}^{(7)}+h^3\frac{1}{3!}\cancel{u_{yyy}}^{(16)}+h_x^4$$

$$\frac{1}{4!}\cancel{u_{yyyy}}^{(13)}+h^5\frac{1}{5!}\cancel{u_{yyyyy}}^{(17)}+h^6\frac{1}{6!}\cancel{6u_{yyyyyy}}^{(22)}+O(h_x^7))+\cancel{u}^{(1)}+\cancel{h(-u_x+u_y)}^{(4)}+\frac{1}{2}h^2\cancel{(u_{xx}-2u_{xy}+u_{yy})}^{(5)(6)(7)}$$

$$+\frac{1}{\cancel{3!}}h^3\cancel{(-u_{xxx}+3u_{xxy}-3u_{yyx}+u_{yyy})}^{(9)}+\frac{1}{4!}h^4\cancel{(u_{xxxx}-4u_{xxxy}+6u_{xxyy}-4u_{yyyx}+u_{yyyy})}^{(10)(11)(12)(13)}$$

$$+\frac{1}{\cancel{5!}}h^5\cancel{(-u_{xxxxx}+5u_{xxxxy}-10u_{xxxyy}+10u_{xxyyy}-5u_{yyyyx}+u_{yyyyy})}^{(15)}$$

$$+\frac{1}{6!}h^6\cancel{(u_{xxxxxx}-6u_{xxxxxy}+15u_{xxxxyy}-20u_{xxxyyy}+15u_{yyyyxx}-6u_{xyyyyy}+6u_{yyyyyy})}^{(18)(19)(20)(21)(22)}+O(h^7)$$

$$-2(\cancel{h^2u_{xx}}^{(5)}+h^4\frac{2}{4!}\cancel{u_{xxxx}}^{(10)}+h^6\frac{2}{6!}\cancel{u_{xxxxxx}}^{(18)}+O(h^7))+\cancel{u}^{(1)}+\cancel{h(u_x-u_y)}^{(4)}+\frac{1}{2}h^2\cancel{(u_{xx}-2u_{xy}+u_{yy})}^{(5)(6)(7)}$$

$$+\frac{1}{\cancel{3!}}h^3\cancel{(u_{xxx}-3u_{xxy}+3u_{yyx}-u_{yyy})}^{(9)}+\frac{1}{4!}h^4\cancel{(u_{xxxx}-4u_{xxxy}+6u_{xxyy}-4u_{yyyx}+u_{yyyy})}^{(10)(11)(12)(13)}$$

$$+\frac{1}{\cancel{5!}}h^5\cancel{(u_{xxxxx}-5u_{xxxxy}+10u_{xxxyy}-10u_{xxyyy}+5u_{yyyyx}-u_{yyyyy})}^{(15)}$$

$$+\frac{1}{6!}h^6\cancel{(u_{xxxxxx}-6u_{xxxxxy}+15u_{xxxxyy}-20u_{xxxyyy}+15u_{yyyyxx}-6u_{xyyyyy}+6u_{yyyyyy})}^{(18)(19)(20)(21)(22)}+O(h^7)$$

$$-2(\cancel{u}^{(1)}-\cancel{hu_y}^{(2)}+h^2\frac{1}{2}\cancel{u_{yy}}^{(7)}-h^3\frac{1}{3!}\cancel{u_{yyy}}^{(16)}+h_x^4\frac{1}{4!}\cancel{u_{yyyy}}^{(13)}-h^5\frac{1}{5!}\cancel{u_{yyyyy}}^{(17)}+h^6\frac{1}{6!}\cancel{6u_{yyyyyy}}^{(22)}+O(h_x^7))$$

$$+\cancel{u}^{(1)}-\cancel{h(u_x+u_y)}^{(3)}+\frac{1}{2}h^2\cancel{(u_{xx}+2u_{xy}+u_{yy})}^{(5)(6)(7)}-\frac{1}{\cancel{3!}}h^3\cancel{(u_{xxx}+3u_{xxy}+3u_{yyx}+u_{yyy})}^{(8)}$$

$$+\frac{1}{4!}h^4\cancel{(u_{xxxx}+4u_{xxxy}+6u_{xxyy}+4u_{yyyx}+u_{yyyy})}^{(10)(11)(12)(13)}$$

$$-\frac{1}{\cancel{5!}}h^5\cancel{(u_{xxxxx}+5u_{xxxxy}+10u_{xxxyy}+10u_{xxyyy}+5u_{yyyyx}+u_{yyyyy})}^{(14)}$$

$$+\frac{1}{6!}h^6\cancel{(u_{xxxxxx}+6u_{xxxxxy}+15u_{xxxxyy}+20u_{xxxyyy}+15u_{yyyyxx}+6u_{xyyyyy}+6u_{yyyyyy})}^{(18)(19)(20)(21)(22)}+O(h^7)\Bigg] \tag{4.31}$$

$$= \frac{1}{h^4}\left[h^4 \frac{\cancel{24}}{\cancel{4!}} u_{xxyy} + \frac{60}{6!}h^6(u_{xxxxyy} + u_{yyyyxx})\right] = \frac{\partial^4 u}{\partial x^2 \partial y^2}(lh, mh, nk) + O(h^2),$$

where the cancelling arrows super-index indicates the terms that cancel each other. This implies that $\delta_{xx}\delta_{yy}$ is of second-order of accuracy, and, therefore, the difference operator δ_{∇^4} is of second-order of accuracy as well.

In general, one can choose unequal grid spacings, as well as different definitions of the difference operators. In this section is shown the approximations that were used in this work. For more information about other type of approximations consult [Bilbao, 2009].

4.3 Grid functions and difference operators in polar coordinates

4.3.1 Grid functions and discretised domains

The polar coordinates are usually employ to deal with systems defined over a circular geometry. In this case, a grid function $u^n_{l,m}$, with $(l, m) \in D \subset \mathbb{Z}^2$ and $n \in T \subset \mathbb{Z}^+$, represents an approximation to a continuous function $u(r, \theta, t)$ at the coordinates $r = lh_r$, $\theta = mh_\theta$ and $t = nk$, where k represents the time-step value, while h_r and h_θ represent the grid spacings in the radial and angular direction respectively, which, in general will not be have the same value. One particularity of this discretisation, is that the grid value at $(l = 0, m)$ has to be the same for all m, as it corresponds to the point $(r = 0, mh_\theta)$, this makes that the value of $u^n_{0,m}$ has to be the same for all m at each temporal step n. This single value is denoted by $u^n_{0,0}$. This particularity has implications in the definition of the difference operators when acting on the origin or close to it.

The time domain description is the same as the one presented before. For a circular domain centred on the origin of radius R the integer domain is given by

$$D = [0, \cdots, N_r] \times [0, N_\theta - 1] \tag{4.32}$$

where $N_r + 1$ and N_θ are the number of sub-divisions in the radial and angular directions, respectively. The grid spacings are given by $h_r = 1/N_r$ and $h_\theta = 2\pi/N_\theta$. Then, the discrete spatial domain is given by

$$\Omega =$$

$$[0, \frac{R}{N_r}, 2\frac{R}{N_r}, \cdots, (N_r - 1)\frac{R}{N_r}, R] \times [0, \frac{2\pi}{N_\theta}, 2\frac{2\pi}{N_\theta}, \cdots, (N_\theta - 1)\frac{2\pi}{N_\theta}]. \tag{4.33}$$

4.3.2 Discrete differential operators

Analogously as the difference operators in Cartesian coordinates previously found, the forward, backward, and centred difference operators in polar coordinates, for the

grid functions evaluated in the interior of the discretised domain, are given by

$$\begin{aligned}\delta_{r+}u^n_{l,m} =& \frac{u^n_{l+1,m} - u^n_{l,m}}{h_r},\\ \delta_{r-}u^n_{l,m} =& \frac{u^n_{l,m} - u^n_{l-1,m}}{h_r},\\ \delta_{r\cdot}u^n_{l,m} =& \frac{u^n_{l+1,m} - u^n_{l-1,m}}{2h_r},\end{aligned} \tag{4.34}$$

and

$$\begin{aligned}\delta_{\theta+}u^n_{l,m} =& \frac{u^n_{l,m+1} - u^n_{l,m}}{h_\theta},\\ \delta_{\theta-}u^n_{l,m} =& \frac{u^n_{l,m} - u^n_{l,m-1}}{h_\theta},\\ \delta_{\theta\cdot}u^n_{l,m} =& \frac{u^n_{l,m+1} - u^n_{l,m-1}}{2h_\theta}.\end{aligned} \tag{4.35}$$

And the second order difference operators (for the grid functions evaluated in the interior of the discrete domain) are

$$\delta_{rr}u^n_{l,m} = \frac{u^n_{l+1,m} - 2u^n_{l,m} + u^n_{l-1,m}}{h_r^2}, \quad \delta_{\theta\theta}u^n_{l,m} = \frac{u^n_{l,m+1} - 2u^n_{l,m} + u^n_{l,m-1}}{h_\theta^2}. \tag{4.36}$$

As previously mentioned, the polar coordinates main feature is the condition that has to be imposed in the origin, when $l = 0$. This turns evident when dealing with the Laplacian operator, which, in polar coordinates, takes the form

$$\nabla^2 = \frac{1}{r}\frac{\partial}{\partial r}\left(r\frac{\partial}{\partial r}\right) + \frac{1}{r^2}\frac{\partial^2}{\partial\theta^2} = \frac{\partial^2}{\partial r^2} + \frac{1}{r}\frac{\partial}{\partial r} + \frac{1}{r^2}\frac{\partial^2}{\partial\theta^2}. \tag{4.37}$$

The term $1/r$ can lead to a discontinuity on the difference operator if it is not define adequately. It is important to realise that any difficulties that may arise at the origin are only a result of the choice of coordinate system, and are not necessarily a reflection of the continuous solution $u(r, \theta, t)$. The definition for the Laplacian difference operator in polar coordinates that will be applied in this work is the one that can be found in [Strikwerda, 2004] and [Bilbao, 2009], and is given, for $l > 0$, by

$$\delta_{\nabla^2\circ} = \frac{1}{r}\delta_{r+}((\mu_{r-}r)\delta_{r-}) + \frac{1}{r^2}\delta_{\theta\theta} \tag{4.38}$$

where $r = lh_r$, and μ_{r-} is the *backward average operator*, that operates on a grid function as

$$\mu_{r-}u^n_{l,m} = \frac{1}{2}(u^n_{l,m} + u^n_{l-1,m}), \tag{4.39}$$

this is, it takes the geometrical average of a grid function evaluated in a grid point and the one 'before' in certain direction. It can also be understood as a approximation

to the identity operator in a discrete domain. Further information about averaging operators can be consulted in [Bilbao, 2009]. When is applied to the grid function $r = lh_r$, yields

$$\mu_{r-} r = \mu_{r-} l h_r = \frac{1}{2}(lh_r + (l-1)h_r) = (l - \frac{1}{2})h_r \approx 1 \cdot r. \tag{4.40}$$

Therefore, the expanded the Laplacian difference operator (4.38) acting on a grid function is given by

$$\begin{aligned}
\delta_{\nabla^2 \circ} u^n_{l,m} &= \frac{1}{lh_r^2}\left(\left(l+\frac{1}{2}\right)u^n_{l+1,m} - 2lu^n_{l,m} + \left(l-\frac{1}{2}\right)u^n_{l-1,m}\right) \\
&+ \frac{1}{l^2 h_r^2 h_\theta^2}\left(u^n_{l,m+1} - 2u^n_{l,m} + u^n_{l,m-1}\right) \\
&= \frac{1}{lh_r^2}\left(l(u^n_{l+1,m} - 2u^n_{l,m} + u^n_{l-1,m}) + \frac{1}{2}(u^n_{l+1,m} - u^n_{l-1,m})\right) \\
&+ \frac{1}{l^2 h_r^2 h_\theta^2}\left(u^n_{l,m+1} - 2u^n_{l,m} + u^n_{l,m-1}\right) \\
&= \frac{1}{h_r^2}(u^n_{l+1,m} - 2u^n_{l,m} + u^n_{l-1,m}) + \frac{1}{lh_r}\frac{1}{2h_r}(u^n_{l+1,m} - u^n_{l-1,m}) \\
&+ \frac{1}{l^2 h_r^2 h_\theta^2}\left(u^n_{l,m+1} - 2u^n_{l,m} + u^n_{l,m-1}\right),
\end{aligned} \tag{4.41}$$

for $l > 0$. Then, the Laplacian difference operator can be also expressed as

$$\delta_{\nabla^2 \circ} = \delta_{rr} - \frac{1}{r}\delta_{r\cdot} + \frac{1}{r^2}\delta_{\theta\theta}. \tag{4.42}$$

As the difference operators involved are of second-order accuracy, the Laplacian difference operator that acts on the grid points with $l > 0$ is also of second-order accuracy.

At the centre point, a special form is necessary. As an heuristic, and in order to introduce and gain intuition about the approximation of the Laplacian difference operator at the centre point, consider the partial differential equation

$$f(r, \theta, u, u_t, u_{tt}) = \nabla^2 u = \frac{1}{r}\frac{\partial}{\partial r}\left(r\frac{\partial u}{\partial r}\right) + \frac{1}{r^2}\frac{\partial^2 u}{\partial \theta^2}, \tag{4.43}$$

where the sub index in u_t and u_{tt} indicates partial derivatives with respect to t and $f(r, \theta, u, u_t, u_{tt})$ is a general function defined over a neighbourhood of the origin (as u, u_t, u_{tt} are also functions of r and θ they also have to be defined in the same neighbourhood). Then, consider the integral of the PDE over a disc of radius ε,

$$\int_0^\varepsilon \int_0^{2\pi} f(r, \theta, u, u_t, u_{tt}) r \, d\theta dr = \int_0^\varepsilon \int_0^{2\pi} \left[\frac{1}{r}\frac{\partial}{\partial r}\left(r\frac{\partial u}{\partial r}\right) + \frac{1}{r^2}\frac{\partial^2 u}{\partial \theta^2}\right] r \, d\theta dr. \tag{4.44}$$

The integral of the Laplacian operator can be split as

$$\int_0^{\varepsilon}\int_0^{2\pi}\left[\frac{1}{r}\frac{\partial}{\partial r}\left(r\frac{\partial u}{\partial r}\right)\right] r\,d\theta dr = \int_0^{2\pi}\int_0^{\varepsilon}\frac{\partial}{\partial r}\left(r\frac{\partial u}{\partial r}\right)\,dr d\theta = \int_0^{2\pi}\frac{\partial u}{\partial r}\varepsilon\,d\theta, \tag{4.45}$$

and

$$\int_0^{\varepsilon}\int_0^{2\pi}\left[\frac{1}{r^2}\frac{\partial^2 u}{\partial\theta^2}\right] r\,d\theta dr = \int_0^{\varepsilon}\int_0^{2\pi}\frac{1}{r}\frac{\partial^2 u}{\partial\theta^2}\,d\theta dr = \int_0^{\varepsilon}\left[\cancelto{0}{\frac{1}{r}\frac{\partial u}{\partial\theta}\Big|_0^{2\pi}} - \int_0^{2\pi}\frac{\partial u}{\partial\theta}\cancelto{0}{\frac{\partial}{\partial\theta}\left(\frac{1}{r}\right)}\,d\theta\right] dr = 0, \tag{4.46}$$

where the integration by parts over the angular integral was applied and the periodicity of $\frac{\partial u}{\partial\theta}$ on the angular direction was used to discard the boundary term, then

$$\int_0^{\varepsilon}\int_0^{2\pi}\left[\frac{1}{r}\frac{\partial}{\partial r}\left(r\frac{\partial u}{\partial r}\right) + \frac{1}{r^2}\frac{\partial^2 u}{\partial\theta^2}\right] r\,d\theta dr = \int_0^{2\pi}\frac{\partial u}{\partial r}\varepsilon\,d\theta. \tag{4.47}$$

By choosing $\varepsilon = h_r/2$, replacing u by the grid function $u_{l,m}^n$, approximating the partial derivative with respect to r by δ_{r+} (at $l = 0$) and discretizing the integral as a sum, we have

$$\int_0^{2\pi}\frac{\partial u}{\partial r}\varepsilon\,d\theta \approx \sum_{m=0}^{N_\theta-1}\frac{u_{1,m}^n - u_{0,m}^n}{h_r}\frac{h_r}{2}h_\theta = \sum_{m=0}^{N_\theta-1}\frac{u_{1,m}^n - u_{0,m}^n}{2}h_\theta, \tag{4.48}$$

The approximation $\varepsilon = h_r/2$ on right hand side of the integral of the PDE (4.44) can be taken as the value of f in the origin (denoted by $f(0)$), which implies also to take the values of the grid functions of u_t and u_{tt} in the origin ($l = 0, m = 0$), leading to

$$f(0)\left(\frac{h_r}{2}\right)^2\pi = \sum_{m=0}^{N_\theta-1}\frac{u_{1,m}^n - u_{0,m}^n}{2}h_\theta. \tag{4.49}$$

By replacing $h_\theta = 2\pi/N_\theta$

$$f(0)\left(\frac{h_r^2}{4}\right)\cancel{\pi} = \frac{\cancel{2}\cancel{\pi}}{N_\theta}\sum_{m=0}^{N_\theta-1}\frac{u_{1,m}^n - u_{0,m}^n}{\cancel{2}}. \tag{4.50}$$

So, finally

$$f(0) = \frac{4}{N_\theta h_r^2}\sum_{m=0}^{N_\theta-1}(u_{1,m}^n - u_{0,0}^n). \tag{4.51}$$

Therefore, a reasonable approximation to the Laplacian operator in the origin given by

$$\delta_{\nabla^2\circ}u_{0,0}^n = \frac{4}{N_\theta h_r^2}\sum_{m=0}^{N_\theta-1}(u_{1,m}^n - u_{0,0}^n). \tag{4.52}$$

This form of the Laplacian difference operator acting on the origin is given as a defini-

tion in [Bilbao, 2009] and a draft of the heuristic can be found in [Strikwerda, 2004]. This approximation preserves the second-order accuracy of (4.42).

In order to approximate the biharmonic operator, needed to model the plate's equation of motion, a procedure was developed by the author. The approximation methods in the literature were found not to be convergent (for example the one in [Bilbao, 2009]). As this procedure was developed to solve the equation of motion of the plate, a more natural way to explain is when the complete scheme for the equation of motion is presented. This will be done in a subsequent section.

As a brief introduction, a sketch of this procedure can be presented by taking an auxiliary function, v, such that $v = \nabla^2 u$, then apply the proper conditions at the central point and on the boundary, and then compute the complete scheme using $\nabla^2 v$ as the biharmonic of u. This procedure was tested and showed an appropriate behaviour, in terms of the capability to replicate the analytical results for a homogeneous circular plate.

4.4 Convergence, Consistency and Stability

The fundamental requirement of a finite difference scheme is to produce numerical solutions that approximate the solution of the corresponding differential equation. As the grid spacing is reduced, the approximation should progressively improve. A numerical scheme that fulfils this criterion is referred to as a *convergent* scheme. A general definition of this concept is given in the following definition.

Definition 4.4.1 (Convergence)**.** *A finite difference scheme approximating a partial differential equation is a convergent scheme if for any solution to the partial differential equation $u(t, \bar{x})$, and solutions to the finite difference scheme, such that $u^0_{l,m}$ converges to $u(0, \bar{x})$ as (lh_x, mh_y) converges to $\bar{x}$, then $u^n_{l,m}$ converges to $u(t, \bar{x})$ as nk converges to t, and (lh_x, mh_y) converges to $\bar{x}$, as h_x, h_y, k converge to 0.*

In general, to prove convergence for a given finite difference scheme can be too complicated, if attempted in a direct manner. However, there are two related concepts that are easy to check: consistency and stability. First, we define consistency.

Definition 4.4.2 (Consistency)**.** *Given a partial differential equation, $Pu = f$, and a finite difference scheme, $P_{n,l,m}u = f_{n,l,m}$, the finite difference scheme is consistent with the partial differential equation if for any solution $u(t, \bar{x})$ to the PDE*

$$P_{n,l,m}(u(nk, lh_x, mh_y)) - f_{n,l,m} \to 0,$$

as h_x, h_y, k converge to 0.

A standard way to prove consistency, is to replace a hypothetical exact solution to the PDE in the finite difference scheme, then, compute the truncation error (or residual, as previously done to compute the approximation error of the difference operators), by expanding in Taylor's series, in terms of the grid spacings $(k, h_x, h_y, ...)$

and show that, as the grid spacings converge to 0, the truncation error also converges to 0. A explicit example of this method will be shown in a subsequent section.

For a PDE with bounded solutions, the fact that a grid function converge to such a solution, somehow implies that the the grid function has to also be bounded in some way. This property is known as stability, and there are many ways to define it, depending on the kind of problem that wants to be solved. A general definition for time-evolving problems is given by

Definition 4.4.3 (Stability)**.** *A finite difference scheme is stable (in the sense of Lax) if the discrete solution satisfy that $|u_{l,m}^n|$ is uniformly bounded when $h_x, h_y \to 0$ and for all $n \in T \subset \mathbb{Z}^+$.*

In this work, the procedure to prove stability that will be apply is known as the *Von Neumann analysis* or *Fourier method*, and consists in replacing a ansatz given by

$$u_{l,m}^n = \zeta^n e^{i(\beta_x l h_x + \beta_y m h_y)} \tag{4.53}$$

in the finite difference scheme and find a relation between the grid spacings that ensure that such an ansatz in bounded. By evaluating (4.53) in a given finite difference scheme a polynomial function of ζ

$$P(\zeta) = \sum_{i=0}^{N} a_l(\beta_x, \beta_y)\zeta^l = 0, \tag{4.54}$$

known as *amplification polynomials* can be found. To ensure a bounded solution it is therefore sufficient to ensure that $|\zeta| \leq 1$, because then

$$|u_{l,m}^n| \leq |\zeta|^n \leq 1 \tag{4.55}$$

for all $n \in \mathbb{Z}^+$. Thus, finding the roots of the amplification polynomial that are bounded by the unity can lead to stability conditions.

4.4.1 Lax-Richtmyer equivalence theorem

The significance of consistency and stability within the study of finite difference schemes for initial value problems is demonstrated by the Lax-Richtmyer equivalence theorem.

Theorem 1 (Lax-Richtmyer Theorem)**.** *A consistent finite difference scheme for a partial differential equation for which the initial value problem is well-posed is convergent if and only if it is stable.*

The Lax-Richtmyer equivalence theorem establishes a profound connection between the concepts of convergence and stability. It implies that, for a scheme that approximates a PDE, i.e. is consistent with it, to provide a convergent solution, it must also be stable to ensure that errors do not grow uncontrollably. The theorem serves as a powerful tool in analysing and designing numerical methods for initial

value problems, offering a clear criterion to assess the performance and reliability of finite difference schemes. A prove of this theorem can be found in [Strikwerda, 2004].

4.5 Finite difference scheme of the loaded and damped plate model

The Finite Difference Method, in both, Cartesian and polar coordinates, was applied to solve the initial-boundary value problem, given by the equation of motion of a clamped circular plate with variable stiffness coefficient and damping:

$$\begin{cases} u_{tt} = -\kappa^2(\bar{x})\nabla^4 u - 2\sigma_0 u_t, \quad \text{for} \quad \bar{x} \in \Omega,\, t > 0, \\ u(\bar{x}, t=0) = u_0(\bar{x}) \quad \text{in} \quad \Omega, \\ u_t(\bar{x}, t=0) = v_0(\bar{x}) \quad \text{in} \quad \Omega, \\ u = u_r = 0, \quad \text{on} \quad \partial\Omega,\, \forall t, \end{cases} \tag{4.56}$$

where the sub-index expresses a partial derivative with respect to the index variable, $\bar{x} = (x, y)$ or (r, θ), depending on the coordinate system that is been used, $\sigma_0 \geq 0$ represents the damping parameter, Ω represents the spatial domain, $\partial\Omega$ represents the spatial domain's border, and the space-dependant stiffness parameter is given by

$$\kappa^2(\bar{x}) = \frac{D(\bar{x})}{\rho(\bar{x})H(\bar{x})L^4}, \tag{4.57}$$

where

$$D(\bar{x}) = \frac{E(\bar{x})H^3(\bar{x})}{12(1-\nu^2(\bar{x}))}. \tag{4.58}$$

Now, H represents the thickness of the plate and L is a distance scaling factor given by the plate's diameter for the the Cartesian coordinates scheme, and by the plate's radius for the the polar coordinates scheme (further information on the scaling can be found in section 6.2.1). In what follows, both finite difference schemes will be described. For the Cartesian scheme, the consistency and stability conditions will be formally derived. As the polar coordinate scheme was developed computationally by modifying the explicit version of the scheme proposed in [Bilbao, 2009] (section 12.6), stability and consistency conditions will be proven by comparing its performance with the analytical solutions for an homogeneous clamped circular plate (obtained in the section 3.2.4) in the section 6.5.

4.5.1 Cartesian coordinates

Finite difference scheme

In Cartesian coordinates, assuming a equal spatial grid spacing, h, the finite difference scheme used to approximate the equation of motion in (4.56) is given by

$$\delta_{tt} u^n_{l,m} = -\kappa^2_{l,m} \delta_{\nabla^4} u^n_{l,m} - 2\sigma_0 \delta_{t\cdot} u^n_{l,m}, \tag{4.59}$$

where $\kappa_{l,m} = \kappa(lh, mh)$ is a grid function that contains the information of the stiffness parameter distribution at each spatial grid point.

Expanding the action of the difference operators, yields

$$\begin{aligned}\frac{1}{k^2}(u_{l,m}^{n+1} - 2u_{l,m}^n + u_{l,m}^{n-1}) &= -\kappa_{l,m}^2 \frac{1}{h^4}(u_{l+2,m}^n - 4u_{l+1,m}^n + 6u_{l,m}^n - 4u_{l-1,m}^n + u_{l-2,m}^n) \\ &+ \frac{2}{h^4}(u_{l+1,m+1}^n - 2u_{l,m+1}^n + u_{l-1,m+1}^n - 2(u_{l+1,m}^n - 2u_{l,m}^n + u_{l-1,m}^n) + u_{l+1,m-1}^n - 2u_{l,m-1}^n + u_{l-1,m-1}^n) \\ &+ \frac{1}{h^4}(u_{l,m+2}^n - 4u_{l,m+1}^n + 6u_{l,m}^n - 4u_{l,m-1}^n + u_{l,m-2}^n) - 2\sigma_0 \frac{1}{2k}(u_{l,m}^{n+1} - u_{l,m}^{n-1}),\end{aligned} \tag{4.60}$$

from where the grid function values in the temporal step $n+1$ can be given in terms of its values in the previous temporal steps as

$$\begin{aligned}u_{l,m}^{n+1} = -\kappa_{l,m}^2 \frac{k^2}{h^4(k\sigma_0 + 1)} \Bigg[&(u_{l+2,m}^n - 4u_{l+1,m}^n + 6u_{l,m}^n - 4u_{l-1,m}^n + u_{l-2,m}^n) \\ &+ 2(u_{l+1,m+1}^n - 2u_{l,m+1}^n + u_{l-1,m+1}^n - 2(u_{l+1,m}^n - 2u_{l,m}^n + u_{l-1,m}^n) + u_{l+1,m-1}^n - 2u_{l,m-1}^n + u_{l-1,m-1}^n) \\ &+ (u_{l,m+2}^n - 4u_{l,m+1}^n + 6u_{l,m}^n - 4u_{l,m-1}^n + u_{l,m-2}^n) \Bigg] + \frac{2}{(k\sigma_0 + 1)} u_{l,m}^n + \frac{(k\sigma_0 - 1)}{(k\sigma_0 + 1)} u_{l,m}^{n-1}.\end{aligned} \tag{4.61}$$

When it is possible to express the next time step $n+1$ in terms of the previous ones the finite difference scheme is called to be an *explicit scheme*. On the contrary, schemes where it is not possible are known as *implicit schemes*. In this work we are going to work with explicit schemes, but, in general, other approximations of the differential equations can lead to implicit ones. Implicit schemes tend to have a better performance in terms of computational efficiency, but most of the times its implementation is more complicated.

Consistency

The prove of consistency can be done by considering a hypothetical exact solution $u^*(x, y, t)$ to the equation of motion

$$u_{tt} = -\kappa^2(x, y)\nabla^4 u - 2\sigma_0 u_t,$$

substitute it in the finite difference scheme, and compute the truncation error, τ, as the residual of this computation. The order of accuracy of each difference operator,

as obtained in a previous section, is given by

$$\begin{aligned}\delta_{\nabla^4}u^*(lh,mh,nk) &= \nabla^4 u^*(lh,mh,nk) + O(h^2),\\ \delta_{t.}u^*(lh,mh,nk) &= \frac{\partial u^*}{\partial t}(lh,mh,nk) + O(k^2),\\ \delta_{tt}u^*(lh,mh,nk) &= \frac{\partial^2 u^*}{\partial t^2}(lh,mh,nk) + O(k^2).\end{aligned} \tag{4.62}$$

As we already know this approximation error, the exact solution will approximate each differential operator in the equation of motion with the same residual, then

$$\begin{aligned}\tau &= -\kappa(lh,mh)^2\delta_{\nabla^4}u^*(lh,mh,nk) - 2\sigma_0\delta_{t.}u^*(lh,mh,nk) - \delta_{tt}u^*(lh,mh,nk)\\ &= -\kappa(lh,mh)^2\cancel{\nabla^4 u^*(lh,mh,nk)} + O(h^2) - 2\sigma_0\cancel{u_t^*(lh,mh,nk)} + O(k^2) - \cancel{u_{tt}^*(lh,mh,nk)} + O(k^2)\\ &= O(h^2) + O(k^2) \to 0, \quad \text{as} \quad h,k \to 0.\end{aligned} \tag{4.63}$$

This proves that, for any solution to the PDE, the scheme satisfies the consistency test. It also indicates that the complete scheme is of second-order accuracy in time and space.

Stability

In order to compute the stability conditions, let us express the explicit scheme (4.61) in terms of the scheme parameter

$$\mu = \kappa_{l,m}\frac{k}{h^2},$$

as

$$\begin{aligned}u_{l,m}^{n+1} =& \frac{1}{(k\sigma_0+1)}\Big[\left(2-20\mu^2\right)u_{l,m}^n + 8\mu^2(u_{l,m+1}^n + u_{l,m-1}^n + u_{l+1,m}^n + u_{l-1,m}^n)\\ &- 2\mu^2(u_{l+1,m+1}^n + u_{l+1,m-1}^n + u_{l-1,m+1}^n + u_{l-1,m-1}^n)\\ &- \mu^2(u_{l,m+2}^n + u_{l,m-2}^n + u_{l+2,m}^n + u_{l-2,m}^n)\Big] + \frac{(k\sigma_0-1)}{(k\sigma_0+1)}u_{l,m}^{n-1}.\end{aligned} \tag{4.64}$$

By replacing $u_{l,m}^n = \zeta^n e^{i(\beta_x lh+\beta_y mh)}$, we have

$$\zeta^{(n+1)}e^{i(\beta_x lh+\beta_y mh)} =$$
$$\frac{1}{(k\sigma_0+1)}\Big[\left(2-20\mu^2\right)\zeta^n e^{i(\beta_x lh+\beta_y mh)} + 8\mu^2(\zeta^n e^{i(\beta_x lh+\beta_y (m+1)h)} + \zeta^n e^{i(\beta_x lh+\beta_y (m-1)h}$$
$$+\zeta^n e^{i(\beta_x (l+1)h+\beta_y mh)} + \zeta^n e^{i(\beta_x (l-1)h+\beta_y mh)}) - 2\mu^2(\zeta^n e^{i(\beta_x (l+1)h+\beta_y (m+1)h)} + \zeta^n e^{i(\beta_x (l+1)h+\beta_y (m-1)h)}$$
$$+\zeta^n e^{i(\beta_x (l-1)h+\beta_y (m+1)h)} + \zeta^n e^{i(\beta_x (l-1)h+\beta_y (m-1)h)}) - \mu^2(\zeta^n e^{i(\beta_x lh+\beta_y (m+2)h)} + \zeta^n e^{i(\beta_x lh+\beta_y (m-2)h)}$$
$$+\zeta^n e^{i(\beta_x (l+2)h+\beta_y mh)} + \zeta^n e^{i(\beta_x (l-2)h+\beta_y mh)})\Big] + \frac{(k\sigma_0-1)}{(k\sigma_0+1)}\zeta^{(n-1)}e^{i(\beta_x lh+\beta_y mh)}. \tag{4.65}$$

Dividing by $\zeta^n e^{i(\beta_x lh+\beta_y mh)}$, yields

$$\begin{aligned}\zeta = \frac{1}{(k\sigma_0+1)}\Big[&\left(2-20\mu^2\right) + 8\mu^2(e^{i\beta_y h} + e^{-i\beta_y h} + e^{i\beta_x h} + e^{-i\beta_x h})\\ &- 2\mu^2(e^{i(\beta_x h+\beta_y h)} + e^{i(\beta_x h-\beta_y h)} + e^{i(-\beta_x h+\beta_y h)} + e^{i(-\beta_x h-\beta_y h)})\\ &- \mu^2(e^{2i\beta_y h} + e^{-2i\beta_y h} + e^{2i\beta_x h} + e^{-2i\beta_x h})\Big] + \frac{(k\sigma_0-1)}{(k\sigma_0+1)}\zeta^{-1},\end{aligned} \tag{4.66}$$

which can be expressed in terms of the variables $p_x = \sin^2(\beta_x h/2)$ and $p_y = \sin^2(\beta_y h/2)$, as the amplification polynomial

$$\zeta + \frac{1}{(k\sigma_0+1)}(16\mu^2(p_x+p_y)^2 - 2) - \frac{(k\sigma_0-1)}{(k\sigma_0+1)}\zeta^{-1} = 0. \tag{4.67}$$

For simplicity, let us consider the scheme without damping to derive the stability condition, this is $\sigma_0 = 0$. As the damped solution must decrease on magnitude, a stability condition for the scheme without damping should also be valid for scheme with $\sigma_0 > 0$. Then, the amplification polynomial with $\sigma_0 = 0$ is

$$\zeta + (16\mu^2(p_x+p_y)^2 - 2) + \zeta^{-1} = 0, \tag{4.68}$$

which is equivalent to

$$\zeta^2 + (16\mu^2(p_x+p_y)^2 - 2)\zeta + 1 = 0, \tag{4.69}$$

that has roots of the form

$$\zeta_\pm = \frac{1}{2}\left(-(16\mu^2(p_x+p_y)^2 - 2) \pm \sqrt{(16\mu^2(p_x+p_y)^2 - 2)^2 - 4}\right). \tag{4.70}$$

If $(16\mu^2(p_x+p_y)^2-2)^2-4<0$, then $\zeta_\pm=(a+ib)\in\mathbb{C}$, and therefore $|\zeta_\pm|^2=a^2+b^2$, thus

$$\begin{aligned}|\zeta_\pm|^2&=\frac{1}{4}\left((16\mu^2(p_x+p_y)^2-2)^2+(16\mu^2(p_x+p_y)^2-2)^2-4\right)\\&=\frac{1}{4}\left(2(16\mu^2(p_x+p_y)^2-2)^2-4\right).\end{aligned}\tag{4.71}$$

By imposing that $|\zeta_\pm|^2\leq 1$, we have

$$\begin{aligned}&\frac{1}{4}\left(2(16\mu^2(p_x+p_y)^2-2)^2-4\right)\leq 1\\\Rightarrow&\frac{1}{2}(16\mu^2(p_x+p_y)^2-2)^2-1\leq 1\\\Rightarrow&(16\mu^2(p_x+p_y)^2-2)^2\leq 4\\\Rightarrow&(16\mu^2(p_x+p_y)^2)^2-4(16\mu^2(p_x+p_y)^2)+4\leq 4\\\Rightarrow&(16\mu^2(p_x+p_y)^2)^2\leq 4(16\mu^2(p_x+p_y)^2),\end{aligned}\tag{4.72}$$

if $(p_x+p_y)=0$, then $\zeta_\pm=1$, which satisfy the stability condition for any value of μ, then, assuming $(p_x+p_y)\neq 0$,

$$\begin{aligned}&(16\mu^2(p_x+p_y)^2)^2\leq 4(16\mu^2(p_x+p_y)^2)\\\Rightarrow&16\mu^2(p_x+p_y)^2\leq 4\end{aligned}\tag{4.73}$$

as $\max(p_x+p_y)=2$, the condition (4.73) is satisfied when

$$\mu\leq\frac{1}{4}.\tag{4.74}$$

On the other hand, if $(16\mu^2(p_x+p_y)^2-2)^2-4\geq 0$, then $\zeta_\pm\in\mathbb{R}$, and for it to be bounded by the unity is necessary that

$$-1\leq\zeta_\pm\leq 1\tag{4.75}$$

this is,

$$-2\leq-(16\mu^2(p_x+p_y)^2-2)\pm\sqrt{(16\mu^2(p_x+p_y)^2-2)^2-4}\leq 2.\tag{4.76}$$

If $(16\mu^2(p_x+p_y)^2-2)^2-4=0$, the stability condition takes the form

$$-2\leq-(16\mu^2(p_x+p_y)^2-2)\leq 2,\tag{4.77}$$

where the inequality on the right hand side is

$$\begin{aligned}&-16\mu^2(p_x+p_y)^2+2\leq 2\\&\Rightarrow-16\mu^2(p_x+p_y)^2\leq 0\end{aligned}\tag{4.78}$$

which is always satisfy. The inequality on the left is

$$\begin{aligned} &-2 \leq -16\mu^2(p_x+p_y)^2+2 \\ &\Rightarrow 16\mu^2(p_x+p_y)^2 \leq 4 \end{aligned} \tag{4.79}$$

which leads to the same stability condition previously found, $\mu \leq 1/4$.

If $(16\mu^2(p_x+p_y)^2-2)^2-4>0$, the inequality on the right hand side is

$$\begin{aligned} &-(16\mu^2(p_x+p_y)^2-2) \pm \sqrt{(16\mu^2(p_x+p_y)^2-2)^2-4} \leq 2 \\ &\Rightarrow \pm\sqrt{(16\mu^2(p_x+p_y)^2-2)^2-4} \leq 16\mu^2(p_x+p_y)^2, \end{aligned} \tag{4.80}$$

the inequality with the minus sign is trivially satisfy because the right side is positive, thus, using the plus sign we have

$$\begin{aligned} &\sqrt{(16\mu^2(p_x+p_y)^2-2)^2-4} \leq 16\mu^2(p_x+p_y)^2 \\ &\Rightarrow (16\mu^2(p_x+p_y)^2-2)^2-4 \leq (16\mu^2(p_x+p_y)^2)^2 \\ &\Rightarrow (16\mu^2(p_x+p_y)^2)^2-4(16\mu^2(p_x+p_y)^2)+4-4 \leq (16\mu^2(p_x+p_y)^2)^2 \\ &\Rightarrow -4(16\mu^2(p_x+p_y)^2) \leq 0, \end{aligned} \tag{4.81}$$

which also is always satisfy. The inequality on the left is

$$\begin{aligned} &-2 \leq -(16\mu^2(p_x+p_y)^2-2) \pm \sqrt{(16\mu^2(p_x+p_y)^2-2)^2-4} \\ &\Rightarrow -2+(16\mu^2(p_x+p_y)^2-2) \leq \pm\sqrt{(16\mu^2(p_x+p_y)^2-2)^2-4} \\ &\Rightarrow 16\mu^2(p_x+p_y)^2-4 \leq \pm\sqrt{(16\mu^2(p_x+p_y)^2-2)^2-4} \\ &\Rightarrow 16\mu^2(p_x+p_y)^2-4 \leq \pm\sqrt{(16\mu^2(p_x+p_y)^2)^2-4(16\mu^2(p_x+p_y)^2)}. \end{aligned} \tag{4.82}$$

The inequality with the plus sign is

$$\begin{aligned} &16\mu^2(p_x+p_y)^2-4 \leq \sqrt{(16\mu^2(p_x+p_y)^2)^2-4(16\mu^2(p_x+p_y)^2)} \\ &\Rightarrow (16\mu^2(p_x+p_y)^2)^2-8(16\mu^2(p_x+p_y)^2)+16 \leq (16\mu^2(p_x+p_y)^2)^2-4(16\mu^2(p_x+p_y)^2) \\ &\Rightarrow -4(16\mu^2(p_x+p_y)^2) \leq -16 \\ &\Rightarrow 4\mu^2(p_x+p_y)^2 \geq 1 \end{aligned} \tag{4.83}$$

The inequality with the minus sign implies that

$$\begin{aligned} &16\mu^2(p_x+p_y)^2-4 \leq 0 \\ &\Rightarrow 4\mu^2(p_x+p_y)^2 \leq 1 \end{aligned} \tag{4.84}$$

in order to satisfy the last inequality in (4.83) and (4.84), $4\mu^2(p_x+p_y)^2=1$, which

can vary depending on the values of $(p_x + p_y)^2$. Therefore the condition $(16\mu^2(p_x + p_y)^2 - 2)^2 - 4 > 0$ does not lead to a stability condition.

To ensure stability, the amplification parameter ζ has to satisfy

$$\begin{aligned} (16\mu^2(p_x+p_y)^2-2)^2-4 &\leq 0 \\ \Rightarrow (16\mu^2(p_x+p_y)^2)^2-4(16\mu^2(p_x+p_y)^2)+4-4 &\leq 0 \\ \Rightarrow (16\mu^2(p_x+p_y)^2)^2 &\leq 4(16\mu^2(p_x+p_y)^2) \\ \Rightarrow 16\mu^2(p_x+p_y)^2 &\leq 4 \\ \Rightarrow 4\mu^2(p_x+p_y)^2 &\leq 1 \end{aligned} \tag{4.85}$$

which again leads to the stability condition

$$\mu \leq \frac{1}{4}, \tag{4.86}$$

which implies that

$$h \geq 2\sqrt{\kappa_{l,m}k} \quad \text{or} \quad k \leq \frac{h^2}{4\kappa_{l,m}} \tag{4.87}$$

which is satisfied for all the values of $\kappa_{l,m}$ when

$$h \geq 2\sqrt{\max_{(l,m)\in D}\{\kappa_{l,m}\}k} \tag{4.88}$$

or

$$k \leq \frac{h^2}{4\max_{(l,m)\in D}\{\kappa_{l,m}\}}. \tag{4.89}$$

The condition (4.88) can be used to compute the minimum spatial grid size h when a certain time definition k is required. On the other hand, condition (4.89) can be employ to compute the maximum time step size k for a given spatial resolution h.

Numerical boundary conditions

The boundary condition for a clamped plate, having its mid-plane represented by Ω, are given by

$$0 = u = u_{\mathbf{n}} = \nabla u \cdot \mathbf{n} \quad \text{on} \quad \partial\Omega, \tag{4.90}$$

where $\mathbf{n}$ represent the outer normal vector on the boundary.

The condition $u = 0$ in the boundary is easy given by making the gird function equal to zero in the corresponding points of the discrete domain.

For a rectangular plate the outer normal vector can be e_x or e_y depending on to which axes is the boundary line aligned to. Then $u_{\mathbf{n}} = \partial u/\partial x$ or $u_{\mathbf{n}} = \partial u/\partial y$.

In the case of a rectangular plate placed with one corner on the origin and place in the positive (x, y) plane one boundary is placed in the line $x = 0$. Taking the finite difference approximation for $\partial/\partial x$ as δ_{x+} and evaluating in the boundary ($l = 0$), we have that

$$\frac{u^n_{0+1,m} - u^n_{0,m}}{h} = 0 \Rightarrow u^n_{1,m} = u^n_{0,m} \tag{4.91}$$

therefore the boundary condition (4.90) is satisfied if

$$u^n_{1,m} = u^n_{0,m} = 0 \tag{4.92}$$

for all m.

We are going to approximate the solution for a circular plate by solving the equation of motion in a circular domain inscribed in a square domain placed in the positive (x, y) plane, by applying the adequate conditions at the grid points on the boundary and outside of the circle. For a circular plate, the outer normal vector is the radial normal vector $\hat{r}$, then

$$u_{\mathbf{n}} = \nabla u \cdot \hat{r}. \tag{4.93}$$

Therefore, the boundary condition $\nabla u \cdot \hat{r} = 0$ is given by $\nabla u = 0$, which can be approximated as

$$(\delta_{x\pm} u^n_{l,m}, \delta_{y\pm} u^n_{l,m}) = (0, 0), \tag{4.94}$$

where the sign in the discrete derivative depends on the orientation of the grid point.

The way we used to implement this approximation consists in making zero the value of the grid function in the boundary as well as its proximate neighbour. This is done by creating a *boundary matrix*, $B_{l,m}$, given by

$$B_{l,m} = \begin{cases} 1, & \text{if } \sqrt{(l - \frac{Nx-1}{2})^2 + (m - \frac{Nx-1}{2})^2} \leq \frac{(Nx-5)}{2}, \\ 0, & \text{otherwise,} \end{cases} \tag{4.95}$$

which means that the boundary matrix has a value of 1 if the grid point is inside the circle and 0 if it is outside. In figure 4.1 the behaviour of the boundary matrix with respect to the number of sub-divisions in the x direction N_x is illustrated.

At each time step, the grid function is computed according to (4.61) in the complete square domain, and before the update the grid function is multiplied by the boundary matrix. This implementation of the boundary conditions was tested to approximate the eigen-frequencies of the homogeneous clamped plate that were obtained in section 3.2.4, showing a reasonably good approximation for sufficiently large N_x. These results are shown in section 6.5. This method also has the advantage that it can be used to approximate the clamped plate vibrations of potentially any two-dimensional shape.

An implementation of circular boundary conditions in Cartesian coordinates is reported as the *staircase approximation* in [Bilbao, 2012]. The fixed boundary case is addressed in a very similar way as the method proposed in this section.

Initial conditions

The initial conditions of position $u(x, y, t = 0) = u_0(x, y)$ and velocity $u_t(x, y, t = 0) = v_0(x, y)$ has to be defined in order to initialise the finite difference scheme. The grid function at the time step $n - 1$ is given by the initial position, and the value at the time step n as the initial position plus the time step, k, times the initial velocity.

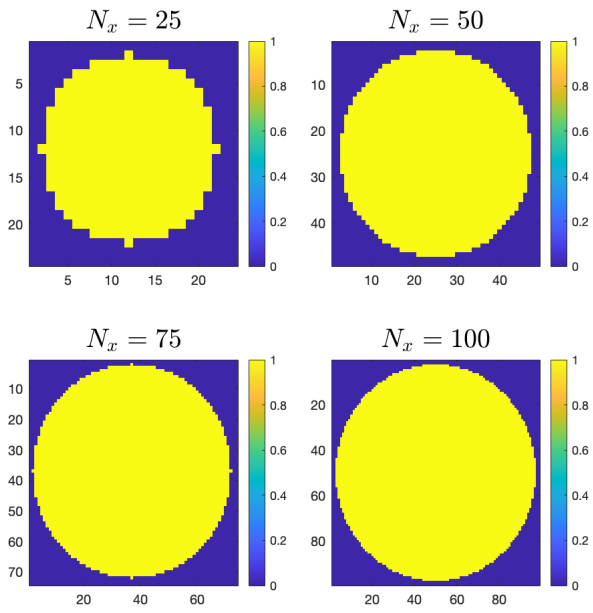

Figure 4.1: Behaviour of the boundary matrix with respect to the number of sub-divisions in the x direction N_x. In this case $N_x = N_y$ as the domain is a perfect square, and the spatial grid size $h = 1/N_x$ is equal in both directions.

This is,

$$\begin{aligned} u_{l,m}^{n-1} &= u_0(lh, mh), \\ u_{l,m}^{n} &= u_0(lh, mh) + k \cdot v_0(lh, mh). \end{aligned} \tag{4.96}$$

In this way, the next time step, $n+1$, can be computed using (4.61). In order for the problem (4.56) to be well posed, the initial conditions has to satisfy the same boundary conditions as u. For example, to simulate a resting plate that is stimulated by an external force in a determined region the initial conditions can be taken as

$$u_0(x, y) = 0, \quad \text{for all} \quad (x, y) \in \Omega \tag{4.97}$$

and

$$v_0(x, y) = \begin{cases} c_0\big(1 + \cos(\pi\sqrt{(x-x_0)^2 + (y-y_0)^2}/r_w\big), & \text{if} \quad \sqrt{(x-x_0)^2 + (y-y_0)^2} \leq r_w \\ 0, \quad \text{if} \quad \sqrt{(x-x_0)^2 + (y-y_0)^2} > r_w, \end{cases} \tag{4.98}$$

this is, the initial position is 0 all around the plate and the initial velocity has a rising cosine shape of width r_w centred at (x_0, y_0), with height c_0.

For both, polar and Cartesian coordinates, the initial conditions behave in a similar way. In this section, the initial conditions implementation was explained in Cartesian coordinates, but everything explained here is applicable to the Polar scheme, only by transforming the functions u_0 and v_0 to its equivalents in polar coordinates

to define the grid functions as in (4.96)

4.5.2 Polar coordinates

As mentioned before, the finite difference scheme in polar coordinates that was employed to approximate the equation of motion was found parting from the explicit version of the scheme proposed in [Bilbao, 2009] (section 12.6), but modifying it significantly.

In this section, this scheme is described, but the prove of convergence is given by the numerical results in section (6.5).

Finite difference scheme

To approximate the equation of motion, we are going to use a auxiliary grid function $v_{l,m}$ defined over the same discrete domain as $u^n_{l,m}$. Given the initial conditions $u^{n-1}_{l,m}$ and $u^n_{l,m}$ as mentioned before, the first step is to compute

$$v_{l,m} = \delta_{\nabla^2 \circ} u^n_{l,m} \tag{4.99}$$

for $l \in (1, N_r - 1)$ and $m \in (0, N_\theta - 1)$. To obtain the boundary condition for $l = N_r$, consider the equation

$$v = \nabla^2 u = \frac{\partial^2 u}{\partial r^2} + \frac{1}{r}\frac{\partial u}{\partial r} + \frac{1}{r^2}\frac{\partial^2 u}{\partial \theta^2} \tag{4.100}$$

evaluated in the boundary. As

$$u = \frac{\partial u}{\partial r} = 0 \tag{4.101}$$

on $\partial\Omega$, then

$$\frac{\partial^2 u}{\partial \theta^2}|_{\partial\Omega} = 0, \tag{4.102}$$

and therefore the value of $v_{N_r,m}$ could be computed as

$$v_{N_r,m} = \delta_{rr} u^n_{N_r,m}, \tag{4.103}$$

but $\delta_{rr} u^n_{N_r,m}$ requires the value $u^n_{N_r+1,m}$, that is out of the domain, to be computed. The way to overcome this is by applying again the boundary condition of the redial derivative to obtain the value needed in terms of grid points inside the domain, this is

$$\delta_{r\cdot} u^n_{N_r,m} = \frac{1}{2h_r}(u^n_{N_r+1,m} - u^n_{N_r-1,m}) = 0 \Rightarrow u^n_{N_r+1,m} = u^n_{N_r-1,m}. \tag{4.104}$$

In this way, the value on the boundary is given by

$$v_{N_r,m} = \frac{1}{h_r^2}(u^n_{N_r+1,m} - 2u^n_{N_r,m} + u^n_{N_r-1,m}) = \frac{1}{h_r^2}(2u^n_{N_r-1,m}), \tag{4.105}$$

where we used also that $u^n_{N_r,m} = 0$ for all m and n.

The value on the central point $l = 0$ is given by

$$v_{0,m} = \delta_{\nabla^2 \circ} u^n_{0,0} = \frac{4}{N_\theta h_r^2} \sum_{m=0}^{N_\theta - 1} (u^n_{1,m} - u^n_{0,0}). \tag{4.106}$$

What is left now is to compute $u^{n+1}_{l,m}$ with the complete scheme for the equation of motion. In the interior points $l \in (1, N_r - 1)$ is computed as

$$u^{n+1}_{l,m} = -\kappa^2_{l,m} \frac{k^2}{(k\sigma_0 + 1)} \delta_{\nabla^2 \circ} v_{l,m} + \frac{2}{(k\sigma_0 + 1)} u^n_{l,m} + \frac{(k\sigma_0 - 1)}{(k\sigma_0 + 1)} u^{n-1}_{l,m}, \tag{4.107}$$

on the boundary $l = N_r$ is set to be

$$u^{n+1}_{N_r,m} = 0 \tag{4.108}$$

for all n and m, and in the central point is computed as

$$\begin{aligned} u^{n+1}_{0,m} &= -\kappa^2_{l,m} \frac{k^2}{(k\sigma_0 + 1)} \delta_{\nabla^2 \circ} v_{0,0} + \frac{2}{(k\sigma_0 + 1)} u^n_{l,m} + \frac{(k\sigma_0 - 1)}{(k\sigma_0 + 1)} u^{n-1}_{l,m} \\ &= -\kappa^2_{l,m} \frac{k^2}{(k\sigma_0 + 1)} \frac{4}{N_\theta h_r^2} \sum_{m=0}^{N_\theta - 1} (v_{1,m} - v_{0,0}) + \frac{2}{(k\sigma_0 + 1)} u^n_{l,m} + \frac{(k\sigma_0 - 1)}{(k\sigma_0 + 1)} u^{n-1}_{l,m}. \end{aligned} \tag{4.109}$$

This procedure showed to be stable by applying the stability condition presented in [Bilbao, 2009] for the scheme in section 12.6 with free centre condition, given for a variable stiffness coefficient by

$$k \leq \left(\frac{1}{1 + \frac{1}{h_\theta^2}} \right) \frac{h_r^2}{2 \max_{(l,m) \in D} \{\kappa_{l,m}\}}. \tag{4.110}$$

The fact that they share the same stability condition could make us believe that the schemes are somehow equivalent, but they are fundamentally different schemes. The most notable difference is that the explicit version of the scheme proposed in Bilbao's book uses an approximation to the biharmonic operator that makes the grid function to have same value at $u^n_{1,m}$ $(l = 1)$ as well as at $u^n_{0,m}$ $(l = 0)$, for all m, at each time step n. In contrast, the scheme we developed only requires that the grid function have the same value in the centre point $u^n_{0,m}$, for all m, at each time step n, given by the approximation of the Laplacian difference operator at the centre point, whereas the value of $u^n_{1,m}$ can vary with respect to m.

The relationship between this schemes as well as the analytic proofs of stability and consistency of the scheme proposed here are going to be left as future work. The computational proof of consistency and stability will be enough to obtain results.

Chapter 5

Metrics

In this chapter we introduce the metrics of interest to be obtained from the numerical simulations, which are: the *harmonicity* and the *quality factor*. The harmonicity metrics were inspired by the definition given in [Sathej and Adhikari, 2009], and the quality factor description and measurement procedure was consulted fundamentally in [Heinrich and Dufour, 2015].

5.1 Harmonicity

When dealing with periodic vibrating phenomenons, it is usual to analyse them by decomposing the signals in their simple wave components, by applying the Fourier Transform or the FFT when the data is given computationally. Each of these components has a characteristic frequency of vibration. The lowest frequency of vibration is known as the *fundamental frequency*, and the higher frequencies are known as *overtones*. The concept of harmonicity of a vibrating body is defined as the proximity of the overtones or higher order frequencies to the integer multiples of the fundamental frequency. This concept is usually employ in musical acoustics to characterise the sound produced by an instrument. Inspired in the work of Sathej, G. and Adhikari, R.[Sathej and Adhikari, 2009], we measure the harmonicity in two ways. The first one is given by the *harmonicity quality function*

$$Q_{\mathrm{h}} = \sum_i (f_i - h_i)^2, \tag{5.1}$$

where h_i represents the closer multiple of the fundamental frequency f_0 to f_i. The second one, called *rounded harmonocity quality function*, is given by

$$Q_{\mathrm{rh}} = \sum_i (\frac{f_i}{f_0} - \left[\frac{f_i}{f_0}\right])^2 \tag{5.2}$$

where $[x]$ represents the rounded value of x. The rounded harmonicity metric was implemented to incorporate the case when the measured frequency of the n-th mode is closer to the $n-1$ or $n+1$-th (or other) multiple harmonic of the fundamental

frequency. Both quality functions indicate a higher harmonicity when their value is minimised.

5.2 Quality factor of a oscillator

The quality factor or Q-factor is a dimensionless parameter that describes how underdamped an oscillator or resonator is. It has many definitions, but it can be looked as the ratio of the initial energy stored in a resonator to the energy lost in one radian of the cycle of oscillation [Hickman, 2013]. Higher Q indicates a lower rate of energy loss and the oscillator die out more slowly or has the capability to vibrate at higher frequencies for longer times. "One may view high-Q systems as exhibiting more energy-efficient free vibrations" [Heinrich and Dufour, 2015].

5.2.1 Quality factor of a free vibrating oscillator

The fundamental definition of the quality factor, as explained in [Heinrich and Dufour, 2015], comes from the equation of motion of a single-degreeof-freedom (SDOF) damped oscillator subjected to a external force

$$m\ddot{u}(t) + c\dot{u}(t) + ku(t) = F(t), \tag{5.3}$$

where m, c, and k represent, respectively, the effective mass, effective damping coefficient, and effective stiffness of the system, $F(t)$ is the time-dependent external force, and $u(t)$ is the displacement response of the SDOF oscillator. This system can also be understood as a linear spring-mass damped oscillator.

We can write the solution of the homogeneous case (with $F(t) \equiv 0$) as

$$u_0(t) = e^{-\zeta\omega_0 t}(A\cos\omega_d t + B\sin\omega_d t) \tag{5.4}$$

where the *undamped natural frequency*, ω_0, and the *damping ratio*, ζ, are given by

$$\omega_0 = \sqrt{\frac{k}{m}}, \tag{5.5}$$

$$\zeta = \frac{c}{2\sqrt{km}}, \tag{5.6}$$

and the *damped natural frequency*, is defined as

$$\omega_d = \omega_0\sqrt{1-\zeta^2}. \tag{5.7}$$

The physical meaning of ω_d is that it represents the frequency of oscillation (in radians per second) of the free vibration of the damped SDOF. Note that the damped natural frequency is less than its undamped counterpart; however, for small-to-moderate values of the damping ratio (ζ less than, say, 0.2), the damped natural frequency is

approximately the same as the undamped natural frequency, this is,

$$\omega_d \approx \omega_0 = \sqrt{k/m}. \tag{5.8}$$

This shows that the damping ratio ζ is a quantity that characterises the energy dissipation inherent in the SDOF. An alternative way to make such a characterisation, is to define the quality factor, Q, in terms of the damping ratio as follows

$$Q = \frac{1}{2\zeta} = \frac{\sqrt{km}}{c}. \tag{5.9}$$

An approximate rule-of-thumb is that a damping ratio of 10% ($Q = 5$) corresponds to roughly a 50% decrease in amplitude over one complete cycle of free vibration.

5.2.2 Quality factor of a harmonically forced vibrating oscillator

Consider now a harmonic force with amplitude F_0 and frequency ω, given by

$$F(t) = F_0 \sin \omega t, \tag{5.10}$$

and write the solution as

$$u(t) = \frac{F_0}{k} D(r, \zeta) \sin[\omega t - \theta(r, \zeta)], \tag{5.11}$$

where

$$D(r, \zeta) = \frac{1}{\sqrt{(1 - r^2)^2 + (2\zeta r)^2}}, \tag{5.12}$$

$$\theta(r, \zeta) = \arctan\left(\frac{2\zeta r}{1 - r^2}\right) \in [0, 2\pi], \tag{5.13}$$

$$r = \frac{\omega}{\omega_0}. \tag{5.14}$$

The coefficient F_0/k in equation (5.11) represents the quasi-static displacement amplitude that the system would experience if the force were applied at extremely low frequencies ($0 < \omega << 1$); hence the quantity D appearing in is simply the ratio of the dynamic displacement amplitude ($u_{\max}$) to the quasi-static amplitude (F_0/k) and is therefore referred to as the *dynamic magnification factor*. The quantity θ represents the angle by which the displacement response lags the actuation force; it is therefore called the *lag angle* of the displacement with respect to the applied force. Both D and θ depend on r and θ, the former being the *frequency ratio*.

Thus, the resonant frequency, ω_{res}, i.e., the actuation frequency that causes maximum displacement response, is obtained by maximising (5.12) with respect to r. In this way,

$$r_{\text{res}} = \sqrt{1 - 2\zeta^2}, \tag{5.15}$$

$$\omega_{\text{res}} = \omega_0\sqrt{1-2\zeta^2} \tag{5.16}$$

and

$$D_{\max} = \frac{1}{2\zeta\sqrt{1-\zeta^2}}. \tag{5.17}$$

Thus, the resonant frequency is less than ω_d, which is less than ω_0. For an undamped system ($c = \zeta = 0$), the displacement amplitude is theoretically infinite and occurs at $r = 1$, or when the forcing frequency coincides with the undamped natural frequency. When the effects of damping are included, $D_{\max}$ occurs at $r < 1$; however, when $\zeta \leq 0.2$ ($Q \geq 2.5$), $D_{\max}$ occurs very close to $r = 1$, in which case $D_{\max}$ may be accurately estimated as

$$D_{\max} \approx D|_{r=1} = \frac{1}{2\zeta} = Q. \tag{5.18}$$

Equation (5.18) indicates that, in theory, for small-to-moderate damping, the value of Q may be extracted from an experimentally generated plot of D versus exciting frequency. This method is known as the "resonant amplification method". However, in practice it may be difficult to experimentally determine the quasi-static scaling factor F_0/k, that is, the low-frequency limit for the displacement amplitude, which is needed to relate the measured displacement amplitude to D. This limitation is usually overcome by employing the *half-power method* or *-3 dB bandwidth method* in MEMS/NEMS applications. Before going into the details of this method, let us study Q with a energy-based definition in a SDOF.

5.2.3 Quality factor definition based on the energy ratio

By understanding the system as a spring-mass oscillator, a common definition employed for the quality factor of a resonator is based on a ratio of energies when the resonator is excited harmonically at its undamped natural frequency, given by

$$Q_E = 2\pi\frac{U_{\max}}{\Delta W}|_{r=1} \tag{5.19}$$

where $U_{\max}$ is the maximum elastic energy (stored in the spring) and ΔW is the dissipated energy per cycle of steady-state vibration.

Using (5.11), we have

$$U_{\max} = \frac{1}{2}ku_{\max}^2 = \frac{1}{2}k[\frac{F_0}{k}D(r,\zeta)]^2 = \frac{F_0}{2k}[D(r,\zeta)]^2, \tag{5.20}$$

and knowing that the energy dissipated must be the same as the work done by the applied force over one cycle, we have that

$$\Delta W = \int_0^{2\pi} F(t)\dot{u}(t)dt = \frac{2\pi\zeta r F_0^2[D(r,\zeta)]^2}{k}. \tag{5.21}$$

Therefore,

$$Q_E = 2\pi \frac{U_{\max}}{\Delta W}|_{r=1} = \frac{1}{2\zeta r}|_{r=1} = \frac{1}{2\zeta} = \frac{\sqrt{km}}{c}, \tag{5.22}$$

which means that the energy-based definition of the quality factor (Q_E) is equivalent to the property-based definition in equation (5.9).

5.2.4 Experimental measurement of the quality factor

The previous definitions of Q are the theoretical motivations, inspired by SDOF models. In practice, the systems are more complicated, most dynamic systems have the potential to respond in a manner that requires a multiple-degree-of-freedom (MDOF) description in order to capture multiple "modes" of vibration that may occur, including the possible interaction of these modes during a free or forced vibration. A common experimental method used to measure Q in MEMS/NEMS resonators (and in other resonating structures) is the *bandwidth method*, also known as the *-3 dB bandwidth method* or the *half-power method*. This method is based on taking advantage of the Q-dependence of the shape of the *frequency response functions* (FRF) for the response amplitude in a neighbourhood of the resonant peak. In the SDOF model with forced vibration, this resonant phenomenon is shown by using as FRF the dynamic amplification factor D, defined in (5.12). However, for more complex behaviours, the FRF may be for the displacement amplitude or any output signal "R" that is proportional to the displacement amplitude. Having experimentally determined the shape of the resonant peak, the value of the quality factor Q_w may be estimated by the formula

$$Q_w = \frac{\omega_{\text{res}}}{\Delta\omega} = \frac{f_{\text{res}}}{\Delta f} \approx Q, \tag{5.23}$$

in which ω_{res} is the resonant frequency (defined by the peak response value $R_{\max}$ of the FRF), $\Delta\omega = \omega_2 - \omega_1$ is the frequency bandwidth and ω_1 and ω_2 are the frequencies corresponding to a response value of $R_{\max}/\sqrt{2}$. Analogous definitions apply to the f quantities in (5.23) for the common case in which frequency values are plotted in hertz, kilohertz, and so on.

In the next chapter we will apply the bandwidth method to measure the quality factor of the numerical simulations of the vibrating loaded-damped plate.

Chapter 6

Numerical Experiments and results

6.1 Introduction

The numerical experiments performed with the finite difference schemes of the initial-boundary value problem for the loaded plate described in the previous chapter, were made in order to understand the vibrating behaviour of a microscopic circular polymer plate loaded with a circular concentric metallic cover, following the variable-density model explained in section 3.3.1. In particular, the experiments were made to address two questions:

1. Can the *harmonicity* of vibration modes in an elastic circular plate made of polymer be improved by loading it with concentric circles of metallic material?
2. Can the *quality factor* of plate vibrations be improved through the same loading procedure?

Two sets of comparable experiments were designed in order to answer each question. At each experiment set, the space of parameters of the diameter and thickness of the metallic loading was explored. For each experimental design, a specific measurement type needs to be made to answer each question.

In this chapter, the details of the numerical schemes and measurement procedures will be explained. Then, the numerical consistency proof of the Cartesian and polar coordinates schemes is performed, and a comparative study between both schemes is shown. Finally, the experiments to measure *harmonicity* and the *quality factor* are explained, and the parameters space exploration performed to answer each question is presented.

6.2 Numerical scaling and numerical decay time

The finite different schemes in both Cartesian and polar coordinates need to be scaled to approximate in a better way the spacial and time dimensions of the microscopic loaded plate system.

6.2.1 Spacial scaling

The spacial scaling is performed by defining a scaled coordinate system given by

$$(x^*, y^*) = \left(\frac{x}{Di_{\text{ext}}}, \frac{y}{Di_{\text{ext}}}\right), \quad \text{or} \quad (r^*, \theta) = (\frac{r}{R_{\text{ext}}}, \theta), \tag{6.1}$$

where (x, y) and (r, θ) represents the original system where the actual physical magnitude of the plate is defined, and the characteristic scaling factor is given by the polymer plate's diameter Di_{ext} in Cartesian coordinates, and by the plate's radius R_{ext} in polar coordinates. In this way, the actual magnitude of the plate is replaced by the unity and the grid spacings $h = 1/N_x$ and $h_r = 1/N_r$ are unit-less fractions of the unit interval. Both of these spacings can be doted with units by multiplying them by the corresponding scale factor.

To understand the effect of this scaling, consider the equation of motion defined over Ω using the spatial coordinates without scaling,

$$u_{tt}(\bar{x}, t) = -\kappa^2(\bar{x})\nabla^4 u(\bar{x}, t) - 2\sigma_0 u_t(\bar{x}, t), \quad \text{for} \quad \bar{x} \in \Omega,\, t > 0, \tag{6.2}$$

with $\bar{x} = (x, y)$ or (r, θ), depending on the coordinate system that is been used, and the space dependant stiffness parameter is

$$\kappa^2(\bar{x}) = \frac{D(\bar{x})}{\rho(\bar{x})H(\bar{x})}, \tag{6.3}$$

where D is the flexural rigidity, ρ is the density and H is the plate's thickness.

The spatial derivatives with respect to the scaled coordinates can be obtained in terms of the coordinates without scaling by applying the chain rule as follows

$$\begin{aligned}
\frac{\partial u}{\partial x^*} &= \frac{\partial u}{\partial x}\frac{\partial x}{\partial x^*} = Di_{\text{ext}}\frac{\partial u}{\partial x}, \\
\frac{\partial u}{\partial y^*} &= \frac{\partial u}{\partial y}\frac{\partial y}{\partial y^*} = Di_{\text{ext}}\frac{\partial u}{\partial r}, \\
\frac{\partial u}{\partial r^*} &= \frac{\partial u}{\partial r}\frac{\partial r}{\partial r^*} = R_{\text{ext}}\frac{\partial u}{\partial r}.
\end{aligned} \tag{6.4}$$

Then, the biharmonic operator in the scaled Cartesian coordinates is

$$\nabla^{*4} = \frac{\partial^4}{\partial x^{*4}} + 2\frac{\partial^4}{\partial x^{*2}\partial y^{*2}} + \frac{\partial^4}{\partial y^{*4}} = Di_{\text{ext}}^4\left[\frac{\partial^4}{\partial x^4} + 2\frac{\partial^4}{\partial x^2\partial y^2} + \frac{\partial^4}{\partial y^4}\right] = Di_{\text{ext}}^4\nabla^4. \tag{6.5}$$

The scaling factor of the biharmonic operator in polar coordinates can be obtain by analysing the Laplacian operator, given by

$$\nabla^{*2}\circ = \frac{\partial^2}{\partial r^{*2}} + \frac{1}{r^*}\frac{\partial}{\partial r^*} + \frac{1}{r^{*2}}\frac{\partial^2}{\partial\theta^2} = R_{\text{ext}}^2\frac{\partial^2}{\partial r} + R_{\text{ext}}^2\frac{1}{r}\frac{\partial}{\partial r} + R_{\text{ext}}^2\frac{1}{r^2}\frac{\partial^2}{\partial\theta^2} = R_{\text{ext}}^2\nabla^2\circ. \tag{6.6}$$

As the biharmonic operator in polar coordinates is

$$\nabla^4 \circ = \nabla^2 \circ \nabla^2 \circ, \tag{6.7}$$

then, it also satisfies that

$$\nabla^{*4} \circ = \nabla^{*2} \circ \nabla^{*2} \circ = R_{\text{ext}}^4 \nabla^2 \circ \nabla^2 \circ = R_{\text{ext}}^4 \nabla^4 \circ . \tag{6.8}$$

Therefore, the scaled coordinate equation of motion is given by

$$u_{tt}(\bar{x}^*, t) = -\kappa^{*2}(\bar{x}^*)\nabla^{*4} u(\bar{x}^*, t) - 2\sigma_0 u_t(\bar{x}^*, t), \quad \text{for} \quad \bar{x} \in \Omega^*,\, t > 0, \tag{6.9}$$

with Ω^* the domain in the scaled coordinates, and

$$\kappa^{*2}(\bar{x}^*) = \frac{D(\bar{x}^*)}{\rho(\bar{x}^*)H(\bar{x}^*)L^4}, \tag{6.10}$$

where $L = Di_{\text{ext}}$ in Cartesian coordinates, and $L = R_{\text{ext}}$ in polar coordinates.

The supper asterisk can be removed to write the initial-boundary value problem as previously in (4.56). In this way, the finite difference schemes presented before inherits the same scaled coordinates.

6.2.2 Time scaling

Proceeding as before, let us define a scaled time coordinate

$$t^* = \sigma t, \tag{6.11}$$

where $\sigma \in \mathbb{R}^+$ is the scaling constant. For example if t is defined in seconds, and $\sigma = 10^{-6}$ then t^* is given in $10^{-6}\text{s} = \mu\text{s}$. In this way,

$$\frac{\partial u}{\partial t^*} = \frac{\partial u}{\partial t}\frac{\partial t}{\partial t^*} = \frac{1}{\sigma}\frac{\partial u}{\partial t}. \tag{6.12}$$

Notice that the units of the damping parameter are

$$[\sigma_0] = \frac{1}{\text{time}}, \tag{6.13}$$

therefore, defining $\sigma_0^* = \frac{1}{\sigma}\sigma_0$, we have that the time-scaled equation of motion is

$$\sigma^2 u_{t^*t^*}(\bar{x}, t^*) = -\kappa^2(\bar{x})\nabla^4 u(\bar{x}, t^*) - 2\sigma^2\sigma_0^* u_t^*(\bar{x}, t^*), \tag{6.14}$$

which implies that

$$u_{t^*t^*}(\bar{x}, t^*) = -\kappa^{*2}(\bar{x})\nabla^4 u(\bar{x}, t^*) - 2\sigma_0^* u_t^*(\bar{x}, t^*), \tag{6.15}$$

where

$$\kappa^{*2} = \frac{\kappa^2}{\sigma^2}, \tag{6.16}$$

in this way, the time scaling factor can also be control by scaling only the stiffness parameter.

In order to understand the units involved in the scheme, let us analyse the units of the flexural rigidity D and of the stiffness parameter κ, given by

$$[D] = [E \cdot H^3] = \frac{\text{mass}}{\text{distance} \cdot \text{time}^2} \cdot \text{distance}^3 = \frac{\text{mass} \cdot \text{distance}^2}{\text{time}^2}, \tag{6.17}$$

and

$$[\kappa^2] = \left[\frac{D}{\rho H L^4}\right] = \frac{\text{mass} \cdot \text{distance}^2}{\text{time}^2 \cdot \frac{\text{mass}}{\text{distance}^3} \cdot \text{distance} \cdot \text{distance}^4} = \frac{1}{\text{time}^2}, \tag{6.18}$$

which means that

$$[\kappa] = \frac{1}{\text{time}}.$$

The frequency of the first modes of vibration of a clamped plate with a radius in the order of micrometers will be of the order of hundreds of kilohertz and in the megahertz for higher order modes. Therefore it is computationally reasonable to scale the time units. The time-scaling procedure done before is equivalent to define a special unit of time σ, for example

$$\sigma = 10^{-6}\text{s}, \tag{6.19}$$

then

$$\text{s} = 10^6\sigma \Rightarrow \text{s}^2 = 10^{12}\sigma^2. \tag{6.20}$$

Therefore, the units of the Young's modulus, expressed in terms of σ, are

$$[E] = \frac{\text{Kg}}{\text{m} \cdot \text{s}^2} = 10^{-12}\frac{\text{Kg}}{m \cdot \sigma^2}. \tag{6.21}$$

In this way, the units of the stiffness parameter are

$$[\kappa] = \frac{1}{\sigma}.$$

Applying the stability condition for Cartesian coordinates with the equal sign, which is the way we are going to use it, leads to

$$k = \frac{h^2}{4\max_{(l,m)\in D}\{\kappa_{l,m}\}}, \tag{6.22}$$

or, in polar coordinates

$$k = \left(\frac{1}{1 + \frac{1}{h_\theta^2}} \right) \frac{h_r^2}{2 \max_{(l,m)\in D}\{\kappa_{l,m}\}}. \tag{6.23}$$

This implies that the unis of the discrete time step has to be

$$[k] = \sigma = 10^{-6}\text{s},$$

because the discrete spatial step is dimensionless due of the scaling made in the differential equation (and therefore in the finite difference scheme). In this way, units of the the frequency will be

$$[f] = \frac{1}{10^{-6}\text{s}} = 10^6 \frac{1}{\text{s}} = \text{MHz}. \tag{6.24}$$

This condition has to be taken into account when performing the Fast Fourier Transform (FFT) to obtain results.

6.2.3 Numerical decay time

As shown in section 3.3.2, the damping term introduced in the equation of motion forces that any bounded solution, $w(\bar{x}, t)$, to decrease exponentially as

$$|w(\bar{x}, t)| \leq Ce^{-\sigma_0 t}, \tag{6.25}$$

for a constant $C > 0$, for all $t > 0$ and for all $\bar{x} \in \mathbb{R}^2$.

The time and size of the amplitude reduction can be controlled by varying the value of σ_0. The 60dB decay time T_{60} is define as the time it takes to a oscillator to reduce its amplitude by 60dB or 10^6 times, and is defined as

$$T_{60} = \frac{6\ln(10)}{\sigma_0}. \tag{6.26}$$

By substituting

$$\sigma_0 = \frac{6\ln(10)}{T_{60}} \tag{6.27}$$

in $Ce^{-\sigma_0 t}$, we have that when $t = T_{60}$

$$Ce^{-\sigma_0 T_{60}} = Ce^{6\ln(10)} = C \cdot 10^{-6}.$$

This implies that at the time $t = T_{60}$ the reduction of amplitude is of the order of 10^6. This decay time will be used in the numerical experiment to measure the quality factor of the loaded plate, as it ensures that the damping has reduced the amplitude significantly during the experiment duration. The units of this decay time are given by the time scaling parameter σ.

6.3 Loading

In the variable-density model the loaded region of the plate is completely determined by the stiffness parameter distribution,

$$\kappa^2(r) = \begin{cases} \kappa_{\text{int}} = \frac{D_T}{\rho_T h_T L^4}, & \text{if} \quad 0 \leq r < R_{\text{int}}, \\ \kappa_{\text{ext}} = \frac{D_1}{\rho_1 h_1 L^4}, & \text{if} \quad R_{\text{int}} \leq r \leq R_{\text{ext}}, \end{cases} \tag{6.28}$$

where κ_{int} and κ_{ext} are the internal and external value of the stiffness parameter.

In both, the Cartesian and the polar finite difference schemes, the information of this distribution is stored in the stiffness parameter matrix $\kappa_{l,m}$, but the definition of this matrix is different for each scheme. The main difference comes from a numerical result that shown certain instability in the Cartesian schemes while dealing with pronounced changes of density. In part this is the motivation to perform two numerical procedures (the Cartesian and Polar schemes) to verify the results.

6.3.1 Polar coordinates

In polar coordinates the stiffness parameter matrix is taken as the step function (6.28) taking the grid radial coordinate $r = lh_r$ and spatial scaling factor $L = R_{\text{ext}}$. Figure 6.1 illustrates the behaviour of the stiffness parameter distribution as a function of the internal diameter Di_{int} and the internal thickness H_{int}. The distribution is defined over a plate of 150 μm diameter and 15 μm of thickness, using a time scaling factor $\sigma = 10^{-6}$s. The internal diameter and thickness are expressed as a percentage of the corresponding feature of the complete plate, i.e., the internal diameter is expressed as a percentage of the plate's diameter and the internal thickness as a percentage of the plate's thickness without loading.

The unloaded part has the elastic values of the CYTOP[1] polymer, which are:

$$\begin{aligned} E_{\text{CYTOP}} &= 7.9 \times 10^9 \text{Kg}/(\text{ms}^2), \\ \rho_{\text{CYTOP}} &= 2.03 \times 10^3 \text{Kg}/(\text{m}^3), \\ \nu_{\text{CYTOP}} &= 0.42, \end{aligned} \tag{6.29}$$

and the loaded region uses the elastic values of the gold, given by

$$\begin{aligned} E_{\text{Au}} &= 79 \times 10^9 \text{Kg}/(\text{ms}^2), \\ \rho_{\text{Au}} &= 19.3 \times 10^3 \text{Kg}/(\text{m}^3), \\ \nu_{\text{Au}} &= 0.4. \end{aligned} \tag{6.30}$$

[1]See [AGC-chemicals, 2018], for more information of this polymer material.

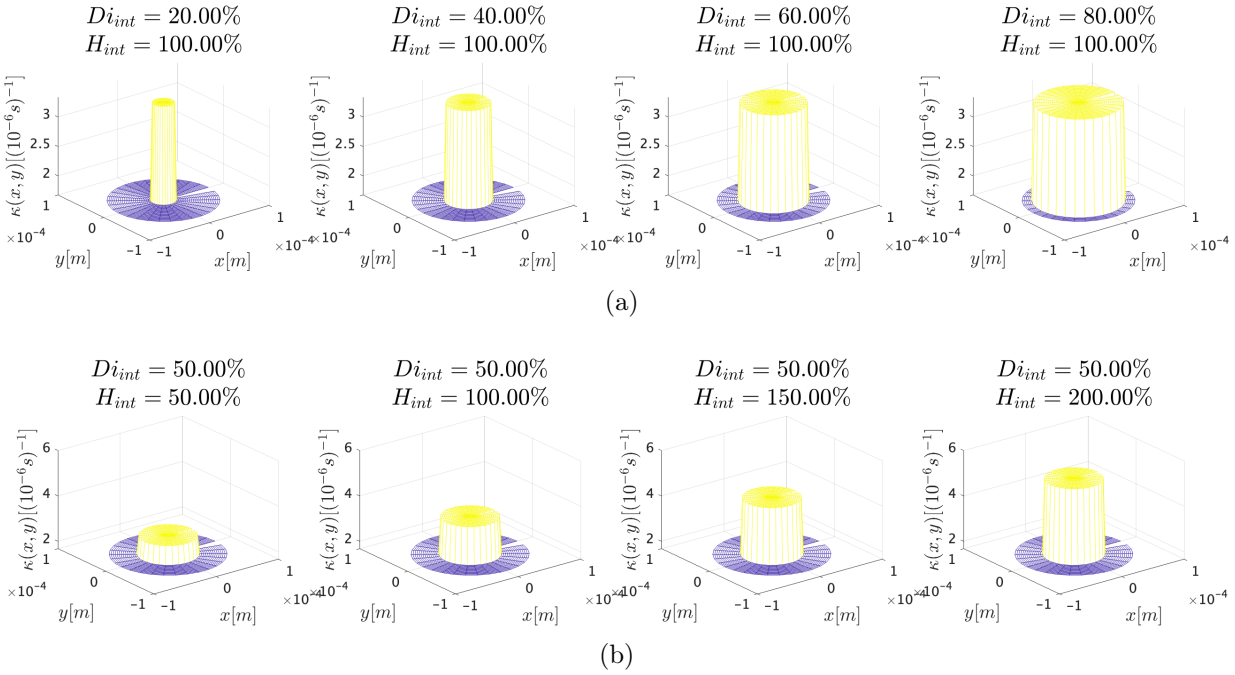

Figure 6.1: Stiffness parameter distribution of the Polar scheme as a function of (a) the internal diameter and (b) the internal thickness. The distribution is defined over a plate of 150 μm diameter and 15 μm of thickness, using a time scaling factor $\sigma = 10^{-6}$s.

6.3.2 Cartesian coordinates

In Cartesian coordinates, the stiffness parameter distribution is *smoothed*, by defining a logistic-type function for the stiffness parameters, given by

$$\kappa(r) = \kappa_{\text{int}} - \frac{(\kappa_{\text{int}} - \kappa_{\text{ext}})}{1 + \exp(-k_s(r - R_{\text{int}}))}, \tag{6.31}$$

where $L = Di_{\text{ext}}$ is used as the spatial scaling parameter, k_s is the *logistic growth rate* and R_{int} is the internal radius, and is also where the change of stiffness distribution happens, also know as the simoid's midpoint. In this way, the stiffness parameter distribution is taken as the logistic-type function (6.31), with radial coordinate

$$r_{l,m} = \sqrt{(l - (Nx-1)/2)^2 + (m - (Ny-1)/2)^2}. \tag{6.32}$$

Varying the internal diameter and thickness values has the same effect as the one showed for the polar coordinates scheme. The main difference is that the logistic growth rate, k_s, controls the smoothness of the transition between the stiffness paremeter values. Figure 6.2 illustrates the behaviour of the stiffness distribution with respect to the values of k_s. It can be noticed, that using a low value of k_s can lead to a very *'loose'* distribution, and, on the other hand, using a too large value can lead to a very pronounced jump. For the experiments we made to obtain results, the value was taken something in the middle, $k_s = 2$, which allows to have less numerical

instability, while it shows a good correspondence with the Polar scheme results, which has no instability (as shown in section 6.6).

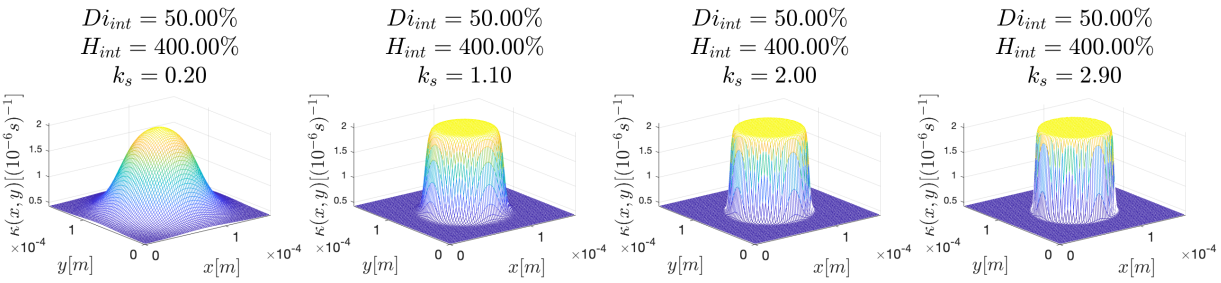

Figure 6.2: Stiffness parameter distribution in of the Cartesian scheme as a function of the logistic growth rate, k_s. The distribution is defined over a CYTOP plate of 150 μm diameter and 15 μm of thickness with a gold loading, using a time scaling factor $\sigma = 10^{-6}$s.

6.4 Measurement procedure

The simulations of at certain time steps for the Cartesian and polar schemes, with and without loading, are shown in figures 6.3 and 6.4.

In order to study the behaviour of the plate vibrations, certain points of the domain, called *readout positions*, are chosen to store the closest grid function values to these points at each temporal step. At each readout position, the stored values conform a signal that can be further analysed. In figure 6.5 the plot of three readout points is shown. The readout position is specified in polar coordinates because these measurements came from the polar coordinate scheme. The radial coordinate has values from 0 to 1, where 0 represents the centre of the plate and 1 the fixed border at radius R_{ext}, while the angular coordinate θ runs from 0 to 2π. It can be noticed that the amplitude of the signal decreases as the readout position is closer to the border. Notice that in the Cartesian coordinates scheme the readout position has to be given be two coordinates running from 0 to 1, where (0.5,0.5) represents the centre of the plate.

The frequency content of the signals is obtained by computing a Fast Fourier Transform (FFT) to each signal. In short, the FFT transforms the signals defined in the time-amplitude space to the frequency-energy space, and the absolute value of the transformed signal is directly related to the energy content of each frequency. The frequencies are then obtained by applying a find peaks algorithm. In figure 6.6 the absolute value of the FFT of the signals in figure 6.5 as a function of the frequency are shown. With blue inverted triangles the peaks found by the find-peaks algorithm are shown. On top of each plot the readout position is specified, and the first frequency found by the algorithm, $f_{1^{\text{st}}}$, together with the most energetic frequency, $f_{\max}$, are shown. As can be noticed, the frequency content can vary depending on the readout position. This will be important when measuring the harmonicity of a loaded plate, as the frequency of consecutive modes of vibration needs to be measured.

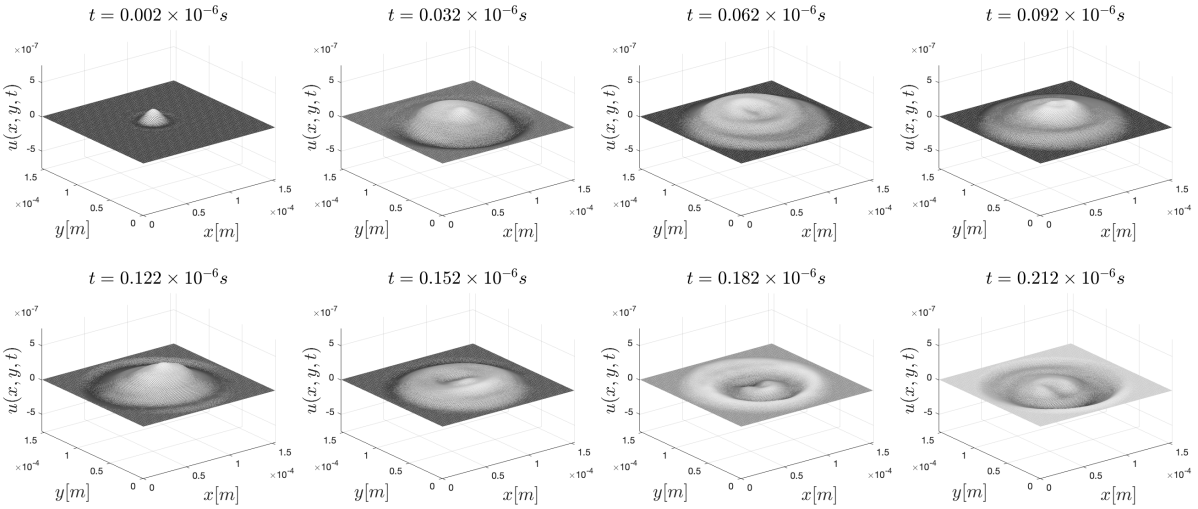

(a)

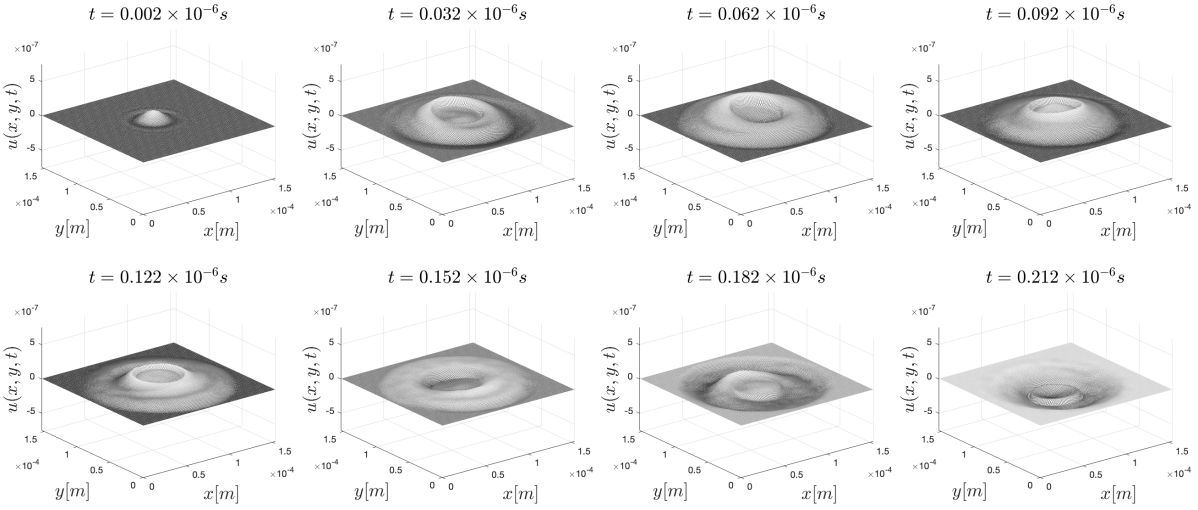

(b)

Figure 6.3: Different moments of the simulation of the plates vibration with an initial velocity placed out of the centre. (a) Cartesian scheme without loading, (b) Cartesian scheme with loading.

The find peaks algorithm employs two main parameters to find the local maximums. The minimum peak distance (mpd) which in this case is given in MHz, the minimum peak height (mph), which we implemented to be imputed as a fraction of the maximum peak height. This algorithm also allows to find the peaks width as the length of the half-prominence line[2]. This width will be useful when computing the quality factor.

[2]For more information, visit `https://www.mathworks.com/help/signal/ref/findpeaks.html`.

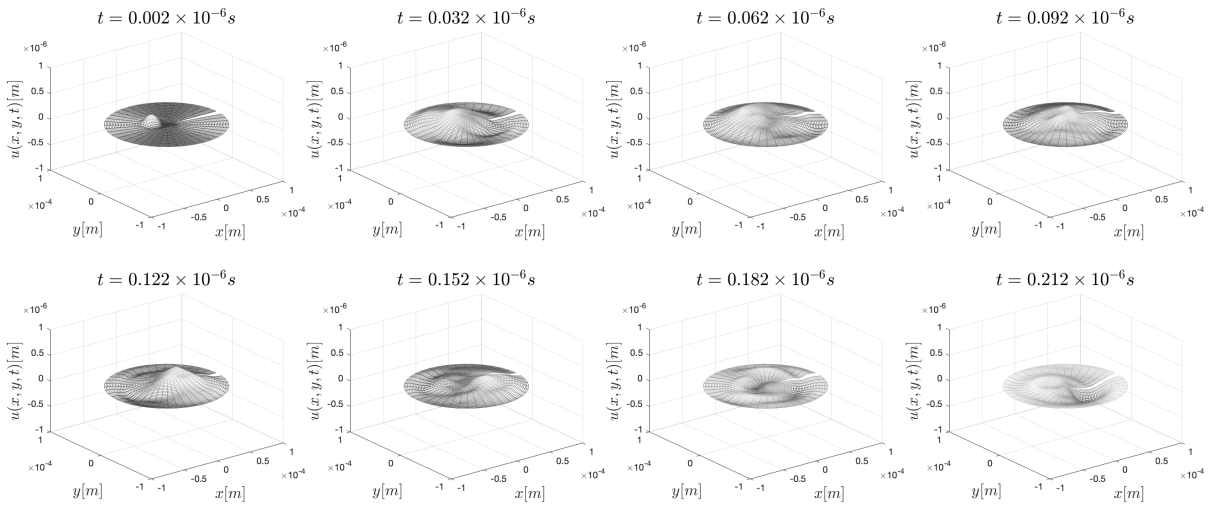

(a)

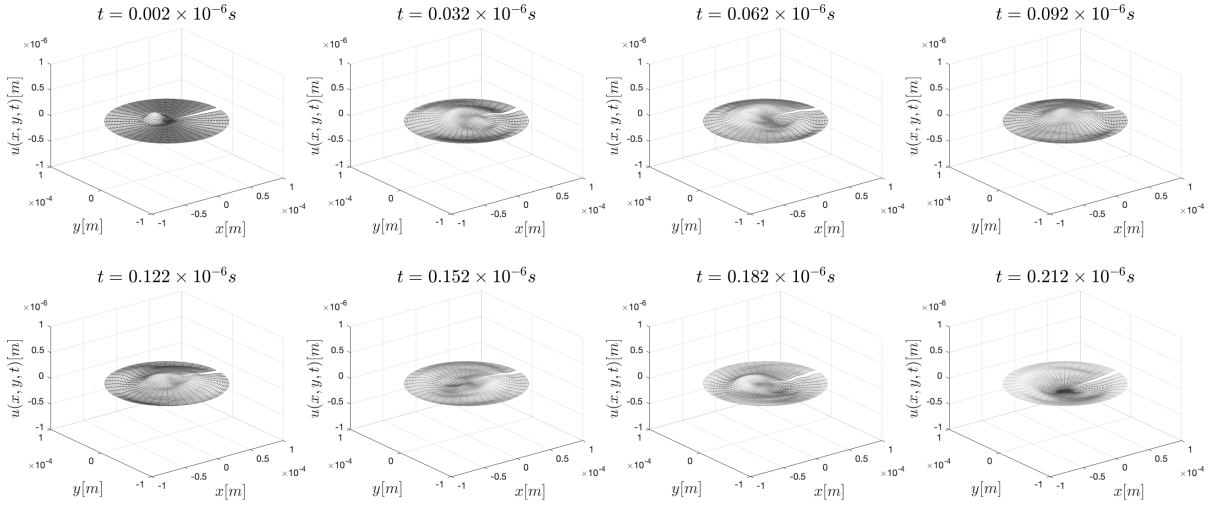

(b)

Figure 6.4: Different moments of the simulation of the plates vibration with a initial an initial velocity placed out of the centre. (a) Polar scheme without loading, (b) polar scheme with loading.

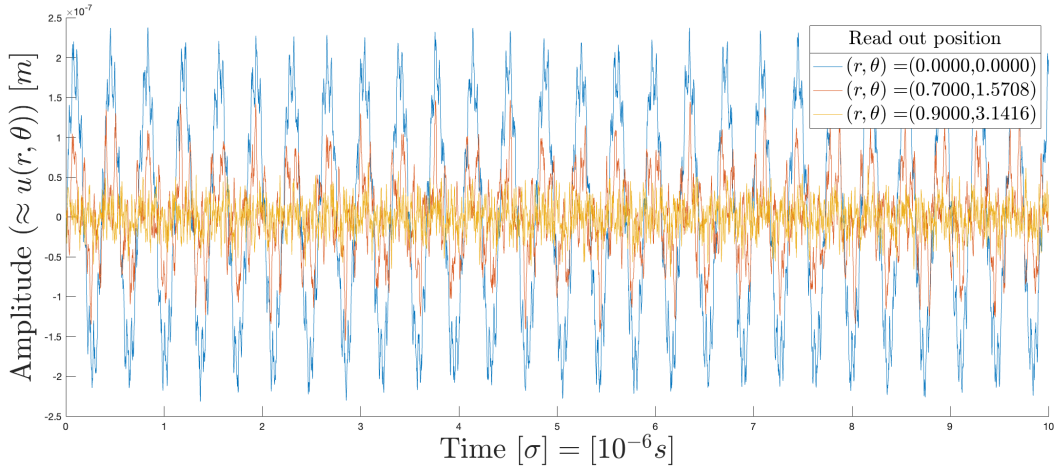

Figure 6.5: Signals of three readout positions as specified. The value of $u(r,\theta)$ is an approximation because (r,θ) is approximated by the closest grid point.

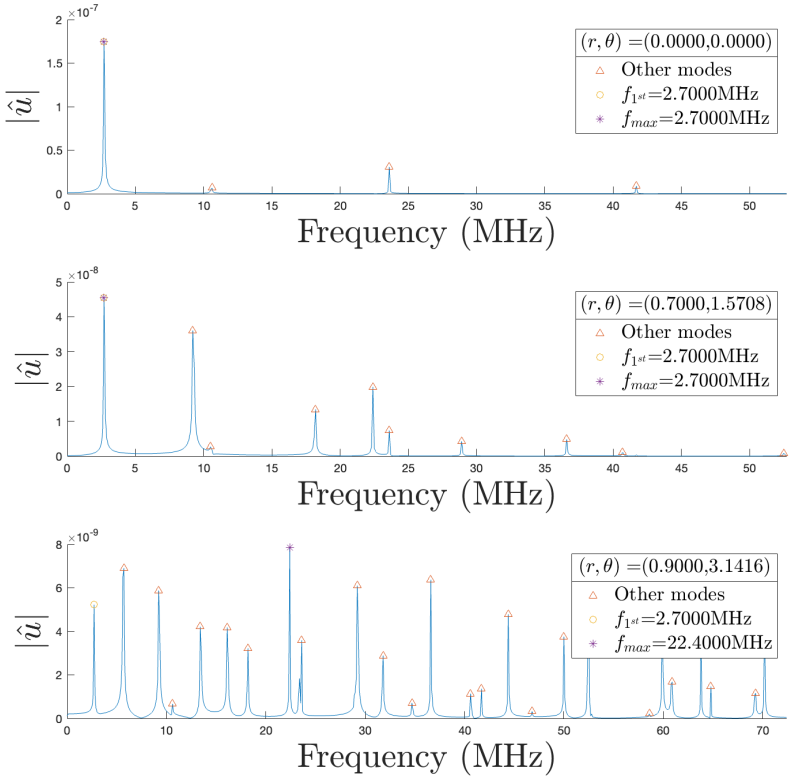

Figure 6.6: Fast Fourier Transform of the signals in figure 6.5 corresponding to the three specified readout positions.

6.5 Homogeneous case: proof of consistency

The exact values of the frequency of the first modes of vibration in a circular homogeneous plate with diameter L and thickness H, can be computed using the analytical solution found in section 3.2.4, as

$$\omega_{m,n} = \sqrt{\frac{D}{\rho H}} \frac{\lambda^2_{m-1,n}}{(L/2)^2}$$

and then using that

$$f_{m,n} = \frac{\omega_{m,n}}{2\pi},$$

where $m \in \mathbb{N}$, $n \in \mathbb{N} \cup \{0\}$, and the values of $\lambda^2_{m-1,n}$ are given in table 3.1, where m represents the diameter nodal mode number and n the circular nodal mode number. The correspondence of this modes numbers and the numbers at the table 3.1 is $m = s + 1$ (the number of circular nodes) and $n = n$ (the number of radial nodes).

In this way, the eigen-frequencies of the first six modes of vibration in increasing order, of a CYTOP plate of 150 μm diameter and 15 μm of thickness are given by

$$\begin{aligned} f_{1,0} &= 2.7218\text{MHz}, \\ f_{1,1} &= 5.6620\text{MHz}, \\ f_{1,2} &= 9.2893\text{MHz}, \\ f_{2,0} &= 10.5916\text{MHz}, \\ f_{1,3} &= 13.5930\text{MHz}, \\ f_{2,1} &= 16.1977\text{MHz}. \end{aligned} \tag{6.33}$$

With these exact solutions, we performed the second proof of consistency of the Cartesian and polar schemes, by measuring their frequency response and comparing it with the exact eigen-frequencies. The consistency tests are performed in the frequency domain because the metrics we want to measure (harmonicity and quality factor) are defined within the frequency output of the system.

6.5.1 Cartesian scheme

For the Cartesian model, a standard proof of consistency for the numerical scheme was made in section 4.5.1, by writing down a Taylor expansion of the solution evaluated in the corresponding scheme, obtaining the approximation error, and proving that it converges to 0 as the grid is refined. Nevertheless, due to the approximation of the boundary condition, presented in section 4.5.1, a geometrical approximation error is induced. Therefore, a second proof of consistency was made by measuring the eigen-frequency response of the homogeneous numerical system while the spatial grid is refined, and comparing it with the analytical solutions. In figure 6.7 the percentage errors of the frequencies obtained, $f^{\text{num.}}_{m,n}$ with respect to the analytical frequencies of

the corresponding mode of vibration, $f_{m,n}$, given by

$$\%\text{Error} = 100 \times \frac{f_{m,n}^{\text{num.}} - f_{m,n}}{f_{m,n}} \tag{6.34}$$

are presented. The results show a clear convergence of the frequencies of the first six modes of vibration. The mode (1,2) presents a small erratic behaviour, which can be explained by the geometrical approximation. As the grid is refined, the approximation to a perfect circle increases, but for some values the radius of the approximated circle can be under or over estimated, depending on the parity of the number of grid subdivisions N_x.

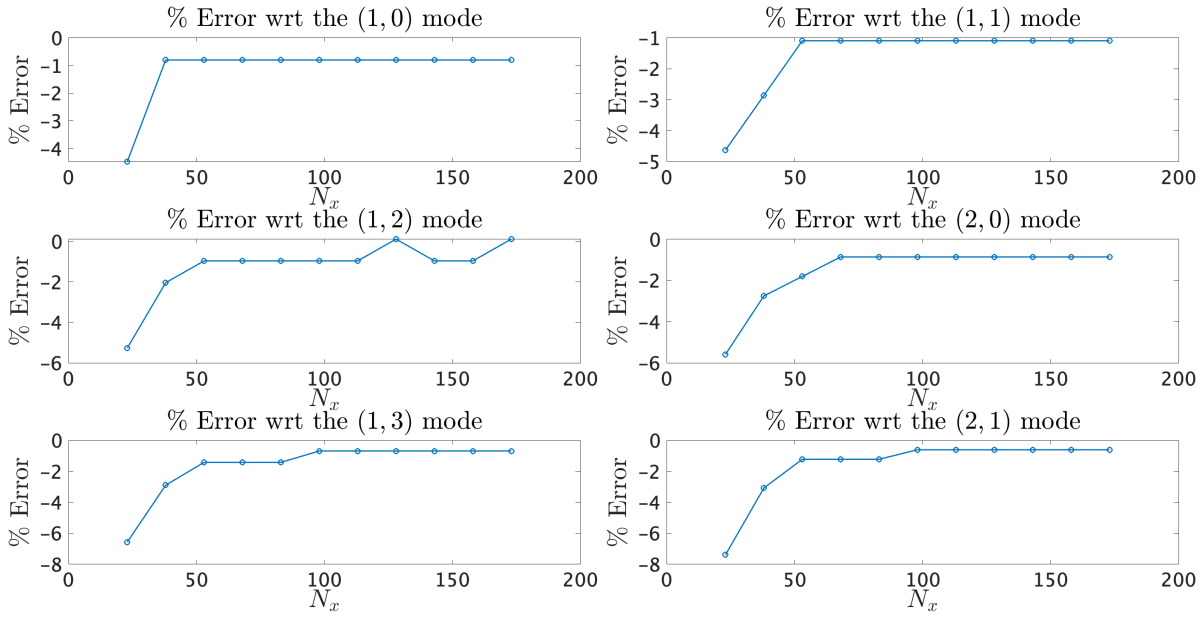

Figure 6.7: Percentage error with respect to (wrt) the analytic solution for the specified eigenmodes, as a function of the number of grid subdivisions. The correspondence of the modes number in this figure and the numbers at the table in figure 3.1 is that the first number is $s + 1$ (the number of circular nodes) and the second number is exactly n (the number of radial nodes). The error is reduced as the grid size increases.

This proves that for big enough N_x value the Cartesian coordinates scheme shows a good approximation to the circular plate system.

6.5.2 Polar scheme

The polar coordinates scheme was found by modifying the explicit version of the scheme proposed in [Bilbao, 2009], at the section (12.6). The modified scheme is now validated by comparing the modes of vibration of the scheme with the circular homogeneous plate eigen-frequencies. The percentage error of the first six modes of vibration of the homogeneous case (presented at the beginning of this section) compared with the frequencies obtained numerically with the Polar scheme, as the

spatial grid is refined are shown in figure 6.8. In all cases the percentage error tends to decrease as the grid is refined, which proves the consistency and convergence of this numerical procedure.

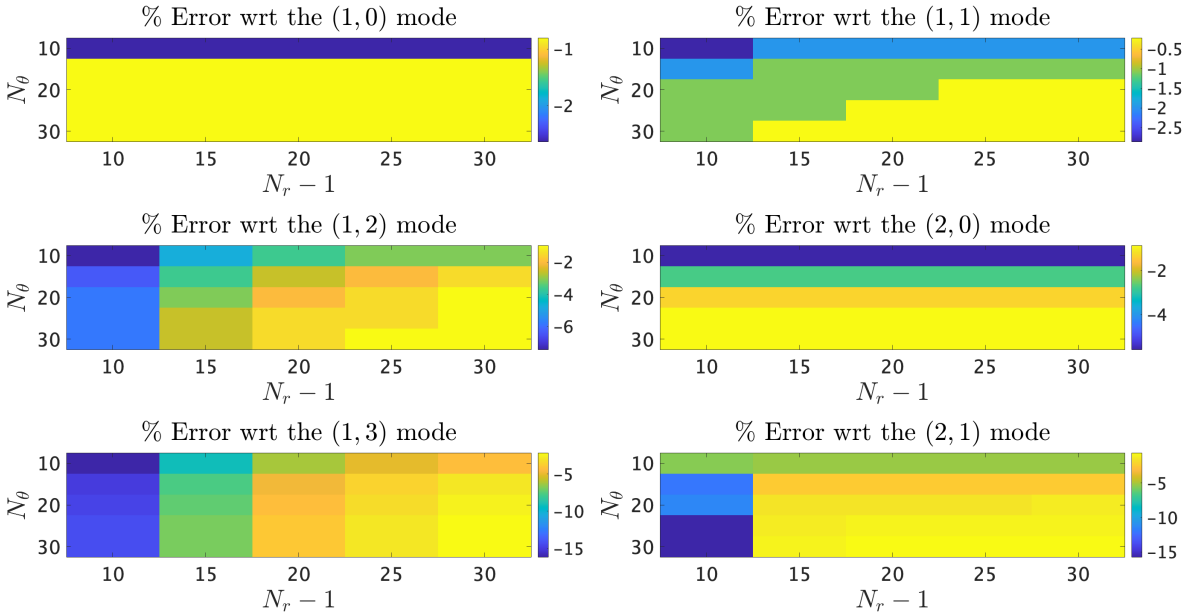

Figure 6.8: Percentage error with respect to (wrt) the analytic solution for the specified eigenmodes, as a function of the number of grid subdivisions. The correspondence of the modes number in this figure and the numbers in table 3.1 is that the first number is $s + 1$ (the number of circular nodes) and the second number is exactly n (the number of radial nodes). The error is reduced as the grid size increases.

6.6 Comparative study

6.6.1 Homogeneous case

We carried out a study to compare the performance of both schemes (the Cartesian and the polar coordinates one). In order to do this, we measured the performance of a homogeneous CYTOP plate of 150μm in diameter and 15μm in thickness, in three readout positions. The initial position was 0 all around the plate and the initial velocity has a rising cosine shape, given in equation (4.98) of width $r_w = Di_{ext}/4$ centred at $(x_0, y_0) = (0, 0)$, with a velocity-height c_0 induced by a kinetic energy $K = 10^{-3}$J[3]. In figure 6.9 the signal corresponding to these positions is shown, and in figure 6.10 the FFT of the signals in figure 6.9 is shown. In order to have comparable signals, the time-step size, k, has to be the same for both schemes. Therefore we set a

[3]The velocity-height and kinetic energy equivalence is explained in section 6.8, as it was implemented specifically for this numerical experiment.

spatial grid size for the polar scheme of $N_r = 30$ and $N_\theta = 20$[4] which induces, trough the stability condition (6.23), a time-step size of $k = 2.982 \times 10^{-5}\mu$s, this induces an x-axis grid size of the Cartesian scheme of $N_x = 145$.

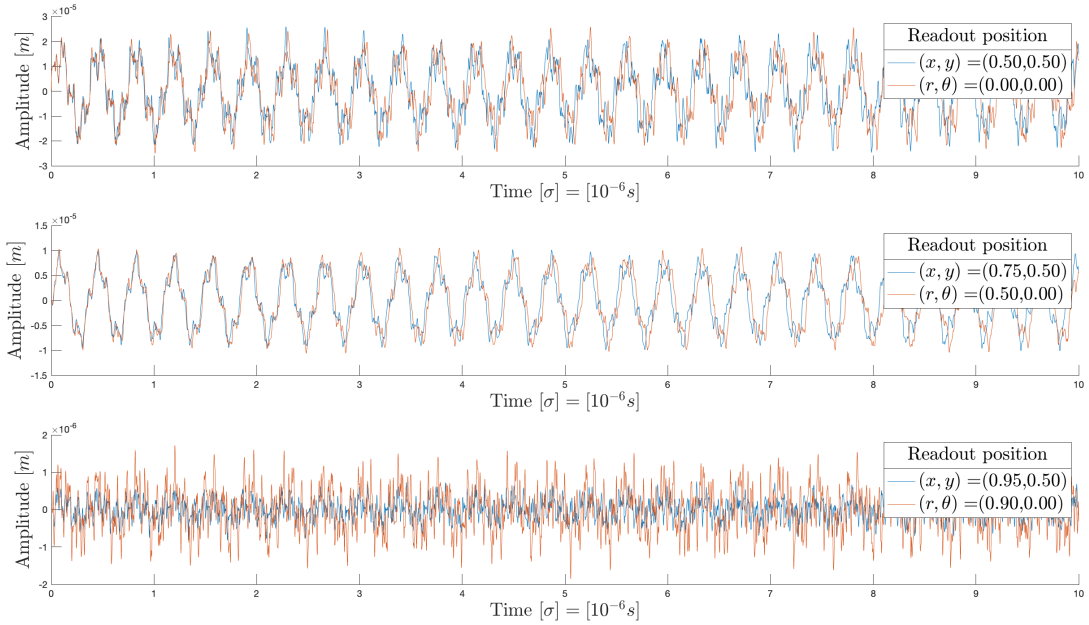

Figure 6.9: Signals from a homogeneous CYTOP plate, measured in the specified readout positions. The (x, y) readout position corresponds to the Cartesian coordinates scheme and the (r, θ) to the polar coordinates one.

[4]We tried to use $N_r = N_\theta = 30$, but this induces an N_x size that is too large for Matlab to perform the required matrix operations.

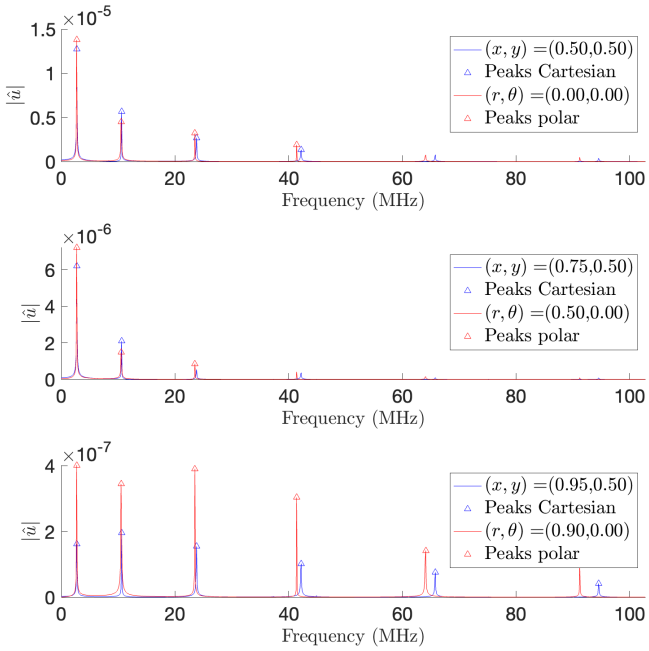

Figure 6.10: Absolute value of the FFT of the signals in figure 6.9, as a function of the frequency. The (x, y) readout position corresponds to the Cartesian coordinates scheme and the (r, θ) to the polar coordinates one.

In the time domain (figure 6.9), the signals measured in the centre ($(x, y) = (0.5, 0.5)$, $(r, \theta) = (0, 0)$) and in the mid-radius point ($(x, y) = (0.75, 0.5)$, $(r, \theta) = (0.5, 0)$) are very similar in the first time steps. As the time lapse increases, certain change in phase is noticeable, which may be due to the difference in the discretisation. The signal measured close to the boundary ($(x, y) = (0.95, 0.5)$, $(r, \theta) = (0.9, 0)$) differ in amplitude. This difference may be due to the approximation of the boundary condition

$$\frac{\partial u}{\partial r} = 0. \tag{6.35}$$

The approximation of the zero radial derivative is given in a more direct way in the polar coordinates scheme than in the Cartesian one.

In the frequency-energy domain (figure 6.10), for low frequencies, similar results are found for the values of the peak-frequencies, even when in the time domain and in the energy of these frequencies the results may differ. Certain discordance in the peak-frequency values are notable for higher frequencies, probably due to the difference in the discretisation of each scheme.

6.6.2 Loaded case

We made a study to compare the performance of both schemes, now with a loading. In order to do this, we measured the performance of a CYTOP plate of 150μm in diameter and 15μm in thickness loaded with gold using the values of $Di_{int} = 50\%$ and $H_{int} = 160\%$, in the same three readout positions as in the homogeneous case. The initial conditions were taken as in the homogeneous case, with the velocity-height value adapted to the loaded mass (refer to section 6.8 for the details). As before, in figure 6.11 the signal corresponding to these positions is shown, and in figure 6.12 the FFT of the signals in figure 6.11 is shown. We set a spatial grid size for the polar scheme of $N_r = 30$ and $N_\theta = 20$ which induces a time-step size of $k = 1.15 \times 10^{-5}\mu$s, this induces an x-axis grid size of the Cartesian scheme of $N_x = 145$.

In the time domain (figure 6.11), the signals measured in the centre ($(x, y) = (0.5, 0.5)$, $(r, \theta) = (0, 0)$) are very similar in the first time steps. As the time lapse increases, certain change in phase is noticeable, as observed in the homogeneous case. For the signals measured at the mid-radius point ($(x, y) = (0.75, 0.5)$, $(r, \theta) = (0.5, 0)$) and the point close to the boundary ($(x, y) = (0.95, 0.5)$, $(r, \theta) = (0.9, 0)$) we can notice a great amplitude difference, with the Cartesian scheme having a bigger amplitude than the polar coordinates one. In this case, the difference of amplitude is not explained by the boundary conditions. It is due to the *dispersion* presented in the Cartesian coordinates scheme when the load stiffness is big enough and the transition in the stiffness parameter distribution is abrupt (or not smooth enough). The signals of the polar coordinate scheme still behave as in the homogeneous case, they decrease in amplitude as the readout position tends to the fixed boundary.

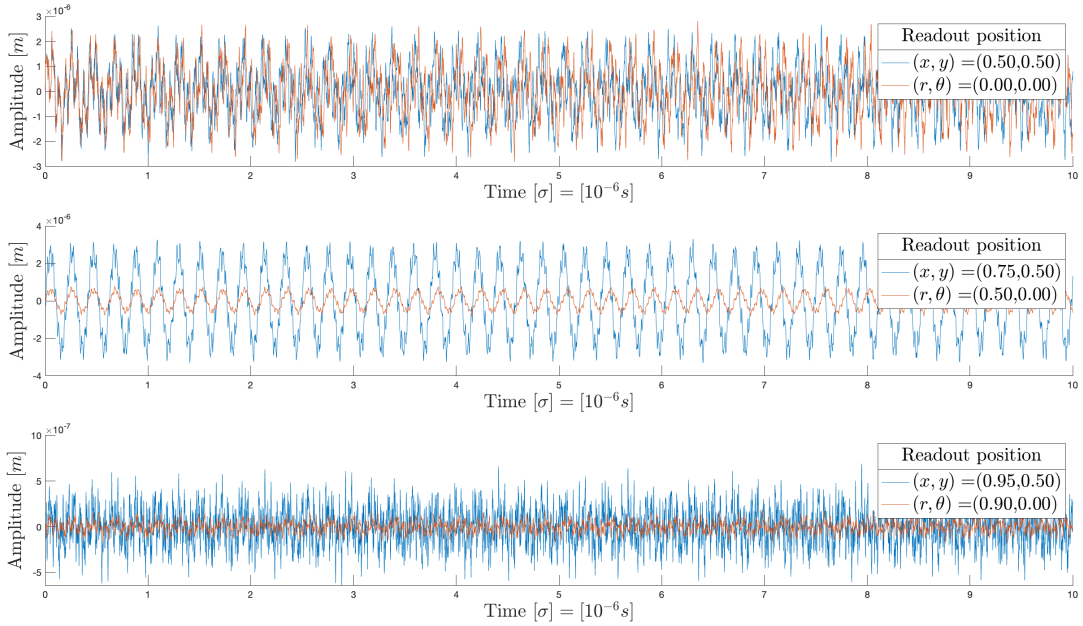

Figure 6.11: Signals from a CYTOP plate loaded with gold, with $Di_{int} = 50\%$ and $H_{int} = 160\%$, measured in the specified readout positions. The (x, y) readout position corresponds to the Cartesian coordinates scheme and the (r, θ) to the polar coordinates one.

In the frequency-energy domain (figure 6.12), for low frequencies, similar results are found for the values of the peak-frequencies, when comparing both schemes. The discordance in the peak-frequency values given in the homogeneous case for higher frequencies remain, but do not increase significantly with the frequency. It is only noticeable the expected change in energy, due to the amplitude difference.

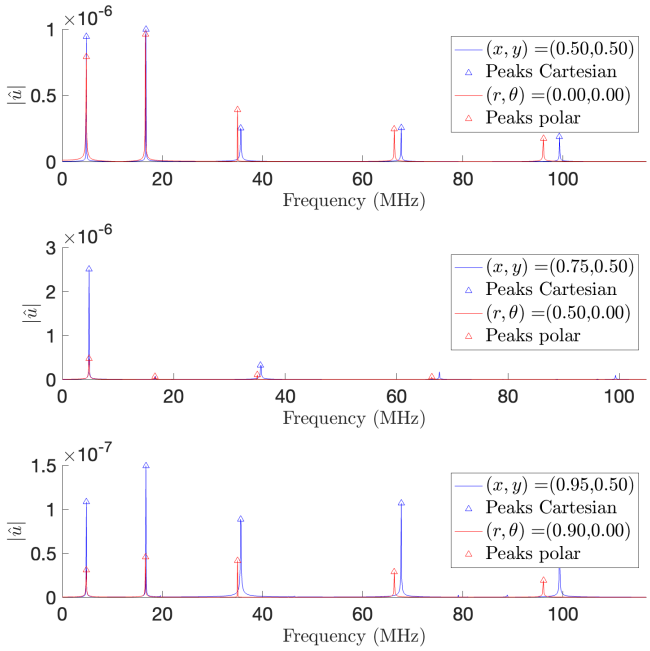

Figure 6.12: Absolute value of the FFT of the signals in figure 6.11, as a function of the frequency. The (x, y) readout position corresponds to the Cartesian coordinates scheme and the (r, θ) to the polar coordinates one.

6.7 Harmonicity

For both, the Cartesian and the polar coordinates schemes, 200 simulations were made. The initial position was set to zero, and the initial velocity was taken as a thin raised cosine out of the centre, to stimulate the more possible modes. In each simulation, a $150\mu m$ diameter CYTOP plate of $15\mu m$ thickness was loaded with a circular gold cover. The loading diameter was increased by 10% of the total diameter in each simulation until the complete CYTOP plate was covered. The thickness of the loading was run from 10% to 50% of the thickness of the unloaded plate, following a linear mapping. The 0% thickness and diameter case was added afterwards to complete the parameters space exploration, because it only has to be computed once, as it corresponds with the homogeneous case. The signal of the grid function values in several different readout positions was stored in each simulation, in other to capture the more possible modes of vibration, and avoid the discontinuities in the measurements.

The Fast Fourier Transform (FFT) was computed for each of this signals. For each FFT signal, the finding peak algorithm was implemented to extract the frequency of the first vibration modes. Then, the frequencies found for each readout point are stored in a concatenated array, finally using a *unique algorithm with tolerance*[5] to keep only the frequencies corresponding to a sequential order. For example, the array

```
a=[1, 2, 3, 4, 5, 1, 1.95 ,3.05 ,5.1]
```

is transformed with the unique algorithm with tolerance, with tolerance value tol=0.1, as

```
uniquetol(a,0.1)=[1.0000, 1.9500, 3.0000, 4.0000, 5.0000]
```

An approximation error with the value of the tolerance is introduced, therefore, is better to keep it relatively low.

In summary, the parameters of these measurements are: the minimum peak distance (mpd) in [MHz], the minimum peak height (mph) which is imputed as a the divisor (mphfrac) in the fraction mph = $f_{\max}$/mphfrac, where $f_{\max}$ is the maximum peak height, and the tolerance (tol) of the unique-algorithm to keep non-repetitive frequencies form all the readout points. The values of the frequencies for the homogeneous cases, that are given when the plate is unloaded and when is fully loaded (for each value of the load thickness), for which we have a analytical solutions, where used to estimate these parameters and to validate the measurements.

6.7.1 Cartesian scheme

Experimental setup

The spatial grid size was chosen is such a way that the previously reported percentage errors in figure 6.7 are minimised, given by

$$N_x = N_y = 128. \tag{6.36}$$

[5]For more information, visit `https://www.mathworks.com/help/matlab/ref/uniquetol.html`.

The initial position and the initial velocity are shown in figure 6.13. The initial velocity is given by a raised cosine with centre (0.7,0.7) and width 0.25, both expressed as fractions of the external diameter Di_{ext}.

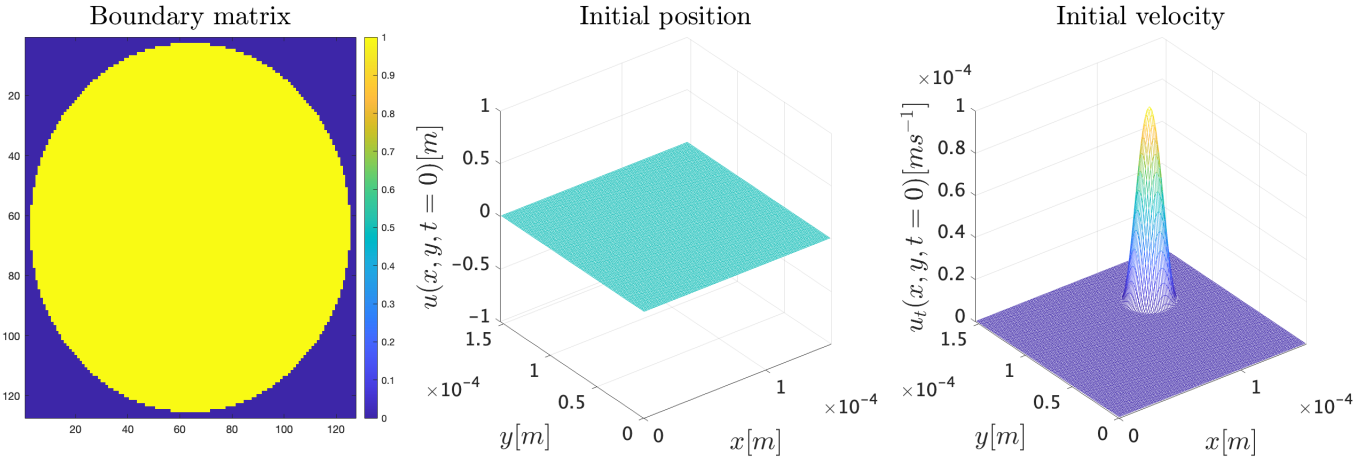

Figure 6.13: Boundary matrix and initial conditions for the harmonicity experiment, for the Cartesian coordinates scheme.

The time scaling factor was taken as

$$\sigma = 10^{-6}s. \tag{6.37}$$

The total time of the simulation was

$$T_F = 20\mu s = 20\sigma. \tag{6.38}$$

As we are interested in the free-vibration modes, the experiments where run without damping, then

$$\sigma_0 = 0. \tag{6.39}$$

The chosen readout positions points, (x, y), expressed as fractions of the external diameter were

$$\begin{aligned} &(0.5, 0.5),\\ &(0.7, 0.7),\\ &(0.3, 0.2),\\ &(0.4, 0.3),\\ &(0.6, 0.7),\\ &(0.7, 0.8). \end{aligned} \tag{6.40}$$

The values of the find peaks and the unique algorithm parameters were

$$\begin{aligned} \text{mpd} &= 0.5\text{MHz}, \\ \text{mphfrac} &= 50, \\ \text{tol} &= 0.15. \end{aligned} \tag{6.41}$$

Results

The evolution of the first six vibration modes as a function of the internal diameter, for a given loading thickness is shown with coloured lines in figure 6.14.The integer multiples of each fundamental frequency (harmonic partials) are shown as a point of reference with black crosses. The values of the frequencies for the homogeneous cases, that are given when the plate is unloaded (Load diameter % ratio = 0) and when is fully loaded (Load diameter % ratio = 100) are represented by blue triangles.

The complete parameters space exploration is shown in figures 6.15 and 6.16, where the value of the quality function for harmonicity and rounded harmonicity as a function of the internal diameter and thickness is shown. The quality functions are measured by taking into account three to six modes of vibration.

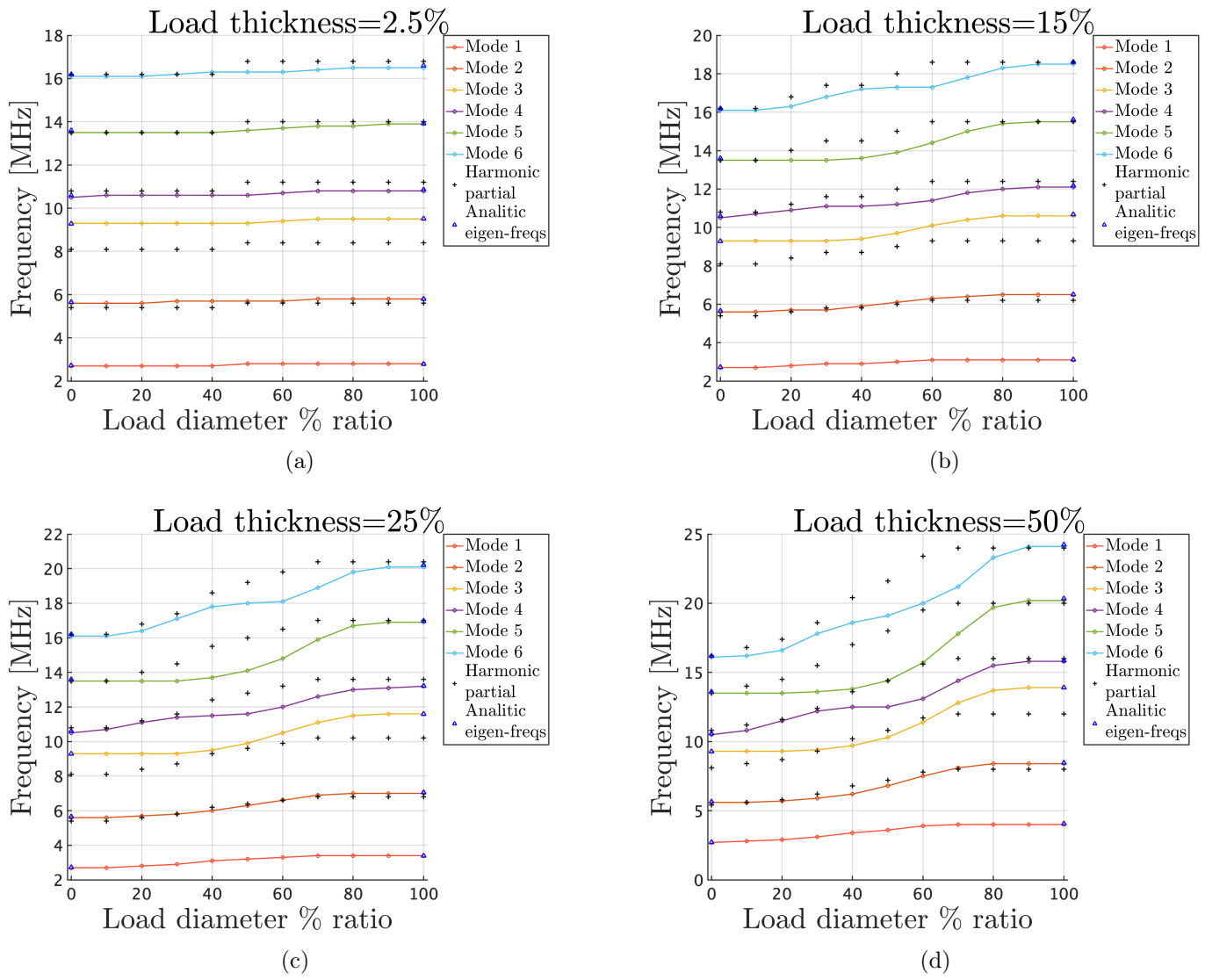

Figure 6.14: Cartesian scheme results. With coloured lines, the behaviour of the first 6 modes as a function of the internal diameter percentage ratio, for the specified loading thickness is shown. The harmonic partials corresponding to each fundamental frequency are indicated with black crosses. The values of the frequencies for the homogeneous cases, that are given when the plate is unloaded (Load diameter % ratio = 0) and when is fully loaded (Load diameter % ratio = 100) are represented by blue triangles. The frequencies measure in these homogeneous cases coincide with the corresponding analytical values, within the tolerance interval and are consistent with the percentage error previously measured. The values of the loading thickness percentage (H_{int}) are indicated on the top of each figure: (a) $H_{\text{int}} = 2.5\%$, (b) $H_{\text{int}} = 15\%$, (c) $H_{\text{int}} = 25\%$, (d) $H_{\text{int}} = 50\%$.

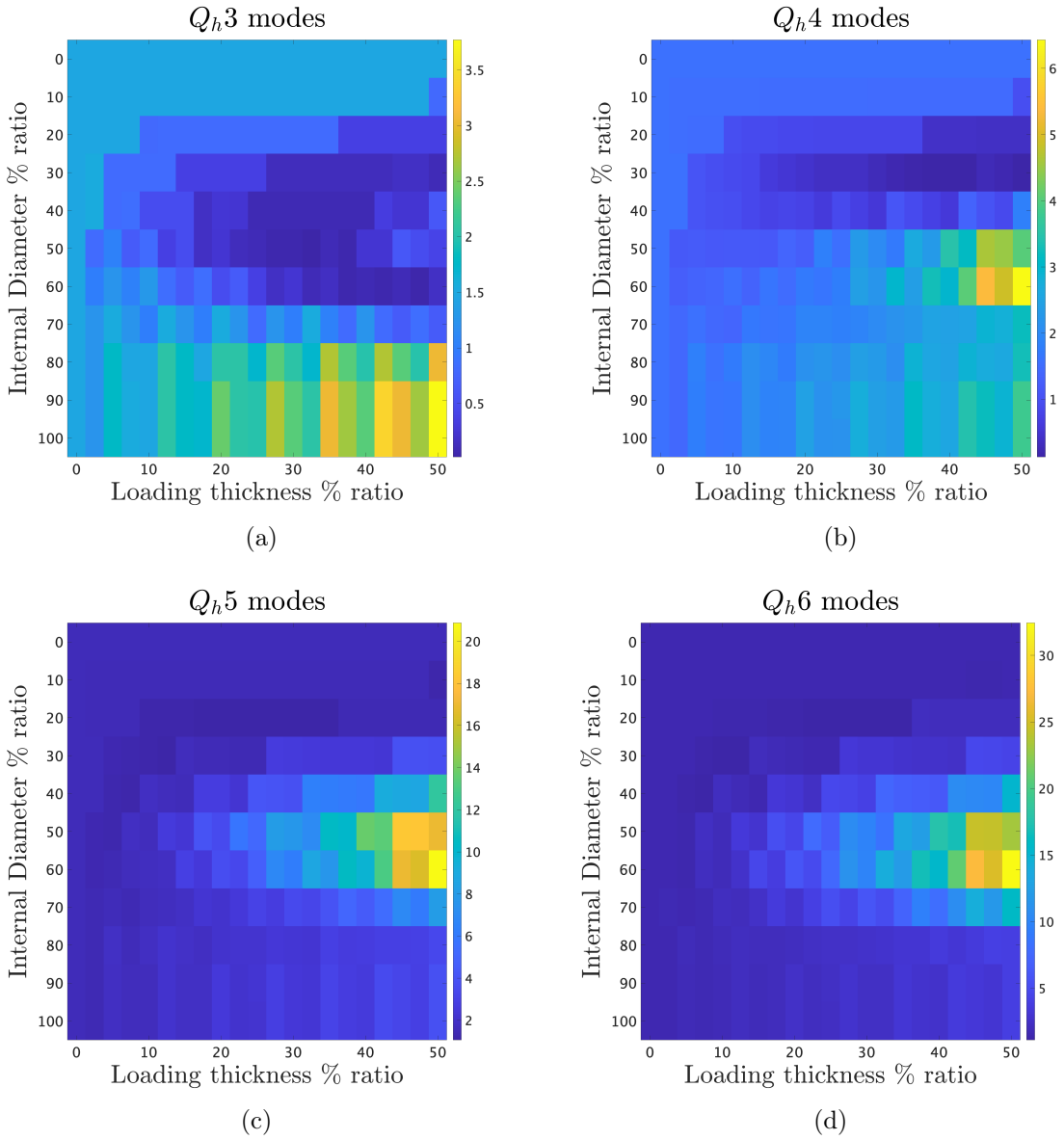

Figure 6.15: Cartesian scheme results. Harmonicity measured in the parameters space of the thickness (H_{int}) and the diameter (Di_{int}) of the load as a percentage ratio, for the first n modes, as indicated: (a) 3 modes, (b) 4 modes, (c) 5 modes and (d) 6 modes. The harmonicity increases as the value of Q_h decreases.

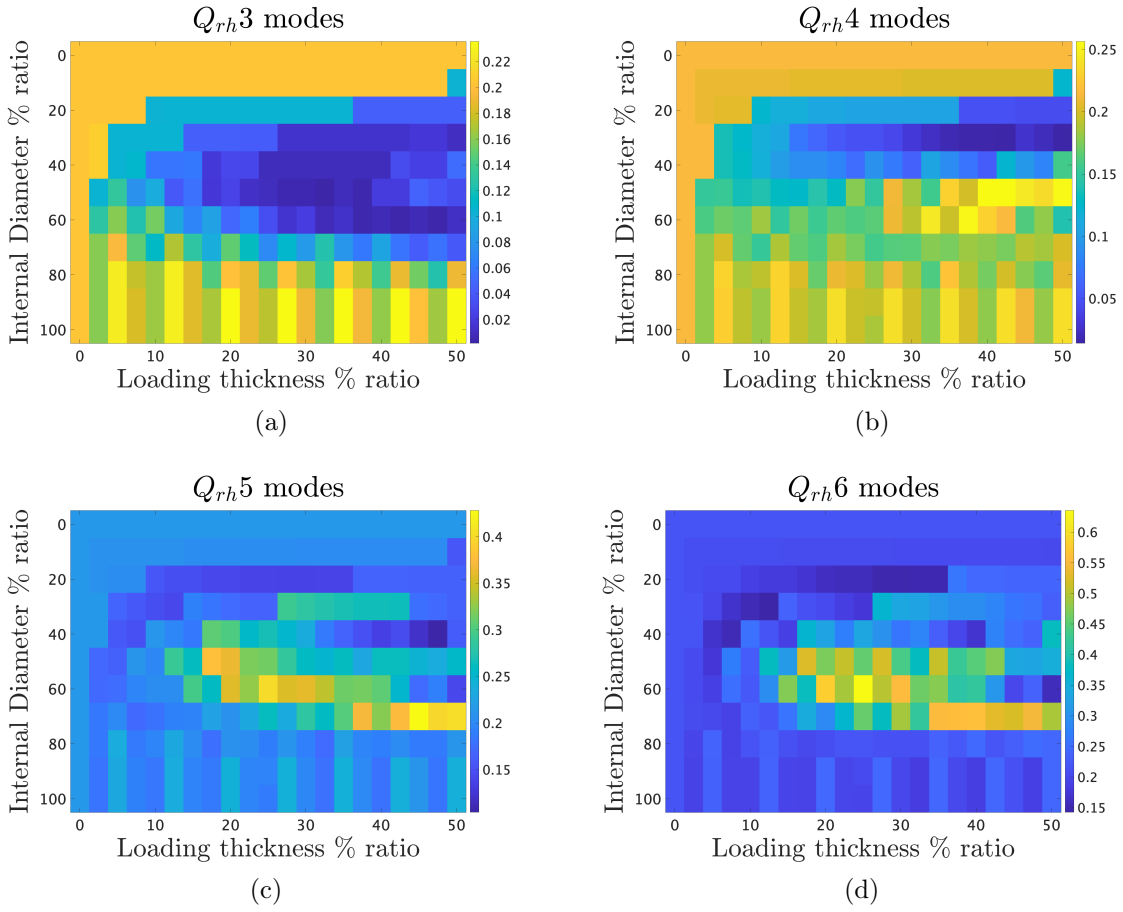

Figure 6.16: Cartesian scheme results. Rounded Harmonicity measured in the parameters space of the thickness (H_{int}) and the diameter (Di_{int}) of the load as a percentage ratio, for the first n modes, as indicated: (a) 3 modes, (b) 4 modes, (c) 5 modes and (d) 6 modes. The harmonicity increases as the value of Q_{rh} decreases.

6.7.2 Polar scheme

Experimental setup

The spatial grid size, which minimises the previously reported percentage errors in figure 6.8, was chosen as

$$N_r = N_\theta = 30. \tag{6.42}$$

The initial position and the initial velocity are shown in figure 6.17. The initial velocity is given by a raised cosine with centre $(0, 0.25)$ and width 0.07, both expressed as fractions of the external diameter Di_{ext}.

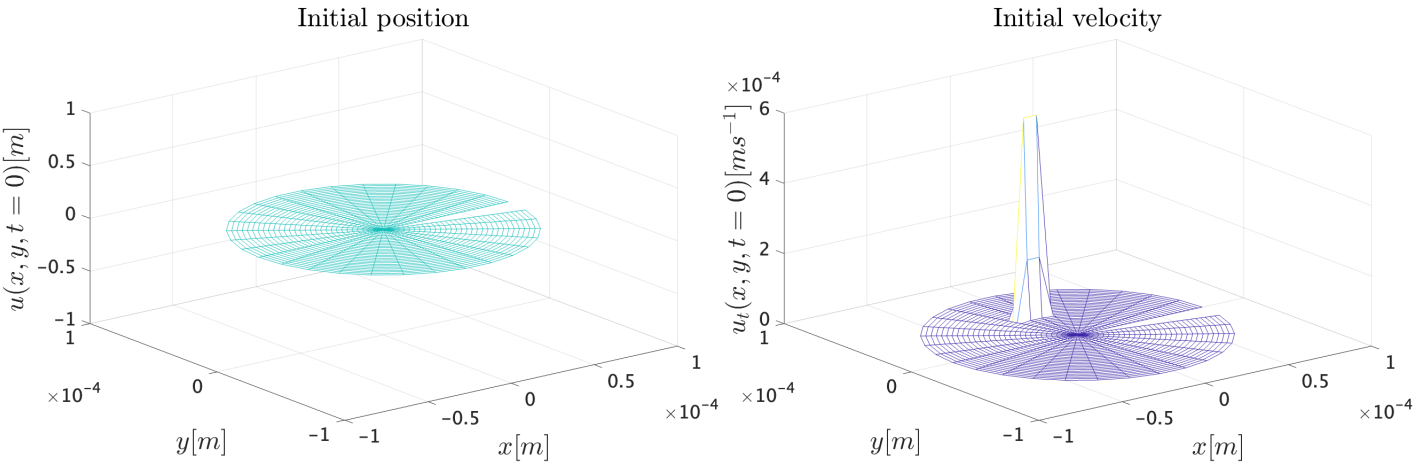

Figure 6.17: Initial conditions for the harmonicity experiment, for the polar coordinates scheme.
Note: it may look like there is a missing value, but we are showing the grid function domain which runs from 0 to $2\pi - h_\theta$.

The time scaling factor was taken as

$$\sigma = 10^{-6}s. \tag{6.43}$$

The total time of the simulation was

$$T_F = 20\mu s = 20\sigma. \tag{6.44}$$

As we are interested in the free-vibration modes, the experiments where run without damping, then

$$\sigma_0 = 0. \tag{6.45}$$

The chosen readout positions points, (r, θ), were

$$\begin{aligned} &(0.3605, 4.1244),\\ &(0.2236, 4.2487),\\ &(0.255, 4.5149),\\ &(0.2236, 1.0171),\\ &(0.3606, 0.9828),\\ &(0.5, 1.5708),\\ &(0, 0), \end{aligned} \tag{6.46}$$

where r is expressed as a fraction of the external radius, R_{ext}, and θ in radians.

The values of the find peaks and the unique algorithm parameters were

$$\begin{aligned} \text{mpd} &= 0.5\text{MHz},\\ \text{mphfrac} &= 50,\\ \text{tol} &= 0.08. \end{aligned}$$

Results

The evolution of the first six vibration modes as a function of the internal diameter, for a given loading thickness is shown with coloured lines in figure 6.18. The integer multiples of each fundamental frequency (harmonic partials) are shown as a point of reference with black crosses. The values of the frequencies for the homogeneous cases, that are given when the plate is unloaded (Load diameter % ratio = 0) and when is fully loaded (Load diameter % ratio = 100) are represented by blue triangles.

The complete parameters space exploration is shown in figures 6.19 and 6.20, where the value of the quality function for harmonicity and rounded harmonicity as a function of the internal diameter and thickness is shown. The quality functions are measured by taking into account three to six modes of vibration.

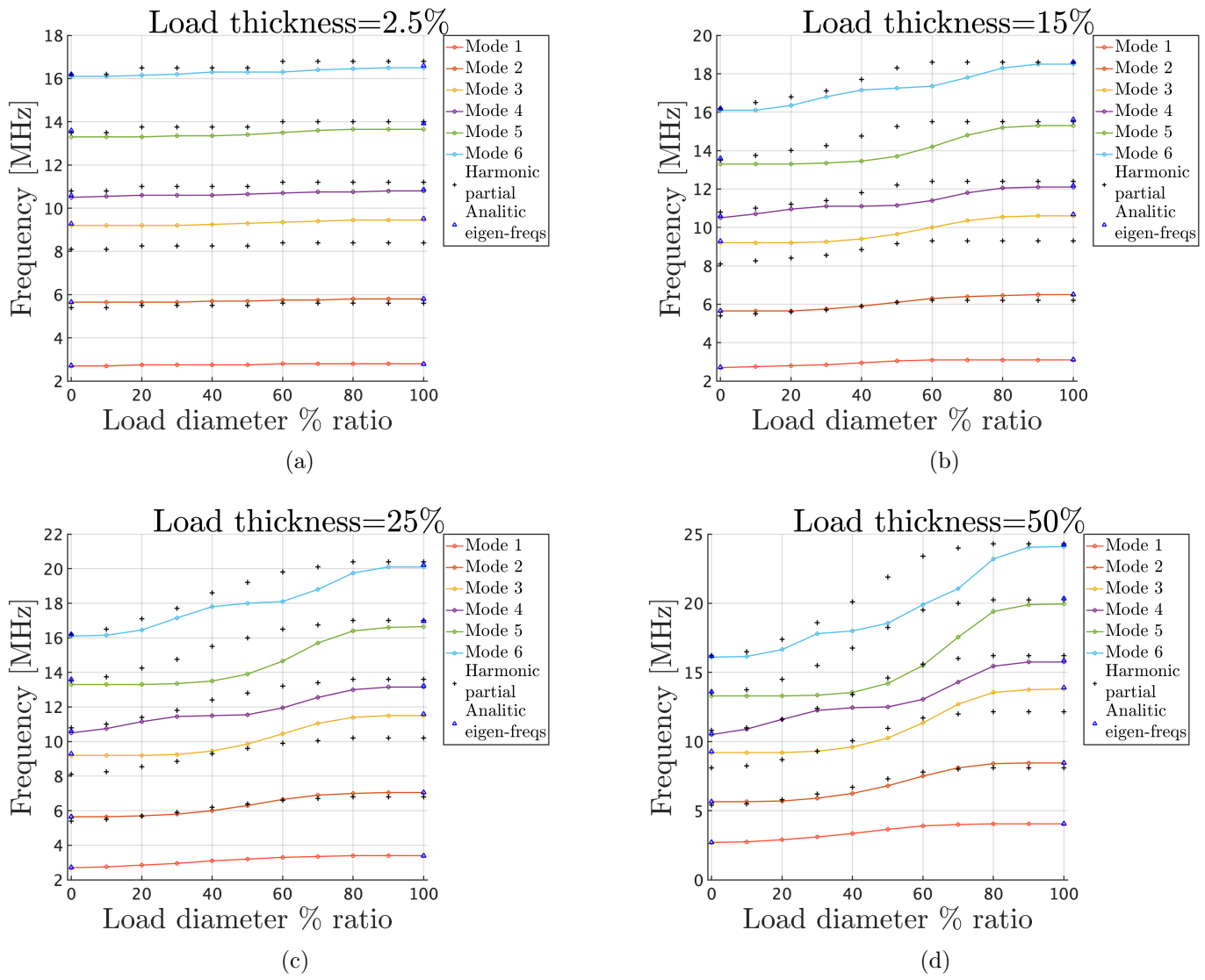

Figure 6.18: Polar scheme results. With coloured lines, the behaviour of the first 6 modes as a function of the internal diameter percentage ratio, for the specified loading thickness is shown. The harmonic partials corresponding to each fundamental frequency are indicated with black crosses. The values of the frequencies for the homogeneous cases, that are given when the plate is unloaded (Load diameter % ratio = 0) and when is fully loaded (Load diameter % ratio = 100) are represented by blue triangles. The frequencies measure in these homogeneous cases coincide with the corresponding analytical values, within the tolerance interval and are consistent with the percentage error previously measured. The values of the loading thickness percentage (H_{int}) are indicated on the top of each figure: (a) $H_{\text{int}} = 2.5\%$, (b) $H_{\text{int}} = 15\%$, (c) $H_{\text{int}} = 25\%$, (d) $H_{\text{int}} = 50\%$.

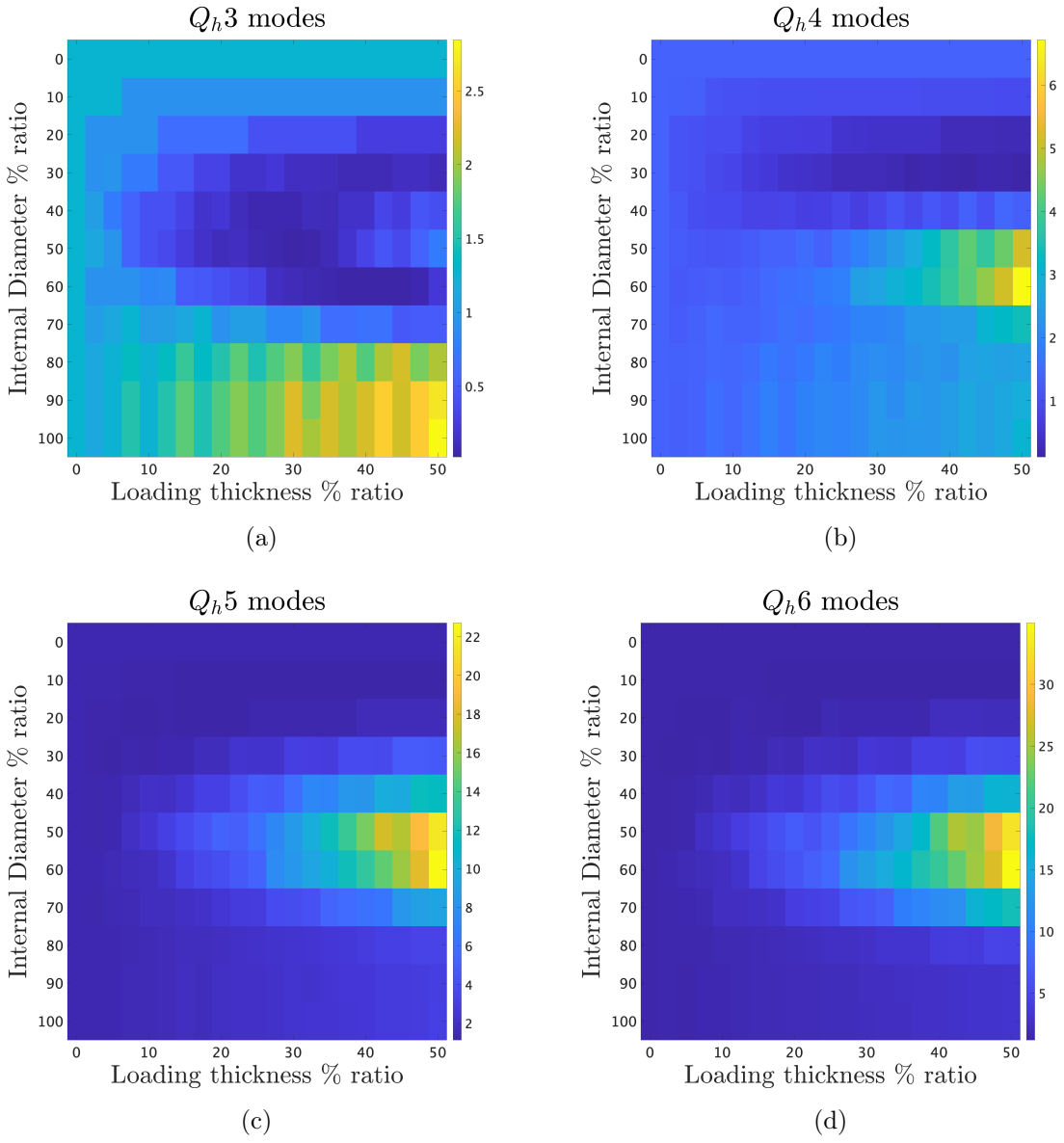

Figure 6.19: Polar scheme results. Harmonicity measured in the parameters space of the thickness (H_{int}) and the diameter (Di_{int}) of the load as a percentage ratio, for the first n modes, as indicated: (a) 3 modes, (b) 4 modes, (c) 5 modes and (d) 6 modes. The harmonicity increases as the value of Q_h decreases.

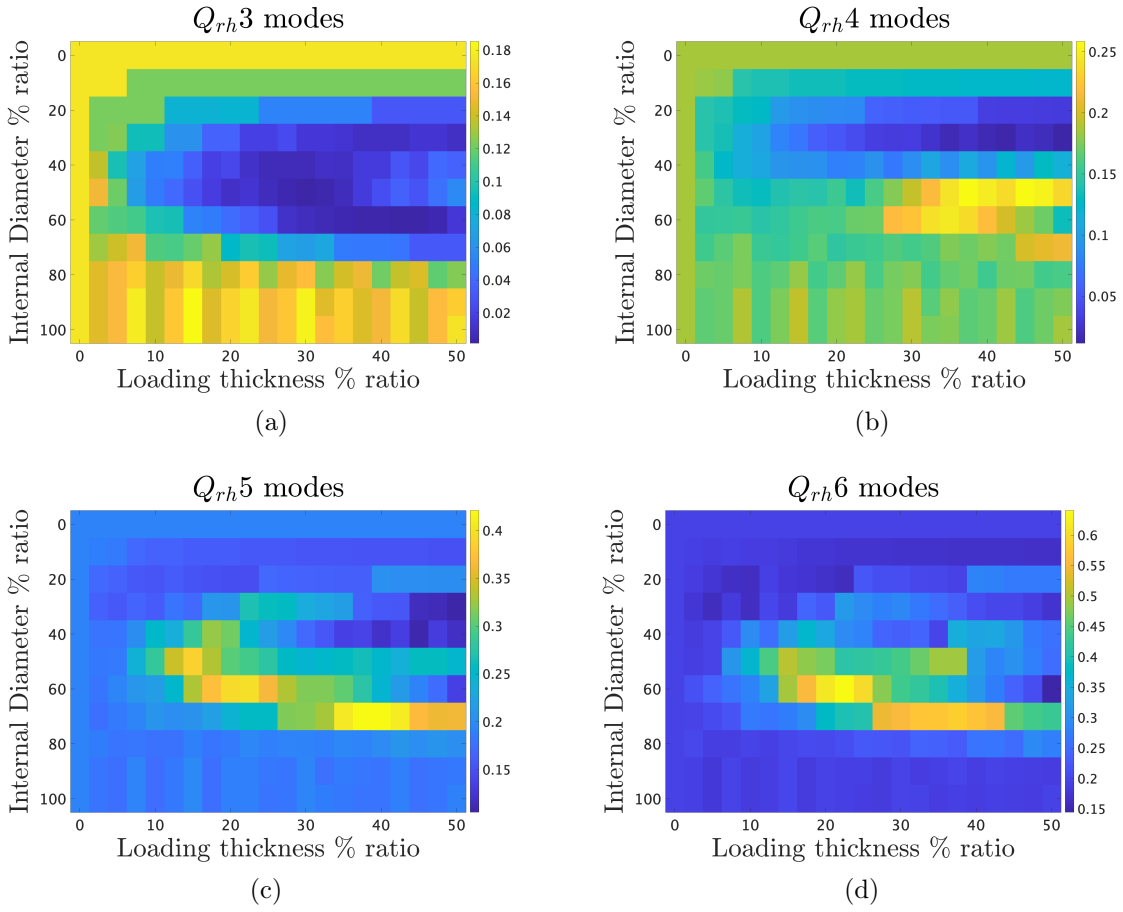

Figure 6.20: Polar scheme results. Rounded Harmonicity measured in the parameters space of the thickness (H_{int}) and the diameter (Di_{int}) of the load as a percentage ratio, for the first n modes, as indicated: (a) 3 modes, (b) 4 modes, (c) 5 modes and (d) 6 modes. The harmonicity increases as the value of Q_rh decreases.

6.7.3 Comments on the harmonicity results

- The results obtained with the Cartesian and the polar coordinates schemes are qualitatively similar, even when they differ in specific values. In both cases, a region of improvement in harmonicity can be found up to the 4th mode, for the values

$$Di_{\text{int}} \approx 30\%,\ H_{\text{int}} = 50\%. \tag{6.47}$$

  This improvement can be observed using both, the harmonicity quality function, Q_{h}, and the rounded harmonicity quality function, Q_{rh}.

- For higher order modes the harmonicity does not show a concrete behaviour in the parameters space.

- When trying to measure harmonicity for higher values of the load thickness, H_{int}, the frequencies start to overlap, making it difficult to measure. This region of the parameters space is studied in the quality factor section, but not for harmonicity measurements.

6.8 Quality factor

In order to explore the $Di_{\text{int}} \times H_{\text{int}}$ parameter space, for both, the Cartesian and the polar coordinates schemes, a set of 200 numerical experiments were run. In each experiment, a circular CYTOP plate of 150μm of diameter and 15μm of thickness was loaded in the centre with gold, varying the internal diameter from 0 to 100% and the internal thickness from 0 to 400%, following a linear map. Every experiment has the clamped boundary conditions explained before. The initial position was 0 all around the plate and the initial velocity has a rising cosine shape, given in equation (4.98) of width $r_w = Di_{ext}/4$ centred at $(x_0, y_0) = (0, 0)$.

The velocity-height constant, c_0, was taken in such a way that the total kinetic energy initially given to the plate was the same for every value of the loading, in order to have a comparable set of experiments. In order to do this, a simplification of the rising cosine shape of the initial velocity was made, thinking of it as a step function of the plate's radius, as

$$v_0^*(r) = \begin{cases} c_0, & \text{if} \quad r =< r_w, \\ 0, & \text{if} \quad r > r_w. \end{cases} \tag{6.48}$$

In this way, we can compute the kinetic energy as

$$\begin{aligned} K &= \frac{1}{2}\int_0^{2\pi}\int_0^{R_{\text{ext}}} H(r)\rho(r)v_0^*(r)^2\, r\, dr d\theta \\ &= \begin{cases} \pi[\frac{r_w^2}{2}(\rho_{\text{int}}H_{\text{int}})]c_0^2, & \text{if} \quad r_w =< R_{\text{int}}, \\ \pi[\frac{R_{\text{int}}^2}{2}(\rho_{\text{int}}H_{\text{int}}) + \frac{(r_w - R_{\text{int}})^2}{2}(\rho_{\text{ext}}H_{\text{ext}})]c_0^2, & \text{if} \quad r_w > R_{\text{int}}. \end{cases} \end{aligned} \tag{6.49}$$

This kinetic energy is greater than the one impressed by the rising cosine function, however, it is equally over-estimated for a given value of c_0. Therefore, by fixing a value of K, the corresponding value of c_0 can be found depending on the relation between the radius of the loading R_{int} and the width of the rising cosine r_w, as

$$c_0 = \begin{cases} \sqrt{K/(\pi[\frac{r_w^2}{2}(\rho_{\text{int}}H_{\text{int}})])}, & \text{if} \quad r_w =< R_{\text{int}}, \\ \sqrt{(K/(\pi[\frac{R_{\text{int}}^2}{2}(\rho_{\text{int}}H_{\text{int}}) + \frac{(r_w - R_{\text{int}})^2}{2}(\rho_{\text{ext}}H_{\text{ext}})])}, & \text{if} \quad r_w > R_{\text{int}}. \end{cases} \tag{6.50}$$

If the variables involved are given in the SI units, then, the units of the velocity height are $[c_0]$ =m/s. In order to initialise the scheme, the units of velocity have to be given in the same units of the temporal step k. For example, if $\sigma = 10^{-6}$s, then s= $10^6\sigma$ the scaled velocity height is $c_0^* = 10^{-6}c_0$.

In order to measure and quantify the performance of the vibrating loaded circular plate, we measure the quality factor of the signal of the deflection of the centre point of the plate. For each value of the internal diameter and thickness, this signal was stored and then analysed. The analysis consisted in computing the FFT of this signal in order to obtain the resonant frequency and the resonant band-width. We used the band-width definition Q_w (given in section 5.2) to measure the quality factor of

the loaded-damped plate. As the FRF we will use the absolute value of the FFT of the signal measured at the centre of the plate. As the the resonant frequency, f_{res} the maximum value in the FRF, and Δf will be measured as the resonance width or full width at half maximum (FWHM), i.e., the band-width over which the power of vibration is greater than half the power at the resonant frequency. This frequency band-width will be computed with the MATLAB's find peaks algorithm as the half prominence width.

6.8.1 Cartesian scheme

Experimental setup

The spatial grid size was chosen as

$$N_x = N_y = 128. \tag{6.51}$$

The initial kinetic energy was chosen as

$$K = 10^{-6}\text{J}. \tag{6.52}$$

As explained at the beginning of this section, the initial velocity height vary depending on the loading radius, to maintain this initial kinetic energy. A example of the initial position and the initial velocity is shown in figure 6.21.

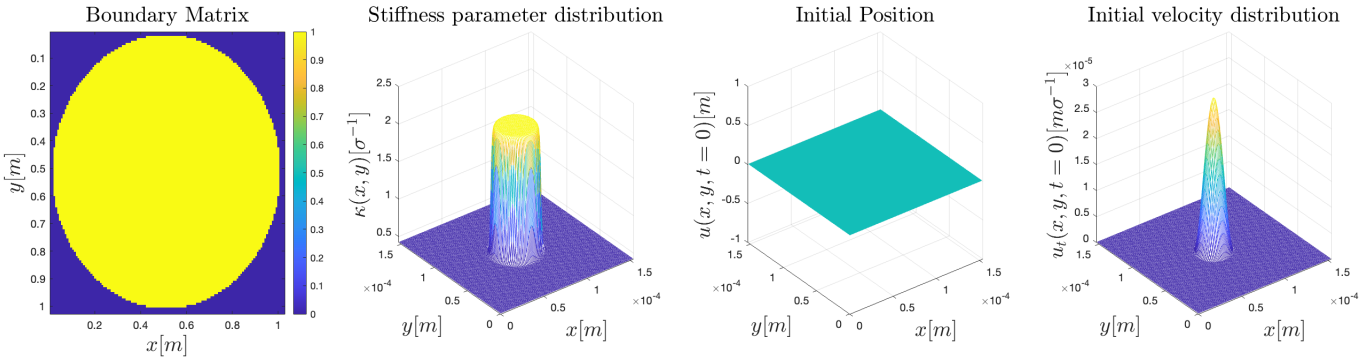

Figure 6.21: Boundary matrix, stiffness parameter distribution and a example of the initial conditions implemented for the quality factor experiments. For this example $Di_{\text{int}} = 30\%$ and $H_{\text{int}} = 400\%$.

The time scaling factor was taken as

$$\sigma = 10^{-6}s. \tag{6.53}$$

The total time of the simulation was

$$T_F = 10\mu s = 10\sigma \tag{6.54}$$

and the -60 dB decay time was taken as

$$T_{60} = T_F, \tag{6.55}$$

in order to have significant damping phenomenon in for the duration of the experiment.

Results

In figure 6.22 the signal read at the centre of the plate corresponding to different loading measures are shown. The absolute value of the FFT of the signals in figure 6.22 are shown in figure 6.23.

The complete exploration of the parameters space $Di_{\text{int}} \times H_{\text{int}}$ in terms of quality factor is shown in figure 6.24. The quality factor measured with the bandwidth method Q_w, using the value of the FFT of the signal measured at the centre of the plate as the FRF is given in two ways; one using as the resonant frequency the maximum value of the FRF, $Q_w(f_{\max})$, and the second one using the first mode of vibration as the resonant frequency $Q_w(f_{1^{\text{st}}})$. The resonant frequency actually corresponds to $f_{\max}$, and is in this mode where the improvement of the quality factor is given. The quality factor measured using the first mode of vibration is shown as a comparison.

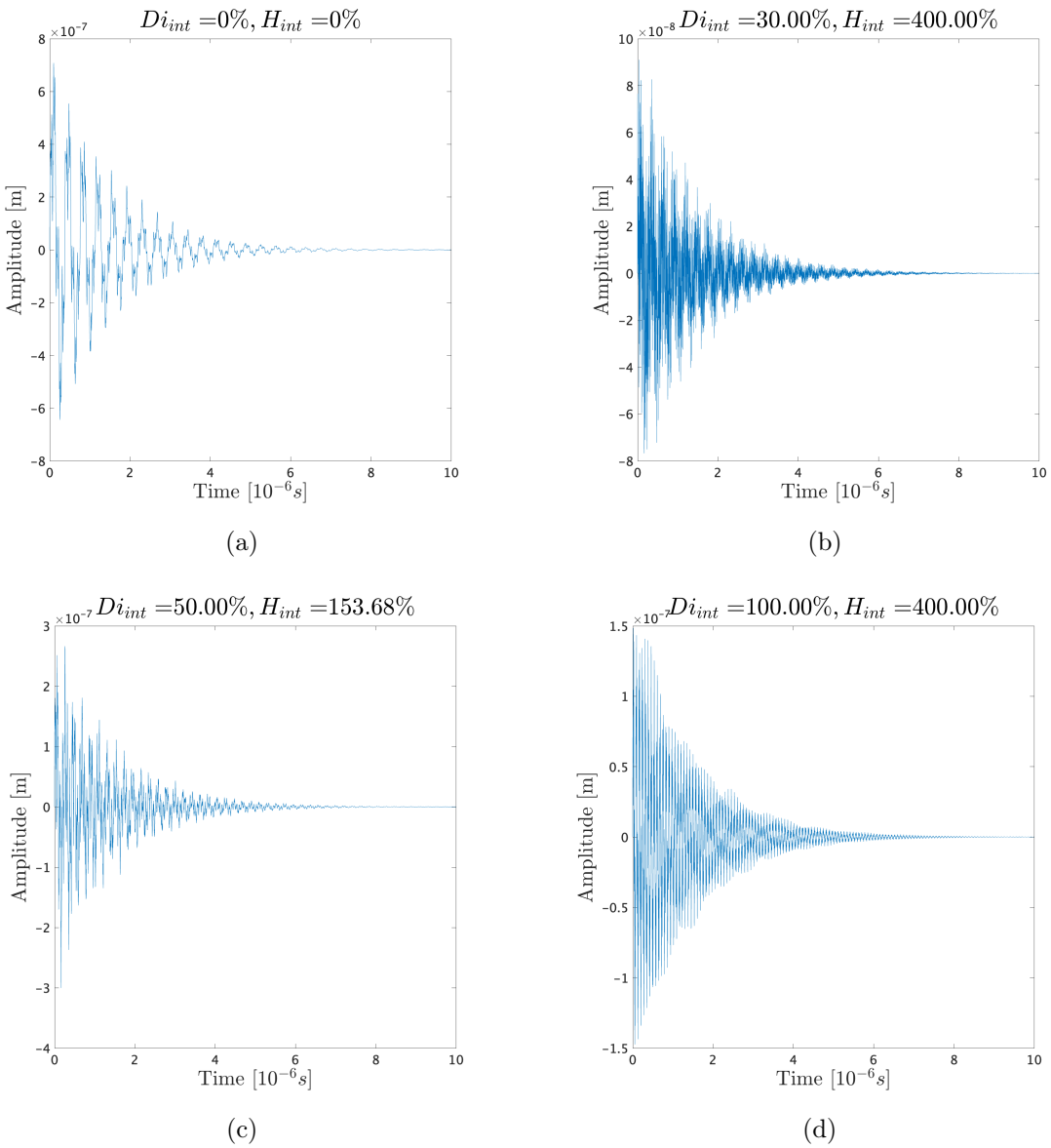

Figure 6.22: Cartesian coordinates result. Waveform of the plate's deflection measured the middle point, for different values of Di_{int} and H_{int}, as specified.

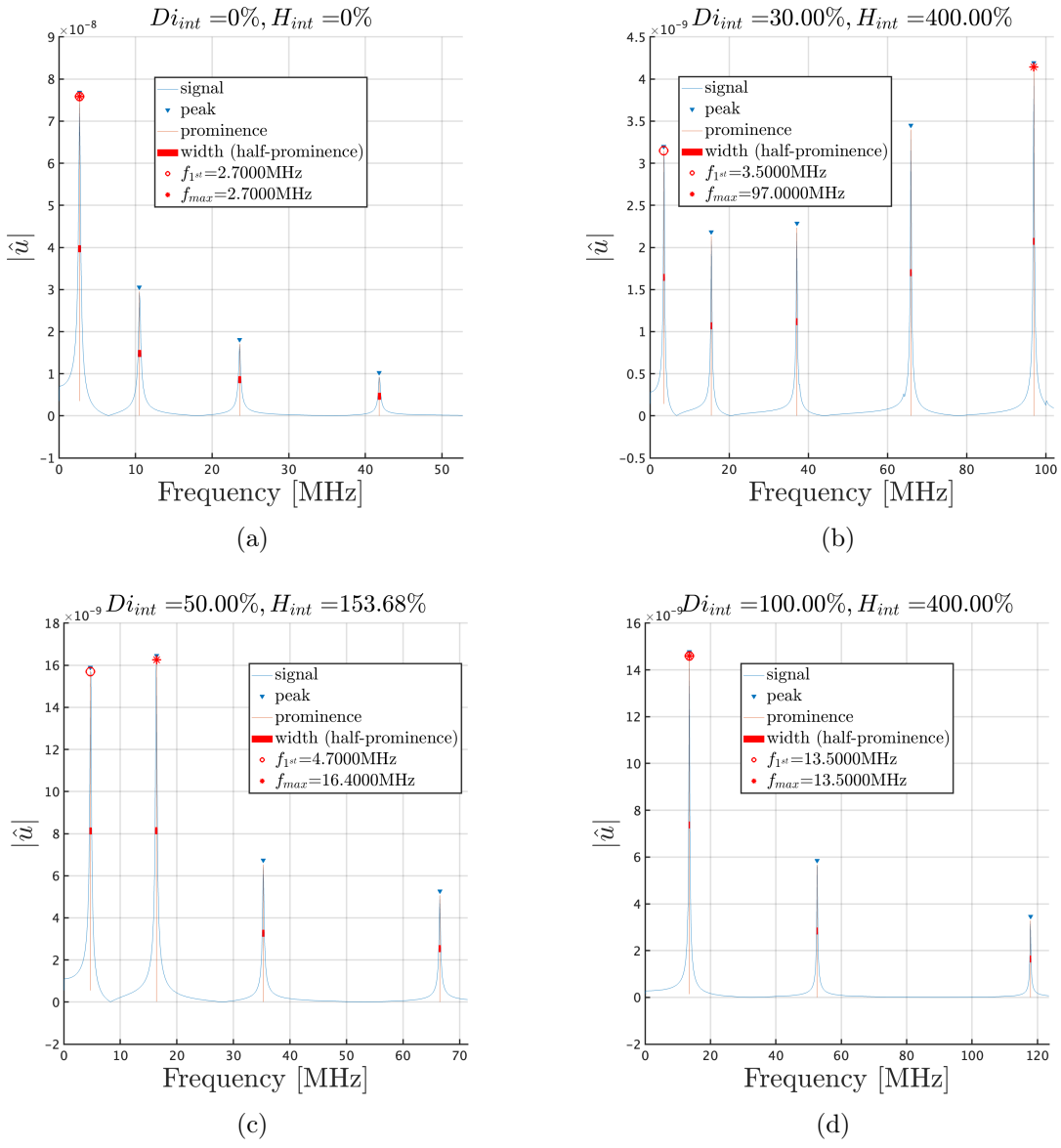

Figure 6.23: Fourier transform of the signal measured in centre of the plates. The loading diameter and thickness is specified on top of each figure. The colours where chosen to highlight the features of interest: the resonant frequency ($f_{1^{st}}$ or $f_{\max}$) and the band-width (half prominence). The line-width of the half-prominence has been enlarged to make it noticeable. It is measured at the centre of the red rectangle.

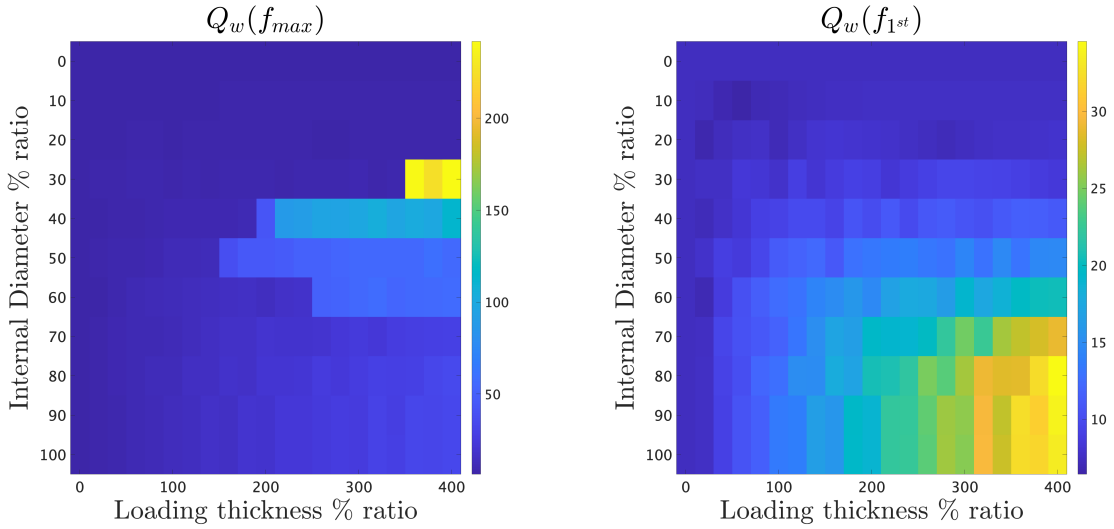

(a) (b)

Figure 6.24: Quality factor behaviour as a function of the internal diameter and thickness using: (a) the most energetic frequency and (b) the first mode of vibration.

6.8.2 Polar scheme

Experimental setup

The spatial grid size was chosen as

$$N_r = N_\theta = 30. \tag{6.56}$$

The initial kinetic energy was chosen as

$$K = 5 \times 10^{-6}\text{J}. \tag{6.57}$$

As explained at the beginning of this section, the initial velocity height vary depending on the loading radius, to maintain this initial kinetic energy. A example of the initial position and the initial velocity is shown in figure 6.25.

The time scaling factor was taken as

$$\sigma = 10^{-6}s. \tag{6.58}$$

The total time of the simulation was

$$T_F = 20\mu s = 20\sigma \tag{6.59}$$

and the -60 dB decay time was taken as

$$T_{60} = T_F. \tag{6.60}$$

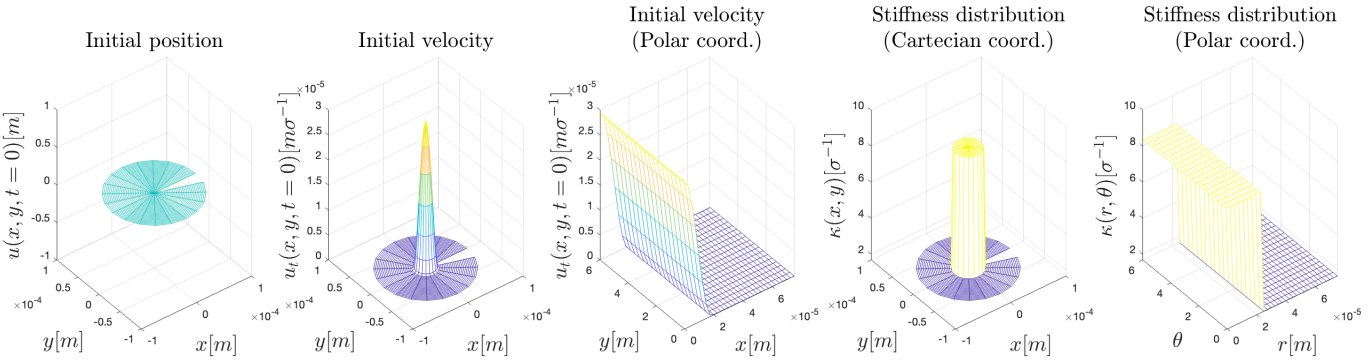

Figure 6.25: Example of the initial conditions, and stiffness parameter distribution implemented for the quality factor experiments. For this example $Di_{\text{int}} = 30\%$ and $H_{\text{int}} = 400\%$. Note: it may look like there is a missing value, but we are showing the grid function domain which runs from 0 to $2\pi - h_\theta$.

Results

In figure 6.26 the signal read at the centre of the plate corresponding to different loading measures are shown. The absolute value of the FFT of the signals in figure 6.26 are shown in figure 6.27.

The complete exploration of the parameters space $Di_{\text{int}} \times H_{\text{int}}$ in terms of quality factor is shown in figure 6.28. The quality factor measured with the bandwidth method Q_w, using the value of the FFT of the signal measured at the centre of the plate as the FRF is given in two ways; one using as the resonant frequency the maximum value of the FRF, $Q_w(f_{\max})$, and the second one using the first mode of vibration as the resonant frequency $Q_w(f_{1^{\text{st}}})$. The resonant frequency actually corresponds to $f_{\max}$, and is in this mode where the improvement of the quality factor is given. The quality factor measured using the first mode of vibration is shown as a comparison.

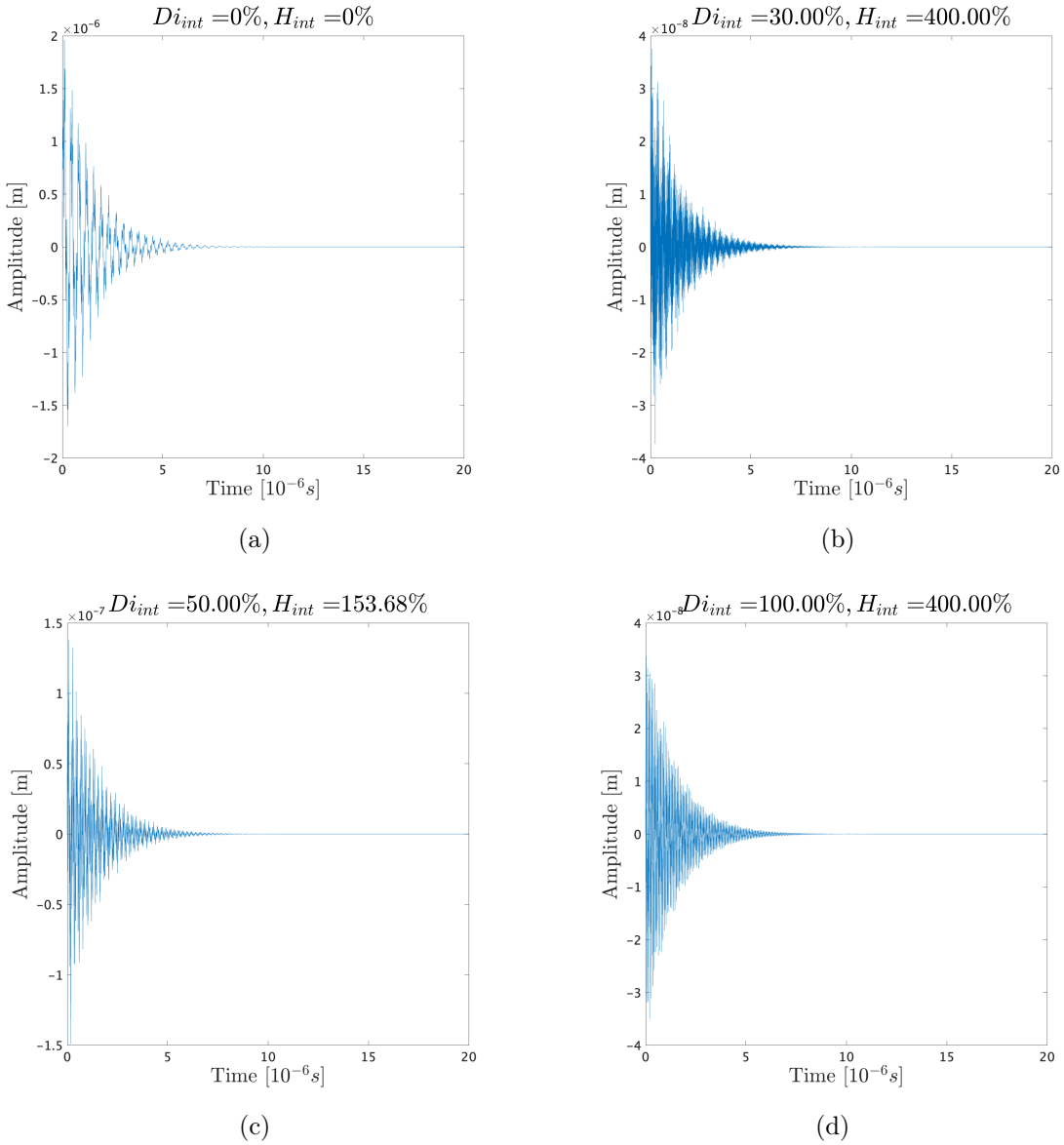

Figure 6.26: Polar Coordinates results. Waveform of the plate's deflection measured the middle point, for different values of Di_{int} and H_{int}, as specified.

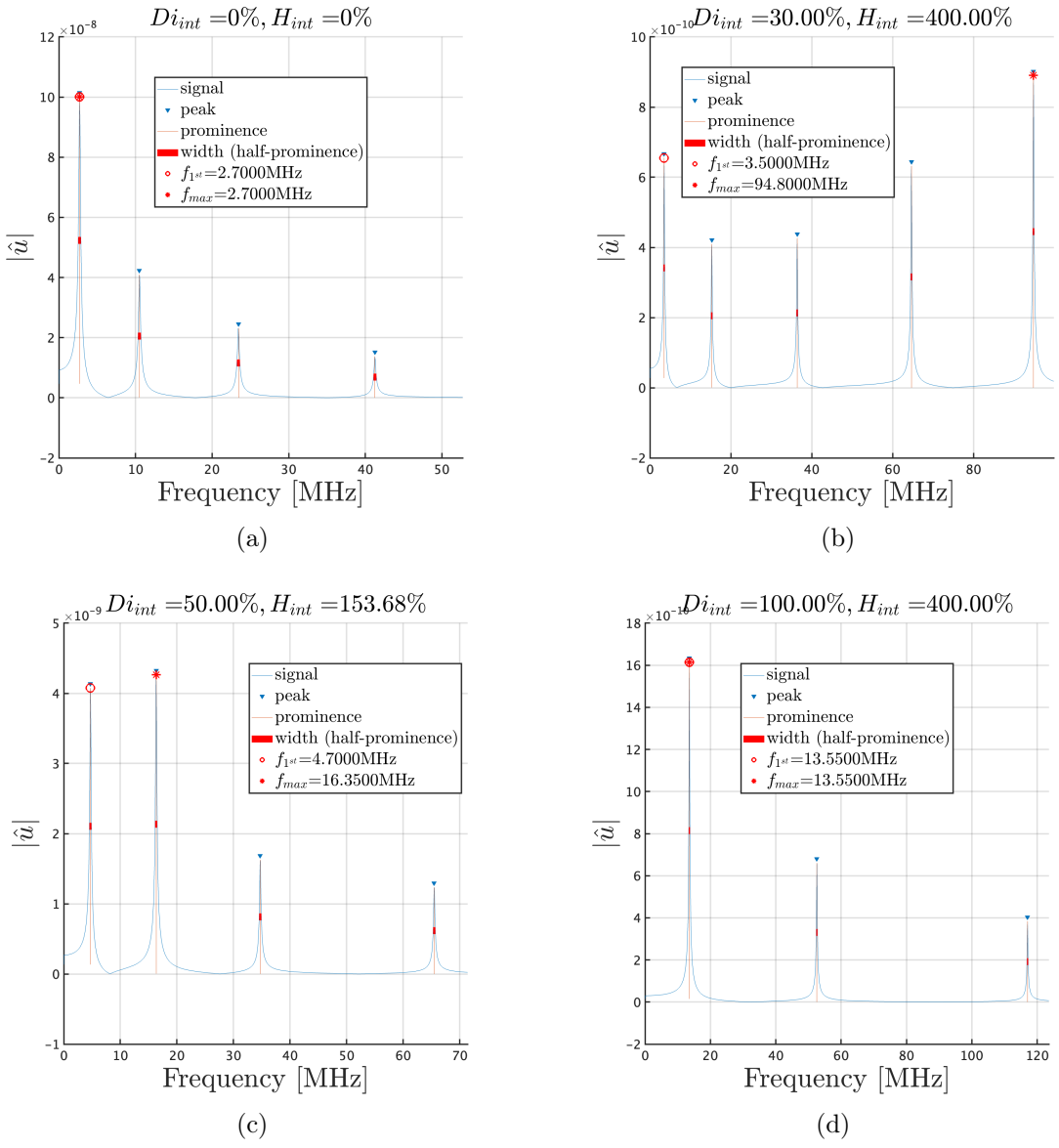

Figure 6.27: Fourier transform of the signal measured in centre of the plates. The loading diameter and thickness is specified on top of each figure. The colours where chosen to highlight the features of interest: the resonant frequency ($f_{1^{st}}$ or $f_{\max}$) and the band-width (half prominence). The line-width of the half-prominence has been enlarged to make it noticeable. It is measured at the centre of the red rectangle.

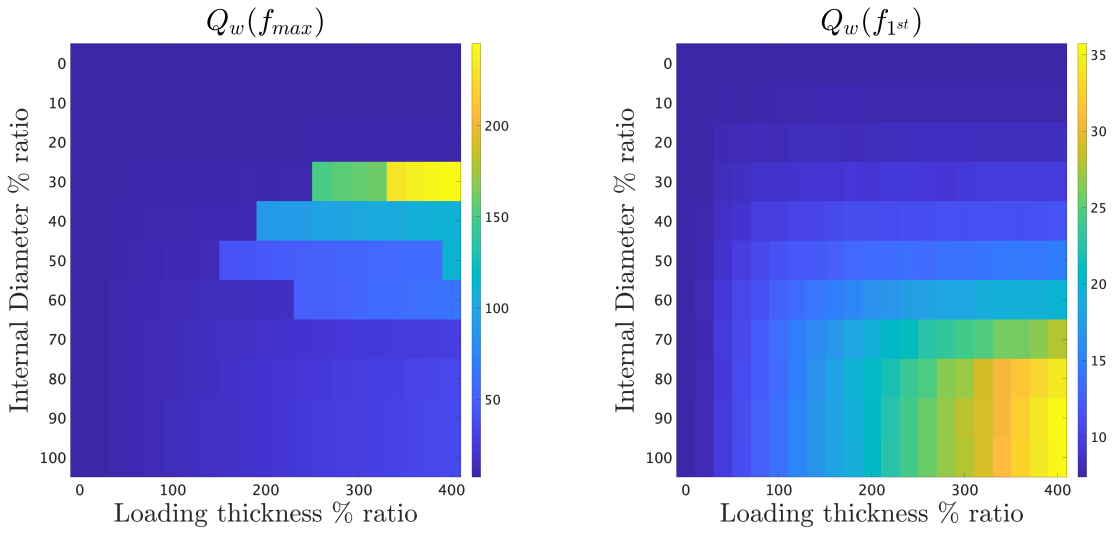

Figure 6.28: Quality factor behaviour as a function of the internal diameter and thickness using: (a) the most energetic frequency and (b) the first mode of vibration.

6.8.3 Comments on the quality factor results

- The results show a comparable behaviour of the scheme in Cartesian coordinates and the one in polar coordinates. They differ in specific values but the overall qualitative behaviour is very similar.

- The experiments show an improvement in the Q-factor in certain regimes of internal diameter and loading. The mechanism through which the quality factor is improved consists of the transfer of the resonant frequency ($f_{\max}$) from the first mode of vibration to higher order modes, as can be seen in figures 6.23 and 6.27, where the homogeneous unloaded plate in (a) and the homogeneous fully loaded plate in (d) shows a resonant frequency in the first mode, while in the partially loaded plate in (b) and (c) the resonant frequency is found in the second and fifth partial respectively.

- The quality factor results are clearer when using the polar coordinates scheme than with the Cartesian coordinates one. This can be due to the difference in the discretisation. As mentioned in section 6.6, the boundary conditions are given more directly in the polar scheme than in the Cartesian one. Another factor that may induce 'noise' in the Cartesian scheme results is the shape of the loading distribution. As mentioned in section 6.3 the logistic-growth rate k_s may induce certain dispersion when the step is not 'smooth' enough, but may be approximating another system when the stiffness distribution is too smooth. If we had to choose, the polar scheme would be chosen, as it shows no dispersive behaviour even for the step-function stiffness distribution (which is closer to the phenomenon we want to model). The boundary conditions are simpler to implement and constitute a better approximation. We show the results for both schemes as a consistency test, even when the Cartesian shows the mentioned problems.

- The higher improvement of the quality factor is observed when the internal diameter is $Di_{int} = 30\%$ and the internal thickness is $H_{int} = 400\%$ and it is of the order of 10 times, when comparing the quality factor obtained from a fully loaded plate, and about 100 times with respect to the unloaded plate. There are other regimes where we can observe an improvement of the quality factor, for example $Di_{int} = 50\%$ and $H_{int} \approx 150\%$, where there is an improvement of about 1.2 times with respect to the fully loaded plate, and about 25 times when comparing with the unloaded plate. A region of significant Q-factor improvement can be found by looking at the lighter colours in figure 6.28 (a), this is, Di_{int} in the region between $(30\% - 60\%)$ and H_{int} in the region $(150\% - 400\%)$.

Chapter 7

Conclusions and future work

7.1 Conclusions

We developed a mathematical and computational method to study the vibrations and resonant properties of loaded plates in the context of MEMS and NEMS devices.

The foundations of the Classical Plate Theory, including a revision of the Linear Elasticity in Continuum Mechanics is presented. Then, two possible modifications of this theory are given: the Variable-coefficients and the Variable-density model. The variable-density model is chosen to be the mathematical approximation of the phenomenon of interest, and it was solved by applying the Finite Difference Method in two spatial dimensions. We developed two different finite difference schemes, one in Cartesian coordinates, and a second one in polar coordinates, both showing comparable results in the frequency domain, but obtaining better and more trustful results with the polar coordinates scheme.

The Harmonicity of the normal modes of a loaded plate system was measured and showed that it could be improved up to the fourth mode of vibration. For higher order frequencies the results do not show a clear tendency.

The main result of this study, as it can have many applications in MEMS/NEMS, is the improvement of the quality factor by up to 100 times with respect to an unloaded polymer plate and up to 10 times when compared to a fully loaded plate. This result still needs to be validated experimentally, but we have comparable numerical experiments that show promising results. Among the possible applications of this research is the possibility of improving pressure or mass sensors on the micro and

nano scale.

7.2 Future work

- The numerical results will be validated experimentally. An ongoing collaboration with the University of Groningen seeks to build the loaded micro-plates and measure the corresponding results. This will require new simulations with the specific material and geometrical properties.
- Understand the relation between the polar coordinate scheme developed in this work and the one presented in [Bilbao, 2009].
- Contrast the numerical results with other types of numerical procedures such as the Finite Element Method or Spectral methods.
- Implement optimisation methods for the loading to optimise the quality factor.
- Explore the possibility of implementing the variable-coefficients model both mathematically and numerically.
- Investigate and implement a model for the loaded plate vibrations under the influence of voltage tension. Adding a external force in the equation of motion, proportional to the electromagnetic attractive force over the plate's surface, can be one implementation.

Appendices

Appendix A

Variational calculus

In this appendix, a brief and concise description of the rudiments of calculus of variations, used to obtain the plate's equation of motion will be given. The description will not be very formal, (compared with the conceptualisation in terms of Lebesgue and Sobolev spaces) as it only seeks to offer a computational approach. This description was taken from [Reddy, 2006]. A formal approach to the variational methods can be consulted in [Dacorogna, 2014].

A.1 The Variational Operator

The delta symbol, δ, used in conjunction with displacements or forces can be interpreted as an operator, and is known as the *variational operator*. It is used to denote a variation (or change) in a given quantity, this is, δu denotes a variation in u, in a similar way as dx denotes a variation in x. In fact, the variational operator δ is a differential operator with respect to the dependent variables. The laws of variation of sums, products, ratios, powers, and so forth are completely analogous to the corresponding laws of differentiation. For example, if $F_1 = F_1(u)$ and $F_2 = F_2(u)$, we have

$$\begin{aligned} &(1)\,\delta(F_1 \pm F_2) = \delta F_1 \pm \delta F_2 \\ &(2)\,\delta(F_1 F_2) = \delta F_1 F_2 + F_1 \delta F_2 \\ &(3)\delta(\frac{F_1}{F_2}) = \frac{\delta F_1 F_2 - F_1 \delta F_2}{F_2^2} \\ &(4)\delta(F_1)^n = n(F_1)^{n-1}\delta F_1 \end{aligned} \tag{A.1}$$

For a function of several dependent variables (and possibly their derivatives), $G = G(u, v, w)$, the total variation is the sum of partial variations,

$$\delta G = \delta_u G + \delta_v G + \delta_w G, \tag{A.2}$$

where, for example, $delta_u$ denotes the partial variation with respect to u. The variational operator can be interchanged with differential and integral operators, as

$$\delta\left(\frac{du}{dx}\right) = \frac{d\delta u}{dx}, \tag{A.3}$$

and

$$\delta\left(\int_\Omega u\, d\Omega\right) = \int_\Omega \delta u\, d\Omega, \tag{A.4}$$

where Ω is a bounded subset of $\mathbb{R}^n$.

A.2 Functionals

A functional is a real number $I(u)$ obtained by an operator $I(\cdot)$ that maps functions u of a vector space H into a real number $I(u)$ in the set of real numbers $\mathbb{R}$. A functional is said to be linear if

$$I(c_1u + c_2v) = c_1I(u) + c_2I(v), \tag{A.5}$$

for all $u, v \in$

Let $I(u)$ denote the integral defined in the interval (a, b),

$$\int_a^b F(x, u, u')dx, \tag{A.6}$$

where F is a function of x, u and $u' = du/dx$. Then the variation of a functional can be calculated as

$$\delta I(y) = \delta\int_a^b F(x, u, u')dx = \int_a^b \delta F dx = \int_a^b \left(\frac{\partial F}{\partial u}\delta u + \frac{\partial F}{\partial u'}\delta u'\right) dx. \tag{A.7}$$

A fundamental tool used in the calculus of variations, is the following theorem.

Theorem 2 (Fundamental lemma of calculus of variations)**.** *Let $\Omega \subset \mathbb{R}^n$. For any integrable function $G \in L^1_{loc}$, if the statement*

$$\int_\Omega G \cdot \eta dx = 0 \tag{A.8}$$

holds for all $\eta(x) \in C_0^\infty(\Omega)$, then it follows that $G = 0$ almost everywhere in Ω.

A proof of this theorem can be consulted in [Dacorogna, 2014]. A more general statement of the fundamental lemma is as follows: If η is arbitrary in $a < x < b$ and $\eta(a)$ is arbitrary, then the statement

$$\int_a^b G \cdot \eta dx + B(a) \cdot \eta(a) = 0 \tag{A.9}$$

implies that $G = 0$ almost everywhere in (a, b), and $B(a) = 0$, because $\eta(x)$ is independent of $\eta(a)$.

A.3 Euler-Lagrange equations

Consider the problem of finding the extremum (i.e., minimum or maximum) of the functional

$$I(u) = \int_a^b F(x, u, u')dx, \quad u(a) = u_a,\ u(b) = u_b. \tag{A.10}$$

The necessary condition for the functional to have a minimum or maximum is (analogous to maxima or minima of functions) that its first variation be zero, this is

$$\delta I(u) = 0, \tag{A.11}$$

thus,

$$0 = \int_a^b \delta F dx = \int_a^b \left(\frac{\partial F}{\partial u}\delta u + \frac{\partial F}{\partial u'}\delta u' \right) dx. \tag{A.12}$$

Note that $\delta u' = \delta(du/dx) = d(\delta u/dx)$. We cannot use the fundamental lemma in the above equation because it is not in the form of (A.8) or (A.9). To recast the above equation in the form of (A.8), we integrate the second term by parts and obtain

$$\begin{aligned} 0 &= \int_a^b \left(\frac{\partial F}{\partial u}\delta u + \frac{\partial F}{\partial u'}\delta u' \right) dx \\ &= \int_a^b \left(\frac{\partial F}{\partial u}\delta u + \frac{\partial F}{\partial u'}\frac{d\delta u}{dx} \right) dx \\ &= \int_a^b \left(\frac{\partial F}{\partial u} + \frac{d}{dx}\frac{\partial F}{\partial u'} \right) \delta u\, dx + \left[\frac{\partial F}{\partial u'}\delta u \right]_a^b. \end{aligned} \tag{A.13}$$

There are two parts in the boundary term,

$$\left[\frac{\partial F}{\partial u'}\delta u \right]_a^b, \tag{A.14}$$

a varied quantity and its coefficient. The variable u that is subjected to variation is called the *primary variable*. The coefficient of the varied quantity, i.e., the expression next to δu in the boundary term, is called a *secondary variable*. The product of the primary variable (or its variation) with the secondary variable often represents the work done (or virtual work done). The specification of the primary variable at a boundary point is termed the *essential boundary condition*, and the specification of the secondary variable is called the *natural boundary condition*. In solid mechanics, these are known as the *geometric* and *force* boundary conditions, respectively. All admissible variations must satisfy the homogeneous form of the essential (or geometric) boundary conditions: $\delta u(a) = 0$and $\delta u(b) = 0$. Elsewhere, $a < x < b$, δu is arbitrary.

Returning to equation (A.13), we note that the boundary terms drop out because of the conditions $\delta u(a) = 0$ and $\delta u(b) = 0$. We have

$$0 = \int_a^b \left(\frac{\partial F}{\partial u} + \frac{d}{dx}\frac{\partial F}{\partial u'} \right) \delta u \, dx \tag{A.15}$$

which must hold for any δu in (a, b). In view of the fundamental lemma of calculus of variations ($\eta = \delta u$), it follows that

$$G = \frac{\partial F}{\partial u} + \frac{d}{dx}\frac{\partial F}{\partial u'} = 0, \tag{A.16}$$

in (a, b). Therefore, the necessary condition for $I(u)$ to be an extremum at $u = u(x)$ is that $u(x)$ be the solution of (A.16), which is known as the *Euler—Lagrange equation* associated with the functional $I(u)$, i.e., $\delta I = 0$ is equivalent to eqauation (A.16).

If $u(a) = u_a$ and $\delta u(b)$ is arbitrary (i.e., $u(a)$ is specified but u is not specified at $x = b$), then $\delta u(a) = 0$ and we have from Eq. (2.1.29) the result

$$0 = \int_a^b \left(\frac{\partial F}{\partial u} + \frac{d}{dx}\frac{\partial F}{\partial u'} \right) \delta u \, dx + \left[\frac{\partial F}{\partial u'} \right]_{x=b} \delta u(b). \tag{A.17}$$

Since δu is arbitrary in (a, b) and $\delta u(b)$ is arbitrary, the above equation implies, in view of (A.9), that both the integral expression and the boundary term be zero separately, thus

$$\begin{aligned} \frac{\partial F}{\partial u} + \frac{d}{dx}\frac{\partial F}{\partial u'} &= 0, \quad a < x < b \\ \left[\frac{\partial F}{\partial u'} \delta u \right] &= 0, \quad x = b. \end{aligned} \tag{A.18}$$

Equations in (A.18) are called the *Euler-Lagrange equations*. Note that the boundary conditions that are a part of the Euler-Lagrange equations always belong to the class of natural boundary conditions.

Appendix B

Codes

In this appendix, we show the MATLAB codes to simulate the loaded-damped plate using finite difference method in both Cartesian and polar coordinates.

B.1 Cartesian coordinates scheme

```
function [out, SR, h, ss, k] = Plate_cartesian(Di_ext, H_ext, E_ext, rho_ext, nu_ext, ...
 Di_int, H_int, E_int, rho_int, nu_int, ch_len, ch_wid, ctr, wid, u0, v0, ...
 sig0, k_sigmoid, Nx, TF, sigma_time, rp_mat)
%
% Simulate a plate using finite difference method in Cartesian coordinates.
% This code also provides the possibility of simulating a circular plate with channels
%
% Inputs:
% Di_ext, Di_int: External and internal diameters of the plate [m].
% H_ext, H_int: External and internal heights of the plate [m].
% E_ext, E_int: Young's moduli of the external and internal materials [Pa=kg/(ms^2)].
% rho_ext, rho_int: Densities of the external and internal materials [kg/m^3].
% nu_ext, nu_int: Poisson's ratios of the external and internal materials.
% ch_len, ch_wid: Length and width of the chanels in the y direction
% ctr: Centre coordinates for boundary conditions [0-1,0-1] as a fraction
% of the plate's diameter.
% wid: Width parameter for the boundary conditions [0-1,0-1] as a fraction
% of the plate's diameter.
% u0: Initial displacement height in [m].
% v0: Initial velocity distribution height in [m/s].
% sig0: Parameter for the finite difference scheme.
% k_sigmoid: Parameter for a sigmoid function.
```

```
% Nx: Number of spatial subdivisions in the x-direction.
% TF: Final simulation time.
% sigma_time: Scale parameter for Young's modulus.
% rp_mat: Matrix specifying readout positions ([0-1,0-1]) as a
    fraction
% of the plate's diameter.
%
% Outputs:
% out: Simulation output for readout positions over time.
% SR: Sample Rate calculated based on stability condition.
% h: Grid spacing.
% ss: Total grid size.
% k: Time step for the simulation.
%

% Start measuring execution time
tic;
% Calculate time-scaled scaled velocity
v0 = v0 * sigma_time;

% Calculate scale parameter for Young's modulus
E_scale_param = sigma_time^2;

% Calculate time scale for display
time_scale = strcat('10^{', num2str(log10(sqrt(E_scale_param))), '}s
    ');

% Calculate scaled Young's moduli
E_ext_scale = E_ext * E_scale_param;
E_int_scale = E_int * E_scale_param;

% Calculate stiffness parameters for external and internal materials
D_ext = (E_ext_scale) * H_ext^3 / (12 * (1 - nu_ext^2));
K_ext = sqrt(D_ext / (rho_ext * H_ext * (Di_ext)^4));

HT = H_int + H_ext;

rho_l = HT / (H_ext / rho_ext + H_int / rho_int);
E_l = HT / (H_ext / E_ext_scale + H_int / E_int_scale);
nu_l = HT / (H_ext / nu_ext + H_int / nu_int);

D_int = E_l * HT^3 / (12 * (1 - nu_l^2));
K_int = sqrt(D_int / (rho_l * HT * (Di_ext)^4));

% Set global parameters
K1 = K_ext;  % unloaded plate stiffness parameter (1/sig)
K2 = K_int;  % loaded plate stiffness parameter (1/sig)

% Stability condition/scheme parameters
K = max([K1, K2]);
K_min = min([K1, K2]);
mu = 0.25;  % scheme free parameter

% Calculate derived parameters
```

```
h = 1 / (Nx - 4);
k = mu * h^2 / K;
SR = floor(1 / k); % sample rate

% Calculate number of subdivisions in the y-direction
y_extra = floor(ch_len / (h * Di_ext));
Ny = Nx + y_extra;

% Calculate simulation duration
NF = floor(SR * TF);

% Create meshgrid for spatial coordinates
[X, Y] = meshgrid([1:Nx-1] * h, [1:Ny-1] * h);
Xaxis = [1:Nx-1] * h;
Yaxis = [1:Ny-1] * h;
ss = (Nx - 1) * (Ny - 1); % total grid size

% Boundary condition matrix
Bo = zeros((Ny - 1), (Nx - 1));
for i = 1:Nx-1
    for j = 1:Ny-1
        if sqrt((i - (Nx - 1) / 2)^2 + (j - (Ny - 1) / 2)^2) <= (Nx - 5) / 2
            Bo(j, i) = 1;
        end
    end
end

% Additional rectangular boundary condition
Bo_rect = zeros((Ny - 1), (Nx - 1));
for i = 1:Nx-1
    for j = 2:Ny-2
        if abs(h * Di_ext * (i - (Nx - 1) / 2)) < ch_wid / 2
            Bo_rect(j, i) = 1;
        end
    end
end
Bo = Bo + Bo_rect;
Bo(Bo > 0) = 1;

% Stiffness parameter distribution
K_Mat = zeros((Ny - 1), (Nx - 1));
R2_mat = (Di_int / Di_ext) * (Nx - 1) / 2;

for i = 1:Nx-1
    for j = 1:Ny-1
        r = sqrt((i - (Nx - 1) / 2)^2 + (j - (Ny - 1) / 2)^2);
        logis = K - (K - K_min) * (1 / (1 + exp(-k_sigmoid * (r - R2_mat))));
        K_Mat(j, i) = logis;
    end
end

Xax = Di_ext * X;
```

```
Yax = Di_ext * Y;
K_vect = reshape(K_Mat, ss, 1);
K_vect2 = K_vect.^2;

% Finite difference scheme matrices
Dxx = sparse(toeplitz([-2 / h^2; 1 / h^2; zeros(Nx - 3, 1)]));
Dyy = sparse(toeplitz([-2 / h^2; 1 / h^2; zeros(Ny - 3, 1)]));
D = kron(eye(Nx - 1), Dyy) + kron(Dxx, eye(Ny - 1)); % Laplacian
    matrix operator
DD = D * D; %Biharmonic matrix operator
I2 = sparse((1 / (1 + sig0 * k)) * 2 * eye(ss));
DD2 = sparse((1 / (1 + sig0 * k)) * k^2 * DD);
C = ((1 - sig0 * k) / (1 + sig0 * k)) * sparse(eye(ss));

% Readout interpolation parameters
rp_index_vect = zeros(size(rp_mat, 1));
for i = 1:size(rp_mat, 1)
    rp = rp_mat(i, 1:end);
    rp_index = (Ny - 1) * floor(rp(1) * Nx) + floor(rp(2) * Ny);
    rp_index_vect(i) = rp_index;
end

% Create 2D raised cosine distribution
dist = sqrt((X - ctr(1) * max(max(X))).^2 + (Y - ctr(2) * max(max(Y)
    )).^2);
ind = sign(max(-dist + wid / 2, 0));
rc = 0.5 * ind .* (1 + cos(2 * pi * dist / wid));
rc = reshape(rc, ss, 1);
RC = reshape(rc, [Ny - 1, Nx - 1]);

% Initial conditions
qu = zeros((Ny - 1), (Nx - 1));

for i = 1:Nx - 1
    for j = 1:Ny - 1
        r = sqrt((i - (Nx - 1) / 2)^2 + (j - (Ny - 1) / 2)^2);

        % Fourth Power Initial Position
        if r * h * Di_ext <= Di_ext / 2
            qu(j, i) = ((1 / 2)^2 - (r * h * 1)^2)^2;
        end

    end
end

% Reshape initial conditions
qu = reshape(qu, ss, 1);

% Initialize grid functions

u_nm1 = u0 * qu;
u_n = u_nm1 + k * v0 * rc;

% Initialise output signals
```

```
179
180 out = zeros(NF, length(rp_mat));
181
182 for i=1:size(rp_mat,1)
183    out(1,i) = u_nm1(rp_index_vect(i));
184    out(2,i) = u_n(rp_index_vect(i));
185 end
186
187 U1 = reshape(u_n, [Ny - 1, Nx - 1]);
188 BU1 = Bo .* U1;
189 u_n = reshape(BU1, ss, 1);
190
191 % Main loop
192 for n = 3:NF
193     if mod(n, 50000) == 0
194         NF - n
195     end
196
197     % Finite difference scheme
198     u_np1 = I2 * u_n - DD2 * (u_n .* K_vect2) - C * u_nm1;
199
200     % Clamped Boundary
201     U = reshape(u_np1, [Ny - 1, Nx - 1]);
202     BU = Bo .* U;
203     u_np1 = reshape(BU, ss, 1);
204
205     % Update grid function values
206
207     u_nm1 = u_n;
208     u_n = u_np1;
209
210     % Record output for readout positions
211     for i = 1:size(rp_mat, 1)
212         out(n, i) = u_np1(rp_index_vect(i));
213     end
214 end
215
216 % End of the main loop
217
218 % End measuring execution time
219 toc;
```

Listing B.1: Cartesian coordinates Scheme

B.2 Polar coordinates scheme

```
1
2 function [out,SR,hr,ht,k]=...
3 Polar_plate_2lapl(Di_ext,H_ext,E_ext,rho_ext,nu_ext,Di_int,H_int,
    E_int,...
4 rho_int,nu_int,sigma_time,k_stability_constant,ctr,wid,u0,v0,sig0
    ,...
```

```
k_sigmoid,logistic_fun,Nr,Nt,TF,rp_mat)
%%%%%%%%%%%%%%%
% Simulate a non-homogeneous plate using finite difference method
%
% Inputs:
% Di_ext, Di_int: External and internal diameters of the plate [m].
% H_ext, H_int: External and internal heights of the plate [m].
% E_ext, E_int: Young's moduli of the external and internal
    materials [Pa=kg/(ms^2)].
% rho_ext, rho_int: Densities of the external and internal materials
     [kg/m^3].
% nu_ext, nu_int: Poisson's ratios of the external and internal
    materials.
% sigma_time: Time scaling factor.
% kstability_constant: Constant used for stability calculation.
% ctr: Centre coordinates for a velocity distribution calculation in
     cartecian coordinates [x,y] in [m].
% wid: Width parameter for the velocity distribution in [m].
% u0: Initial displacement height in [m].
% v0: Initial velocity height in [m/s].
% sig0: Damping parameter in [sigma^(-1)].
% k_sigmoid: Parameter for a sigmoid function.
% logistic_fun: Flag for selecting a logistic function.(1=true, 0=
    false)
% Nr: Number of radial steps for discretisation.
% Nt: Number of angular steps for discretisation.
% TF: Final simulation time in [sigma_time*s].
% rp_mat: Matrix specifying readout positions.([0-1,0-2*pi])
%
% Outputs:
% out: Simulation output for readout positions over time.
% SR: Sample Rate calculated based on stability condition.
% hr: Radial step size.
% ht: Angular step size.
% k: Time step for the simulation.
%%%%%%%%%%%%%%%%%%%%%%%%%%%%%%%%%%%%%%%%%%%%%%%%%%%%%%%%

tic % Start measuring execution time

% Calculate time-scaled velocity
v0 = v0 * sigma_time;

% Calculate scale parameter for Young's modulus

E_scale_param=sigma_time^2; % Scale parameter for the Young's
    modulus

% Scale Young's modulus
E_ext_scale = E_ext * E_scale_param;
E_int_scale = E_int * E_scale_param;

% Compute Stiffness parameters for exterior and interior
D_ext = (E_ext_scale) * H_ext^3 / (12 * (1 - nu_ext^2));
K_ext = sqrt(D_ext / (rho_ext * H_ext * (Di_ext / 2)^4));
```

```
HT = H_int + H_ext;
rho_l = HT / (H_ext / rho_ext + H_int / rho_int);
E_l = HT / (H_ext / E_ext_scale + H_int / E_int_scale);
nu_l = HT / (H_ext / nu_ext + H_int / nu_int);
D_int = E_l * HT^3 / (12 * (1 - nu_l^2));
K_int = sqrt(D_int / (rho_l * HT * (Di_ext / 2)^4));

K_max = max([K_int, K_ext]);
K_min = min([K_int, K_ext]);
R_int = Di_int / Di_ext;

% Radial coordinates step size and count
hr = 1 / Nr;
Nr = floor(1 / hr);

% Angular coordinates step size and count
ht = 2 * pi / Nt;
Nt = round(2 * pi / ht);

% Stability condition - calculate time step 'k'
k = k_stability_constant * (hr^2 / (2 * K_max)) * (1 / (1 + 1 / (ht
    ^2)));

% Calculate Sample Rate
SR =floor(1 / k);

% Number of Time Steps
NF = floor(SR * TF);

% Polar and Cartesian coordinates axes
[R, T] = meshgrid([0:Nr] * hr * Di_ext / 2, [0:Nt - 1] * ht);
[X, Y] = pol2cart(T, R);

% Compute readout parameters index for convenience
rp_mat_index = zeros(size(rp_mat));
for i = 1:size(rp_mat, 1)
    rp = rp_mat(i, :);
    rp_r = rp(1);
    rp_t = rp(2);
    rpr_index = floor(rp_r / hr) + 1;
    rpt_index = floor(rp_t / ht) + 1;
    rp_mat_index(i, :) = [rpr_index rpt_index];
end

% Compute rising cosine velocity distribution
%%%% Cartesian coordinates

dist = sqrt((X-ctr(1)).^2 +(Y-ctr(2)).^2);
ind = sign(max(-dist+wid/2,0));
rc = 0.5*ind'.*(1+cos(2*pi*dist'/wid));

%%%% Polar coordinates
[t,r,rc_pol]=cart2pol(X,Y,rc);

```

```
% Stifness parameters matrix

K_mat=zeros(Nr+1,Nt);
for i=1:Nr+1
    l=i-1;
    r=hr*l;
    step_func=K_int;
    if r>R_int
        step_func=K_ext;
    end
    for j=1:Nt
        if logistic_fun==1
        logis=K_int-(K_int-K_ext)*(1/(1+exp(-k_sigmoid*(r-R_int))));
        K_mat(i,j)=logis;
        else
        K_mat(i,j)=step_func;
        end

    end
end
[x,y,K_mat_cart]=pol2cart(T,R,K_mat);
% Fourth order polinomial Initial position
qu=zeros(Nr+1,Nt);
for i=1:Nr+1
    l=i-1;
    r=hr*l;
    for j=1:Nt
       qu(i,j)=(1-(r)^2)^2;

    end
end
[x,y,qu_cart]=pol2cart(T,R,qu);
% Initialise grid functions
u_nm1 = u0*qu;
u_n = u0*qu+k*v0*rc_pol;
for m=0:Nt-1
    M=mod(m,Nt)+1;
    u_nm1(1,M)=u_nm1(1,1);
    u_n(1,M)=u_n(1,1);
end
u_np1 = zeros(Nr+1,Nt);
% Initialise output
out = zeros(NF,length(rp_mat));
for i=1:size(rp_mat,1)
   out(1,i) = u_nm1(rp_mat_index(i,1),rp_mat_index(i,2));
   out(2,i) = u_n(rp_mat_index(i,1),rp_mat_index(i,2));
end
% Initialise test function v
v=zeros(Nr+1,Nt);
%% Main loop
for n=3:NF
if mod(n,50000)==0
NF-n
end
```

```
    %%%% v=lalp(u), compute Laplacian of u
   for l=1:Nr-1
       L=l+1;
     for m=0:Nt-1
         M=mod(m,Nt)+1;

         v(L,M)=((- 2* l* u_n(L,mod(m,Nt)+1) + ...
    (l - 0.5)* u_n(L-1,mod(m,Nt)+1) + (l + 0.5)* u_n(L+1,mod(m,Nt)
   +1))/(hr^2* l) + ...
    (- 2* u_n(L,mod(m,Nt)+1) + u_n(L,mod(m-1,Nt)+1) + u_n(L,mod(m+1,
   Nt)+1))/(hr^2* ht^2* l^2));

    end

   end

    %%% Boundary condition at l=Nr
    %v=u_rr

   for l=Nr
       L=l+1;
     for m=0:Nt-1
         M=mod(m,Nt)+1;

 v(L,M)=(2*u_n(L-1,mod(m,Nt)+1))/(hr^2);
 %u_n(L+1,mod(m,Nt)+1)->u_n(L-1,mod(m,Nt)+1) as u_r=0


    end

   end

%.........Centre point v..............

lapl_00=0;
  for m=0:Nt-1
      M=mod(m,Nt)+1;
 lapl_00=lapl_00+(4/((Nt)*hr^2))*(u_n(2,M)-u_n(1,M)); %forward first
    order aproximation

  end

for m=1:Nt
  v(1,m)=lapl_00;
end

%%% lapl(lapl(u))=lapl(v), compute biharmonic of u as the Laplacian
   of v, and compute the rest of the scheme
    for l=1:Nr-1
       L=l+1;
     for m=0:Nt-1
         M=mod(m,Nt)+1;

u_np1(L,M)=(-k^2*K_mat(L,M)^2)/(1+k*sig0)*((- 2* l* v(L,mod(m,Nt)+1)
```

```
    + ...
210     (l - 0.5)* v(L-1,mod(m,Nt)+1) + (l + 0.5)* v(L+1,mod(m,Nt)+1))/(
    hr^2* l) + ...
211     (- 2* v(L,mod(m,Nt)+1) + v(L,mod(m-1,Nt)+1) + v(L,mod(m+1,Nt)+1)
    )/(hr^2* ht^2* l^2))...
212     +2/(k*sig0+1)*u_n(L,M)+(k*sig0-1)/(k*sig0+1)*u_nm1(L,M);
213
214     end
215
216     end
217
218 %.........Centre point u..............
219
220 %%%%%%% l=0, L=1
221   %u00
222 %l=1,L=2
223 lapl_00=0;
224   for m=0:Nt-1
225       M=mod(m,Nt)+1;
226  lapl_00=lapl_00+(4/((Nt)*hr^2))*(v(2,M)-v(1,M));
227
228   end
229
230  for m=1:Nt
231   u_np1(1,m)=(-(k^2*K_mat(1,m)^2)/(1+k*sig0))*lapl_00+...
232       2/(k*sig0+1)*u_n(1,m)+(k*sig0-1)/(k*sig0+1)*u_nm1(1,m);
233  end
234
235
236     if size(unique(u_n(1,:)))~=size(1)
237
238         stop
239     end
240
241     if any(abs(u_n)>1e3)
242         u_n(1,1)
243         'The scheme diverges'
244         stop
245     end
246
247 % Store information in the output
248
249 for i=1:size(rp_mat,1)
250    out(n,i) = u_np1(rp_mat_index(i,1),rp_mat_index(i,2));
251 end
252
253 % Update grid function values
254
255 u_nm1 = u_n; u_n = u_np1;
256
257 end
258 %%%%%% end main loop
259
```

```
260 toc % Stop measuring execution time
```

Listing B.2: Polar coordinates Scheme

Bibliography

[AGC-chemicals, 2018] AGC-chemicals (2018). Cytop_en_brochure.pdf. https://www.agc-chemicals.com/file.jsp?id=jp/en/fluorine/products/cytop/download/pdf/CYTOP_EN_Brochure.pdf. Accessed: June, 2023.

[Banerjee, 2014] Banerjee, S. (2014). Cv raman and colonial physics: Acoustics and the quantum. *Physics in Perspective*, 16:146–178.

[Bilbao, 2009] Bilbao, S. (2009). *Numerical sound synthesis: finite difference schemes and simulation in musical acoustics*. John Wiley & Sons.

[Bilbao, 2012] Bilbao, S. (2012). Time domain simulation and sound synthesis for the snare drum. *The Journal of the Acoustical Society of America*, 131(1):914–925.

[Chaigne and Kergomard, 2016] Chaigne, A. and Kergomard, J. (2016). *Acoustics of musical instruments*. Springer.

[Dacorogna, 2014] Dacorogna, B. (2014). *Introduction to the Calculus of Variations*. World Scientific Publishing Company.

[Dubey and Krishna, 2021] Dubey, V. and Krishna, I. P. (2021). Theoretical and experimental studies on the vibration of membranes of mridangam. *Applied Acoustics*, 181:108121.

[Gaudet et al., 2006] Gaudet, S., Gauthier, C., and Léger, S. (2006). The evolution of harmonic indian musical drums: A mathematical perspective. *Journal of sound and vibration*, 291(1-2):388–394.

[Graff, 1975] Graff, K. (1975). Wave motion in elastic solids ohio state u. *Press, Columbus, Ohio*.

[Heinrich and Dufour, 2015] Heinrich, S. M. and Dufour, I. (2015). Fundamental theory of resonant mems devices. *Resonant MEMS: Fundamentals, Implementation and Application*, pages 1–28.

[Hickman, 2013] Hickman, I. (2013). *Analog Electronics: Analog Circuitry Explained*. Newnes.

[Leissa and Qatu, 2011] Leissa, A. W. and Qatu, M. S. (2011). *Vibrations of continuous systems*. McGraw-Hill Education.

[Meyers and Chawla, 2008] Meyers, M. A. and Chawla, K. K. (2008). *Mechanical behavior of materials*. Cambridge university press.

[Pujol, 2003] Pujol, J. (2003). *Elastic wave propagation and generation in seismology*, volume 227. Cambridge University Press Cambridge.

[Ramakrishnan, 1988] Ramakrishnan, T. (1988). Selected papers of raman: An introduction. *Journal of the Indian Institute of Science*, 68(11&12):509.

[Raman and Kumar, 1920] Raman, C. and Kumar, S. (1920). Musical drums with harmonic overtones. *Nature*, 104(2620):500–500.

[Raman, 1934] Raman, C. V. (1934). The indian musical drums. In *Proceedings of the Indian academy of sciences-section A*, volume 1, pages 179–188. Springer.

[Reddy, 2006] Reddy, J. N. (2006). *Theory and analysis of elastic plates and shells*. CRC press.

[Rodríguez-Cervantes, 2019] Rodríguez-Cervantes, M. T. (2019). Análisis de vibración de barras aplicado a las esculturas sonoras baschet.

[Rossing, 1992] Rossing, T. D. (1992). Acoustics of drums. *Physics Today*, 45(3):40–47.

[Salençon, 2012] Salençon, J. (2012). *Handbook of continuum mechanics: General concepts thermoelasticity*. Springer Science & Business Media.

[Sathej and Adhikari, 2009] Sathej, G. and Adhikari, R. (2009). The eigenspectra of indian musical drums. *The Journal of the Acoustical Society of America*, 125(2):831–838.

[Schlicke et al., 2016] Schlicke, H., Schröter, C. J., and Vossmeyer, T. (2016). Electrostatically driven drumhead resonators based on freestanding membranes of crosslinked gold nanoparticles. *Nanoscale*, 8(35):15880–15887.

[Šiškins et al., 2022] Šiškins, M., Kurdi, S., Lee, M., Slotboom, B. J., Xing, W., Mañas-Valero, S., Coronado, E., Jia, S., Han, W., van der Sar, T., et al. (2022). Nanomechanical probing and strain tuning of the curie temperature in suspended cr2ge2te6-based heterostructures. *npj 2D Materials and Applications*, 6(1):41.

[Slawinski, 2010] Slawinski, M. A. (2010). *Waves and rays in elastic continua*. World Scientific.

[Strikwerda, 2004] Strikwerda, J. C. (2004). *Finite difference schemes and partial differential equations*. SIAM.

[Tiwari and Gupta, 2017] Tiwari, S. and Gupta, A. (2017). Effects of air loading on the acoustics of an indian musical drum. *The Journal of the Acoustical Society of America*, 141(4):2611–2621.

[Venkateshvaran and Smith, 2023] Venkateshvaran, D. and Smith, M. (2023). Indian drums inspire microscopic membranes. *Selwyn College Calendar*. Forthcoming article.

[Zheng et al., 2017] Zheng, X.-Q., Lee, J., and Feng, P. X.-L. (2017). Hexagonal boron nitride nanomechanical resonators with spatially visualized motion. *Microsystems & Nanoengineering*, 3(1):1–8.